EXPERIMENTAL CHARACTERIZATION OF VISCOELASTIC MATERIALS FOR MARINE APPLICATIONS

By

Md. Mahmudul Hasan

A thesis submitted to the

School of Graduate Studies

in partial fulfillment of the requirement for the degree of

Master of Engineering

Faculty of Engineering and Applied Science

Memorial University of Newfoundland

May 2019

St. John's Newfoundland and Labrador Canada

Abstract

On-board noise and vibration has become an important concern across the maritime industry. Prolonged exposure to noise and vibration causes an unsafe working conditions and reduces the performance of marine professionals. In order to mitigate noise and vibration generated by on-board sources, a proper design of the insulation system and ship structural dynamics should be carried out. Viscoelastic materials (VEM) are widely applied as damping materials for structure-borne noise and vibration control in various industries. The most notable examples are aerospace, automotive and marine industries. But still now there is no standard design formulation to apply VEM effectively to the ship's hull structure. This study provides a better understanding on the effects of VEM on ship structures in order to provide ship designers with effective ways to simulate the dynamics of VEM when applied to ship structures.

Acknowledgement

Firstly, I would like to express my deepest appreciation to my supervisor Dr. Lorenzo Moro for providing me with the opportunity to work on this project. I got the foremost help from him in any situation. His motivational feedback, research idea and patience were the keys to reach my goal. It became possible to accomplish my research work within the time frame because of his continual support and guidelines and for creating an environment of team work.

I am also grateful to Giorgio Burella, Jacopo Fragasso and Nicola Fedeli, graduate students in our research group for their valuable suggestions and time they spent while performing this research activity.

Finally, I would like to express very special thanks to my beloved parents and wife. I was away from them for two years. They always tried to energize me from thousands of miles away with their inspirational words.

This work was supported by InnovateNL through the IgniteR&D program [funding number: 211081].

We acknowledge SIKA AG for the Viscoelastic Materials kindly provided for the tests presented in this thesis.

Thanks to University of Trieste, Italy for the collaboration while doing this research activity.

Table of Contents

List of Tables:

List of Figures:

List of Abbreviation and Symbols

E_1 = the Young's modulus of the base beam

E_2^* = complex Young's modulus of VEM

f_{0n} = the resonance frequencies of the un-damped beam

H_1, H_2 = the thickness of base beam

h_2 = The ratio of the thickness of base beams

m_A = the mass of accelerometer

λ_n = the length of pinned-pinned beam

ω_n = The nth modal frequency of beams

ξ_n = The eigenvalue of each mode of vibration of the beams

ρ = Density

A = Cross sectional area of the beam

η = Loss factors

$\Delta\omega$ = The band-width

ω_1, ω_2 = Corresponding frequencies 3 dB below the resonance frequency

ω_n = Resonance frequency of the *nth* mode

n_i = Modal density of subsystem, *i.*

η_i, η_{ii} = Internal loss factor of subsystem *i.*

η_{ij} = Coupling loss factor between subsystem *i* and *j*

ζ = Damping ratios

E_{ij} = Band and space averaged energy of vibration of subsystem *i* when only subsystem *j* is excited and

P_j = Band averaged power into subsystem *j.*

$S_{a1}(\omega)$= The spectral density of the acceleration at point 1

T_L = The transmission loss

I_L = The insertion loss

I_{LB} = The insertion loss base structure

M = Total number of excitation points.

N = Number of measurement points on the central panel of the deck.

f_k = *k-th* central frequency of each third-octave band

ν = Poisson's ratio

List of Appendices

Chapter 1: Introduction

1.1 Motivation

Mitigation of structure-borne noise and vibration is a concern in several engineering fields in order to improve performance and durability of the final product, or comfort and customer satisfaction where people are exposed to noise. In the maritime industry, noise and vibration reduction has become an important topic. Prolonged exposure to hazardous noise in living spaces on board vehicles can cause severe health problems. High noise levels can also impair oral communications or acoustic signals, thus implying a potential danger for life (Ferrari et al., 2005). On board vehicles, these issues arise due to the presence of powerful sources of noise such as propulsion engines, propellers, HVAC system and large machineries near cabins and working spaces (Ferrari et al., 2007). As an example, hazardous noise levels are typically found on fishing vessels. Fishing vessels are relatively smaller than other types of marine vehicles but there is a high number of on-board pieces of machinery. (Zytoon et al., 2012; Burella et al., 2019). High levels of noise and vibration also decrease the comfort levels in the crew cabins. Low level of comfort in the accommodation decks causes improper rest of crew members, decreasing their workplace efficiency and increasing the occurrences of injuries. On-board machinery, like diesel engines and generator sets are usually the main sources of structure-borne noise. Mitigation of structure-borne noise and vibration has been boosted in the last decades by the construction of ships with advance levels of design standards. For example, reduction of structure-borne noise and vibration on cruise vessels is an important design parameter to provide higher

levels of comfort for passengers and it is a key factor that makes the maritime market competitive in the present era (Ferrari et al., 2007; Biot et al., 2014). In addition to the steady-state on-board noise and vibration sources, entertainment systems and human activities also increase noise and vibration levels on cruise vessels and mega-yachts. It is also important to ensure on-board comfort levels for crewmembers working on other merchant vessels so that they can take proper rest, improving safety on board. For these reasons, shipyards and research institutes have focused their research activities on the development of effective methods to control noise and vibration energy generated by on-board sources, and to increase comfort levels on accommodation decks and in workplaces.

Damping materials, like viscoelastic materials (VEM) are widely used in the transportation industry as an effective measure to control on-board noise and vibration. Research activities have been done to characterize the damping materials. Nevertheless, few references are found in the literature covering structure-borne noise and vibration reduction in the marine industry by using VEM and still now there is a lack of standards and design procedures on the application of VEM to the ship's structures in order to reduce structure-borne noise and vibration. This study provides a better understanding on the effects of VEM to ship structures in order to provide ship designers with effective ways to simulate the dynamics of VEM when applied to ship structures.

1.2 Objective

In order to control structure-borne noise and vibration generated by on-board sources, a proper design of the insulation system and the dynamics of the structures should be carried out. Structure-borne noise and vibration can be controlled by using several strategies: absorption, use of barriers and enclosures, structural damping and vibration isolation (Jennifer et al., 2001). Increasing the damping of a system is one of the most effective way to control structure-borne noise and vibration. Damping refers to the dissipation of mechanical energy from a vibrating system usually by conversion into heat energy by means of some dissipation mechanisms. An added damping system is effective in reducing the vibration level of a system if the overall damping of the composite structure is increased significantly from its initial condition (De Silva 2007). Use of VEM as a damping source is a common practice in various engineering fields including aerospace, aeronautics, automotive and domestic appliances in order to minimize undesirable structure-borne vibrations and radiated noise (Pravin et al., 2014).

VEMs are rubber-like polymers with stiffness and damping characteristics that vary strongly with temperatures and frequency. VEM must be strategically applied to the structure or machinery in such a way that may vary according to the systems involved (Jones 2001). The goal of this kind of noise and vibration controlling system is to add VEM in such a way and in such locations as to ensure the greatest possible cyclic deformation of the damping material will occur as the structure vibrates in the modes of interest and to dissipate as much vibrational energy as possible during each cycle. Developing a proper damping treatment requires understanding of the dynamic

behavior of the structures where the material is applied, the deformation of the VEM during vibration of the structure and the damping properties of VEM.

There are two effective ways to apply VEM to any structure: free layer damping (FLD) and constrained layer damping (CLD). In the marine vehicles these two types of application systems are widely used in order to achieve desired level of structure-borne noise and vibration reduction. FLD consists simply of a viscoelastic coating sufficiently applied to a beam or plate surface to increase the damping of the coated member. Damping properties of VEM applied in FLD configuration can be found by means of an equation first introduced by Oberst (Jones 2001).

Another application of damping treatment is called shear or constrained layer damping treatment (CLD). In this case, the viscoelastic layer is constrained by another elastic layer, such as a metal sheet or plate. For a CLD treatment, the Ross-Kerwin-Ungar (RKU) equation can be applied accurately only to beam-like members with pinned-pinned boundary conditions. More complicated configurations with this type of treatment, such as stiffened panels, can be properly addressed only by means of finite element analysis, or dedicated experimental tests.

Other types of application treatment of VEM include tuned dampers and viscoelastic links, which must be developed as engineering devices to be applied at or between specific points in the determined dimensions, materials and locations to maximize the amount of energy dissipated cycle by cycle during vibration. Available theoretical formulae to characterize VEM are not applicable in every condition. That is why this research activity has been carried out with the following objectives:

- Design an experimental test to understand the effects of structural constraints and the thickness in the characterization of VEM
- Determine the most effective VEM configuration to reduce structure-borne noise and vibration
- Investigate the effectiveness of VEM to reduce structure-borne noise and vibration when it is applied to a ship's structure
- Ascertain the damping characteristics of VEM damped structure at low frequency range [0, 100] Hz
- Find out the damping characteristics of VEM damped structure in audio frequency range [100, 4000] Hz
- Calculate the loss parameters like, transmission loss, insertion loss and insertion loss base structure
- Develop a design approach to apply VEM so that, ship designers can consider the optimal application of VEM at the early design stage of the ship's structure

1.3 Structure of the thesis

The rest of this thesis is organized as follows: Chapter 2 provides a literature review focusing on the research activities already done in different transportation industries like, automotive, aeronautical and railway industries to increase on board comfort levels. This study will also demonstrate the lack of established design standards for use

of VEM in the maritime sector to control structure-borne noise and vibration. In this research activity, VEMs for marine applications were characterized by employing experimental test and numerical analysis. In Chapter 3 theoretical background about damping characteristics of VEM, modal behaviors and Statistical Energy Analysis (SEA) parameters are discussed. This Chapter also includes experimental test procedure of impact test with aluminum beams, modal analysis and statistical energy analysis with a full-scale deck panel. Chapter 4 presents the results found from FEA analysis and experimental test. The last Chapter will present concluding discussion on the contributions of this thesis with recommendation for future research.

Chapter 2: Literature Review

To control on-board noise levels, careful acoustical planning in the early design stage is needed and also various types of countermeasures should be put into practice to achieve the results. Noise and vibration control systems can be categorized into the active, passive, semi-active and hybrid method (Kandasamy et al., 2016). Use of VEM with any vibrating structure is a passive control method in which it is not required to have any external power source and it can utilize the motion of the vibrating structure to reduce structure-borne noise and vibration. VEM should be added to the base structure in a proper way and in such a location so that its greatest possible cyclic deformation can be achieved when the whole composite structure vibrates in its modes of interest. This requires an understanding of the dynamic behavior of the VEM which occurs during vibration of the structure. VEMs are applied to the structures in different configurations and those structures are connected to other parts with different boundary conditions. Therefore, it is important to investigate the influence of different boundary conditions on the vibration damping properties (resonance frequency, loss factor) of any damped structures. But at present, few references exist for the damping measurement of composite structures considering the effects of boundary conditions. For example, the Ross-Kerwin-Unger (RKU) equation can only be applied accurately to beams having pinned-pinned boundary conditions, but in case of other simple boundary conditions such as cantilever beam, free-free beam and clamped-clamped beams, we need to modify the RKU equation by finding out the semi-wave length of equivalent pinned-pinned beam.

The literature review reveals major research activities related to structure-borne noise and vibration control in railway, aeronautical and marine sectors. In the railway sector, significant research activities have been performed on the control of noise and vibration levels in train carriages by utilizing different anti-noise and anti-vibrational treatments to ensure comfortable train journeys. Fan et al. (2009) studied three major types of damping materials (bitumen-based damping material, water-based damping material and butyl-rubber damping material) which are normally used in train structure to mitigate noise and vibration. Measurements of noise and vibration levels were taken on three running train carriages (each of those were damped with the aforementioned damping materials separately) to investigate their damping effects in reduction of noise and vibration of railway vehicles. Finally, they suggested that the effects of damping treatments in railway vehicles depend on the train speed and that bitumen-based and water-based damping materials can reduce vibration levels in a wider frequency range (63 to 1000 Hz) than the last one. Thompson et al. (2007) and Alves Costa et al. (2012) also worked to increase on- board comfort levels in railway transportation.

In the aeronautical field, emphasis is on the reduction of noise and vibration to increase on-board comfort levels. Human response to aircrafts noise was studied by Schomer et al. (1987). Structure-borne noise and vibration in aircraft can be controlled in two ways: (a) acting directly on the primary source of noise and (b) increasing the attenuation and dissipation along the path of propagation (De Fenza, Angelo 2011). The latter is known as passive control system and is preferred in aeronautical field because of their lower complexity and cost. Rao (2003) described some of the recent industrial application of

passive damping technology (free layer damping, constrained layer damping) of VEM to control on-board noise and vibration in commercial airplanes.

Recently, on-board comfort in the maritime industry has become an important issue especially in cruise vessels and mega yachts. Research activities are performed to investigate the most effective way to increase on-board comfort in marine vehicles. For instance, an investigation of anti-noise treatment used on a ship's cabin floors was performed by Ferrari et al. (2005). They performed an experimental modal analysis with a full-scale deck panel of a fast ferry. Their study found the most effective configuration (viscoelastic constrained layer formed by steel plate, V+R+S) to control the noise level in cabin floors by developing several configurations of anti-noise treatment on the load carrying surface of the deck panel and measuring the acceleration on both the upper and lower surface of the system in a direction normal to the deck plate. In another study, they characterized the damping properties of VEM by performing an experimental test with a steel plate specimen. In their study they demonstrated the effects of environmental conditions of the test, like constraints, temperature and the positions of the instruments.

The mitigation of structure-borne noise and vibration in marine vehicles can also be achieved by applying empirical design procedures and by inserting isolating devices, which uncouple the source of vibration from the ship's structure. In addition, cabins are insulated and decoupled from the ship structures using insulating materials or floating floors (Moro et al., 2016; Fragasso et al., 2019). These solutions reduce the structure-borne noise and vibration energy transmitted from the sources to the ship structures and from the ship structures to the receivers. In the recent research of Moro et al. (2016),

design concepts for the selection of optimal resilient mountings for marine diesel engines and the development of new floating floors to improve comfort on board ships were analyzed. Fragasso et al. (2017) conducted an experimental activity with a steel plate at free-free boundary condition to investigate the optimal thickness of VEM for the application within the structures in FLD configuration as an effective means of structure-borne noise and vibration control. It was found from their analysis that, the increment of the thickness of VEM beyond 20% of the base material thickness will not provide any improvement to the damping effects. Recently, Vergassola et al. (2018) presented a new reliable and simple testing procedure with steel plate specimen for the determination of damping loss factor at free-free boundary condition. Their proposed method was also validated by comparing the estimated loss factors with finite element results and results obtained by statistical analysis. The effects of damping material thickness in the calculation of damping loss factors of CLD configuration at cantilever-free boundary condition has been studied by Hujare et al. (2014).

From the literature review, it is found that VEMs are widely used across different transportation industries as an effective measure to control structure-borne noise and vibration. Neverthless, there is no standard design methodology for the application of VEM to achieve maximum noise and vibration reduction in ships, so further research with VEM is required to meet the objectives as described in the previous Section. Those objectives can be achieved by the following ways:

- Characterization of VEM and studying the effects of boundary conditions in the calculation of damping parameters

- Experimental test with a ships deck panel to investigate the effects of VEM when it will be applied to ship structure at lower frequency range
- Statistical energy analysis to find out damping properties of VEM damped structures at audio frequency range.

Chapter 3: Methods

This Chapter presents the methodology used in the research activity. This Chapter is organized in the following sections that describe:

a) VEM configurations (Section 3.1)

b) Characterization of VEM and effects of boundary conditions (Section 3.2)

c) Description of mock-up used in our experimental test (Section 3.3)

d) Experimental test to find out damping properties at lower frequency range (Section 3.4)

e) Statistical energy analysis (Section 3.5)

Each Section is divided into several sub-sections to describe the related theory and the test set-up of each experiment.

In order to have a complete characterization of VEM, dynamic properties of VEM in the form of loss factors need to be calculated over a broad frequency range. This study analyzed the loss factor of VEM used on aluminum beams and the effects of VEM when applied to a more complex ship structure were also analyzed using a mock-up, specifically designed for this purpose. By performing impacts tests and statistical energy analysis with the simple beams and the structural mock-up, damping parameters were calculated at lower and higher frequency ranges respectively. The overall research methodology is presented below in the following flow diagram:

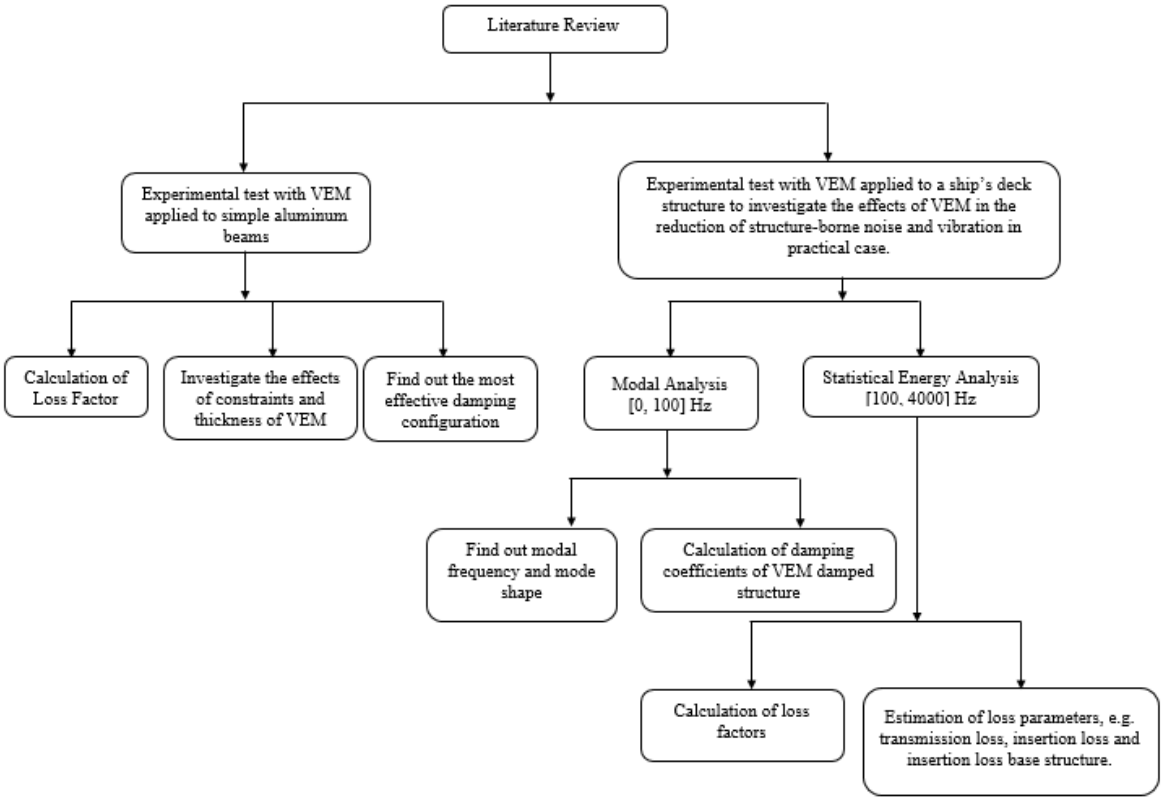

Figure 3.1: Flow chart presenting overall research procedures.

3.1 VEM Configurations

VEMs are treatments applied to the structural elements of a structure in order to increase its damping. These materials should be applied strategically to the structures in order to optimize their damping effect. Free layer damping (FLD) and constrained layer damping (CLD) are the most widely used damping configurations in marine structures. FLD is the simplest flexural damping treatment that consists of a layer of VEM directly applied to the bare structure (e.g. deck of a ship) at different thickness in order to increase its damping. In this damping treatment vibration energy is dissipated through cyclic deformation of the damping material, primarily in tension and

compression. In FLD, VEM is subjected to bending moment. The complex Young's modulus elasticity of VEM applied in FLD can be found from the Oberst (Jones 2001) as described below.

$$E_2^* = \frac{E_1}{2h_2}\left(\sqrt{(A_2^*)^2 + 4h_2^2(Z^* - 1)} - A_2^*\right) \quad (3.1)$$

Where E_1 is the Young's modulus of the base beam that can be calculated from the resonance frequencies of the un-damped beam (f_{0n}) from the following equation:

$$E_1 = \frac{48\rho_1\pi^2L^4(f_{0n})^2}{H_1^2(\xi_n)^4} \quad (3.2)$$

and:

$$Z^* = \left(\frac{\rho_1 bLH_1 + \rho_2 bLH_2 + 4m_A}{\rho_1 bLH_1 + 4m_A}\right)\left(\frac{f_n}{f_{0n}}\right)^2(1 + i\eta_n) \quad (3.3)$$

$$A_2^* = 5 + 6h_2 + 3(h_2)^2 - Z^* \quad (3.4)$$

$$h_2 = H_2/H_1$$

With H_1, H_2 the thickness of base beam and damping materials respectively and m_A is the mass of accelerometer used to measure the responses during the experiment. From the Oberst equations it is found that the values of Young's modulus are a function of the damping loss factors. In this thesis damping loss factors were calculated by conducting an experimental test with VEM used on simple aluminum beams.

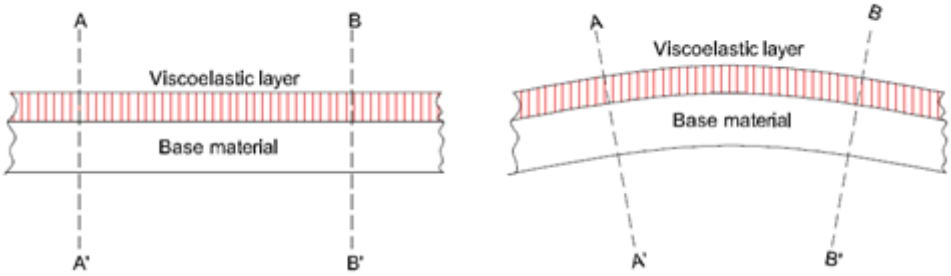

(a) Un-deformed (b) Deformed

Figure 3.2: FLD treatment in (a) un-deformed (b) deformed in bending.

CLD treatment is used to control noise and vibration of structures which are subjected to shear deformation by bonding a layer of VEM between the surfaces of two adjacent structures. CLD dissipates vibrational energy via shear cyclic deformation of the damping material. Using CLD, damping can be significantly increased with minimum impact on the total mass of the structure.

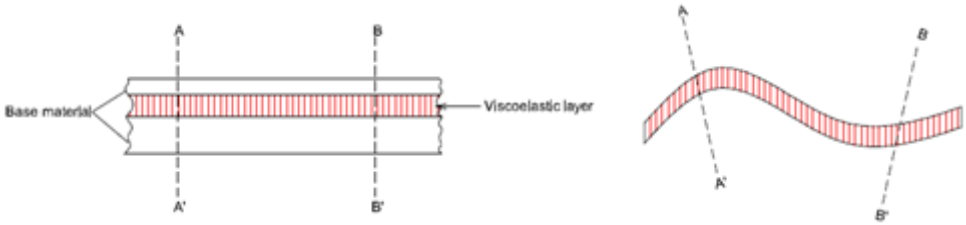

(a) Un-deformed (b) Deformed

Figure 3.3: CLD treatment in (a) un-deformmed (b) deformed in shear.

Flexural rigidity (which is defined as the resistance offered by a structure while undergoing bending) of a CLD structure can be calculated by the Ross-Kerwin-Ungar (RKU) equation. The RKU equation has been simplified considering equal thickness of both outer surfaces of CLD structure and by ignoring the bending effect of inner damping material (Jones 2001). That means, the complex Young's modulus of the

damping materials is negligible compared to the complex Young's modulus of the base beam in CLD. The simplified RKU equation can be described as below:

$$(EI)^* = E_1 H_1^3/6 + E_1 H_1 (H_1 + H_2)^2 g^*/(1 + g^*) \quad (3.5)$$

Where

$$g^* = G_2^* \lambda_n^2 / E_3 H_2 H_3 \pi^2 \quad (3.6)$$

Flexural rigidity $(EI)^*$ of CLD can also be calculated by measuring the response of the composite beam from the following equation:

$$(EI)^* = E_1 I_1 \left(1 + \frac{2\rho_2 H_2}{\rho_1 H_1}\right)\left(\frac{f_n}{f_{0n}}\right)(1 + i\eta_n)^2 \quad (3.7)$$

Where f_n is the n^{th} resonance frequency of the composite beam and f_{0n} is the n^{th} natural frequency of each base beam used in CLD. The RKU equations as described above are applicable only for beams having pinned-pinned boundary conditions. For beams having other types of boundary conditions, we need to calculate an effective semi-wave length λ_n, which is the length of an equivalent pinned-pinned beam having the same length, thickness and resonance frequency as the actual beam. In order to calculate the effective semi-wave length of an equivalent pinned-pinned beam, firstly, we need to calculate n^{th} modal frequency of both pinned-pinned beam and beam having other types of boundary conditions. For a pinned-pinned beam, the n^{th} modal frequency can be calculated from following formula (Jones 2001):

$$\omega_n = \left(\frac{\pi}{\lambda_n}\right)^2 \sqrt{\left(\frac{E_1 I_1}{b\rho_1 H_1}\right)} \quad (3.8)$$

Where λ_n is the length of equivalent pinned-pinned beam. The n^{th} modal frequency of beams having other types of boundary conditions can be calculated as described below:

$$\omega_n = \left(\frac{\xi_n}{L}\right)^2 \sqrt{\left(\frac{E_1 I_1}{b\rho_1 H_1}\right)} \tag{3.9}$$

From equations (3.8) and (3.9) we can calculate semi-wave length for an equivalent pinned-pinned beam as follows:

$$\lambda_n = \frac{\pi L}{\xi_n} \tag{3.10}$$

Where ξ_n is the eigenvalue of each mode of vibration of the beams. The effective semi-wave length of equivalent pinned-pinned beam of cantilever beam and free-free beam can be found from the eigenvalue of each mode of vibration. Eigenvalues of a cantilever beam and free-free beam can be calculated from its equation of motion (Mehmet 2010). A detail procedure to find out eigenvalues for cantilever beam and free-free beams has been presented by T. Irvine (2011).

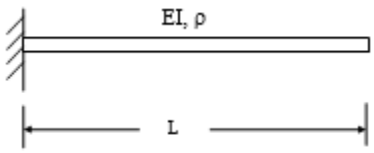

Figure 3.4: Cantilever beam

Let's consider a cantilever beam having length L, Young's modulus E, density ρ , and uniform cross-sectional area A. The equation of motion of this cantilever beam can be described as below:

$$EI\frac{\partial^4 y}{\partial x^4}+\rho\frac{\partial^2 y}{\partial t^2}=0 \tag{3.11}$$

The boundary conditions for a cantilever beam, at its fixed end, x=0; displacement, y(0)=0, slope, $\left.\frac{dy}{dx}\right|_{x=0}=0$ and at free end, x=L; bending moment, $\left.\frac{d^2y}{dx^2}\right|_{x=L}=0$ and shear force, $\left.\frac{d^3y}{dx^3}\right|_{x=L}=0$.

If y(x,t)=Y(x)T(t) is the solution of equation of motion of cantilever beam, then after substituting it into the equation (3.11) the equation of motion becomes as below

$$EI\frac{\partial^4[Y(x)T(t)]}{\partial x^4}+\rho\frac{\partial^2[Y(x)T(t)]}{\partial t^2}=0 \tag{3.12}$$

After separating the time (t) and displacement (x) variables and considering a constant term c it is found as like the following equations:

$$\frac{d^2}{dt^2}T(t)+c^2T(t)=0 \tag{3.13}$$

$$\frac{d^4}{dx^4}Y(x)-c^2\left\{\frac{\rho}{EI}\right\}Y(x)=0 \tag{3.14}$$

Equation (3.14) is a forth order differential equation. Let's consider the solution of this equation as below:

$$Y(x)=a_1\sinh(\beta x)+a_2\cosh(\beta x)+a_3\sin(\beta x)+a_4\cos(\beta x) \tag{3.15}$$

Therefore, $\frac{dY(x)}{dx}=a_1\beta\cosh(\beta x)+a_2\beta\sinh(\beta x)+a_3\beta\cos(\beta x)-a_4\beta\sin(\beta x)$ (3.16)

$$\frac{d^2Y(x)}{dx^2} = a_1\beta^2\sinh(\beta x) + a_2\beta^2\cosh(\beta x) - a_3\beta^2\sin(\beta x) - a_4\beta^2\cos(\beta x) \qquad (3.17)$$

$$\frac{d^3Y(x)}{dx^3} = a_1\beta^3\cosh(\beta x) + a_2\beta^3\sinh(\beta x) - a_3\beta^3\cos(\beta x) + a_4\beta^3\sin(\beta x) \qquad (3.18)$$

$$\frac{d^4Y(x)}{dx^4} = a_1\beta^4\sinh(\lambda x) + a_2\beta^4\cosh(\beta x) + a_3\beta^4\sin(\beta x) + a_4\beta^4\cos(\beta x) \qquad (3.19)$$

Now applying the boundary conditions and after some mathematical operations a matrix equation is found as below:

$$\begin{bmatrix} \sin(\beta L)+\sinh(\beta L) & \cos(\beta L)+\cosh(\beta L) \\ \cos(\beta L)+\cosh(\beta L) & -\sin(\beta L)+\sinh(\beta L) \end{bmatrix} \begin{bmatrix} a_1 \\ a_2 \end{bmatrix} = \begin{bmatrix} 0 \\ 0 \end{bmatrix} \qquad (3.20)$$

The determinant of this matrix is zero. Considering this condition finally equation (3.21) is found as below.

$$\cos(\beta L)\cosh(\beta L) = -1 \qquad (3.21)$$

By solving equation (3.21) we will find eigenvalues for a cantilever beam. Eigenvalues for a free-free beam can also be calculated by following the same procedure as described for cantilever beam. But the boundary conditions for a free-free beam will be changed as follow:

At x=0; bending moment $\left.\frac{d^2y}{dx^2}\right|_{x=L} = 0$, shear force $\left.\frac{d^3y}{dx^3}\right|_{x=L} = 0$ and at x=L; bending moment $\left.\frac{d^2y}{dx^2}\right|_{x=L} = 0$ and shear force $\left.\frac{d^3y}{dx^3}\right|_{x=L} = 0$.

Eigenvalues (ξ_n) and effective semi-wave length (λ_n) for cantilever beam and free-free beam are described in following Table 3.1 and 3.2:

Table 3.1: Eigenvalues and semi-wave length of cantilever beam.

Cantilever Beam		
Modes of vibration	Eigenvalues	Semi-wave length
1	1.87510	1.67L
2	4.69409	0.67L
3	7.85640	0.40L
4	10.9956	0.29L

Table 3.2: Eigenvalues and semi-wave length of cantilever beam.

Free-Free Beam		
Modes of vibration	Eigenvalues	Semi-wave length
1	4.73004	0.67L
2	7.85320	0.40L
3	10.9956	0.29L

These values allow us to calculate the semi-wave length of equivalent pinned-pinned beams for free-free beams and cantilever beams in order to use the RKU equations for finding the damping properties of VEM applied to the structures in these two boundary conditions. The semi-wave length of first, second, third and sub-sequenct modes of vibration of free-free beam is equivalent to the semi-wave length of second, third, fourth and sub-sequent modes of vibration of cantilever beam. This allows the transformation of cantilever constraint into free-free constraint. Thus the impact test procedures for cantilever beams described in ASTM can also be used for free-free boundary conditions. The detail about impact test and damping parameter estimation procedures are described below:

3.2 Characterization of VEM according to ASTM and Effects of Boundary Conditions

This experimental test has been carried out to calculate the damping loss factors of VEM applied on simple aluminum beams. The characterization of VEM has been done on the basis of these loss factors values. The detail of this experimental test and calculation of loss factors are described below.

3.2.1 Experimental Test Set-Up

The following experimental test was carried out with seven different sets of aluminum beams as shown in Figure 3.4, complying the ASTM standard. The goal of this experimental work is to investigate the effects of boundary conditions in the characterization of VEM in FLD and CLD configurations. That is why it is required to perform experimental test considering the cantilever beam and free-free beam boundary conditions for both FLD and CLD. Effect of free-free boundary conditions in the characterization of VEM is important as this type of boundary condition is common in characterizing VEM for marine applications . Fragasso et. al. (2017) and Vergassola et. al. (2018) focused on free-free beam boundary conditions in their recent research with VEM. Hujare et al. (2014) studied cantilever boundary conditions to investigate the effects of damping material thickness in the calculation of damping loss factors. Cantilever beams and Free-Free beams are found to be the most effective as those boundary conditions are easier to produce in practice than the other types of boundary conditions (Jones 2001). Base beams having the same characteristics were used in making the test specimen having the dimensions: length 440 mm, breadth 50 mm and

thickness 6.50 mm. All physical properties except the boundary conditions for each beam were kept constant in this experiment. The description of test specimens is presented in Table 3.3 and Figure 3.4.

Table 3.3: Dimensions and damping types of test specimens

Beam No.	Damping configuration	Thickness of VEM (mm)
Beam-1	Bare Beam	-----
Beam-2	FLD	1.00
Beam-3	FLD	2.00
Beam-4	FLD	4.00
Beam-5	CLD	1.00
Beam-6	CLD	2.00
Beam-7	CLD	4.00

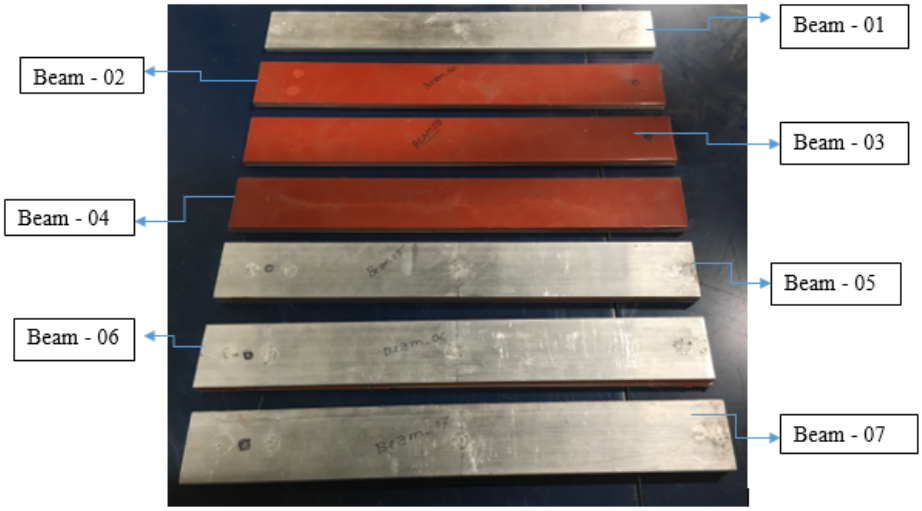

Figure 3.4: Test specimen for first experiment.

In the case of cantilever beams, one end of each specimen was kept in fixed support by placing it horizontally in a rigid steel test fixture as shown in Figure 3.5. Piezoelectric accelerometers were used to acquire signals. The data acquisition software LabVIEW® was used to record vibrational signals. The exciting force was provided at one end with an impulse hammer, which is equipped with a force sensor (load cell) on its tip. In the free-free condition, each beam was suspended horizontally using an elastic wire, as shown in Figure 3.6. Two piezoelectric accelerometers were placed on both ends at the same distance from each end as shown in Figure 3.6. Vibrational signals were recorded through the data acquisition devices by exciting the beam at its mid-point with the same impulse hammer as was used to excite the cantilever beam.

Figure 3.5: Experimental test with cantilever beam.

Figure 3.6: Experimental test with free-free beam.

In each experimental test, the impact of the hammer provided the trigger for the time acquisition. The time-domain force signals and acceleration signals were recorded for each beam. All signals were recorded in time-domain samples at sampling rate of 4096 Hz. The vibration signals were truncated by using exponential windows. Signals from accelerometer and hammer load cell were processed by Fourier Transform (FT) in order to calculate Frequency Response Function (FRF) which is defined as the ratio of output response and input force. The FRF was calculated from 0 – 2.0 KHz at a frequency interval 0.10 Hz. Coherence and Phase of FRF were also calculated to verify reliability of our recorded signals. Damping characteristics in the form of loss factors were calculated from the FRF as discussed in the following section.

3.2.2 Calculation of Loss Factors

Loss factor is an important damping measuring parameter of any damped structure (De Silva 2000). It is also considered as a useful design parameter to control structure-borne noise and vibration (ASTM 2010). Loss factor can be defined as specific damping capacity (ratio of energy dissipated in one complete cycle of motion to the initial energy

of the system) per radian of the damping cycle and can be expressed by the following equation:

$$\eta = \frac{\Delta U}{2\pi U_{max}} \tag{3.22}$$

Where ΔU is the amount of energy dissipated in one cycle and U_{max} is the initial energy of the system. There are several ways to measure damping loss factor. In this thesis, the half-power bandwidth method is used to calculate the loss factor of a single-degree-of-freedom (SDOF) system from its frequency response function (FRF) using the following formula (De Silva 2007):

$$\eta = \frac{\Delta\omega}{2\omega_n} \tag{3.23}$$

Where $\Delta\omega$ is the band-width and can be defined by the difference of ω_1 and ω_2, the corresponding frequencies at 3 dB below the resonance frequency (ω_n) as shown in Figure 3.7.

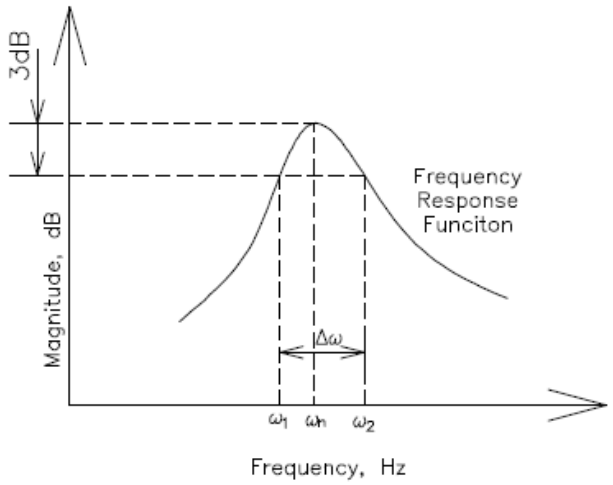

Figure 3.7: Half power bandwidth method

3.3 Mock-up for Dynamic Characterization of VEM When Applied to Ship Structures

To understand the effects of VEM when it is applied to the ships structures, experimental tests were performed with a ships deck panel specifically designed for this purpose. Experimental tests were carried out with this deck panel before and after application of damping treatment. The description of the mock-up and application of damping treatment are presented below.

3.3.1 Design of the Mock-up

A portion of a full-scale deck panel has been designed considering length, L=3.0m and width, B = 1.2m. It has been shown that, this small-scale deck panel represents similar dynamic behaviors as a full-scale deck panel (Fedeli. N., 2019). The deck panel is reinforced by two transverse primary girders and by two longitudinal angle stiffeners. The 3D view of the model is outlined in Figure 3.8 and the material properties are presented in Table 3.4.

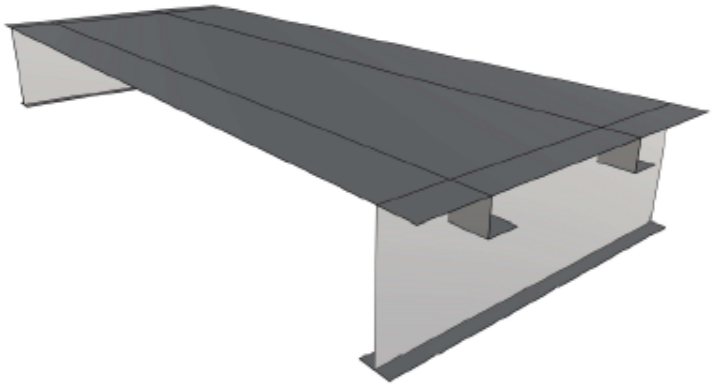

Figure 3.8: 3D view of the ship's deck panel

Table 3.4: Material properties of the deck panel

Property	Symbol	Value	Unit
Young's modulus	E	200.00	GPa
Poisson's ratio	v	0.30	-
Mass density	ρ	7850.0	Kg/m^3
Thermal expansion coeff.	α	$1.2x10^{-5}$	$^0C^{-1}$

The detail design of the deck panel is presented in Figure 3.9 to 3.11. The position of the collar plate and detail of the connection between main girders and stiffeners is presented in Figure 3.12. The main dimensions of the panel and the positions of the stiffeners and girders are summarized in the Table 3.5 and 3.6. The dimensions of the collar plate fitting in between the main girders and stiffeners connection are tabulated in Table 3.7.

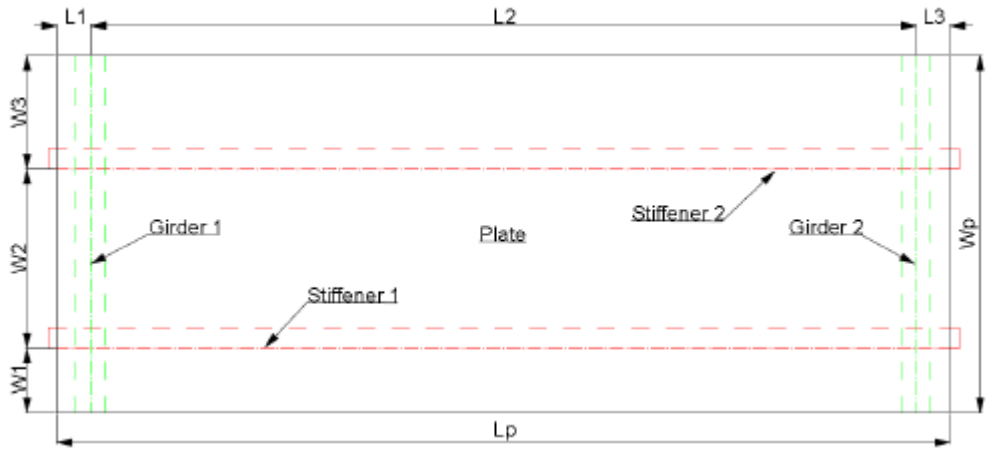

Figure 3.9: Top-view of the model

Table 3.5: Main dimensions of the panel

Dimension	Value	Unit
L_p	3.00	*m*
W_p	1.20	*m*
L_1	11.50	*cm*
L_2	277.00	*cm*
L_3	11.50	*cm*
W_1	21.80	*cm*
W_2	60.00	*cm*
W_3	38.20	*cm*

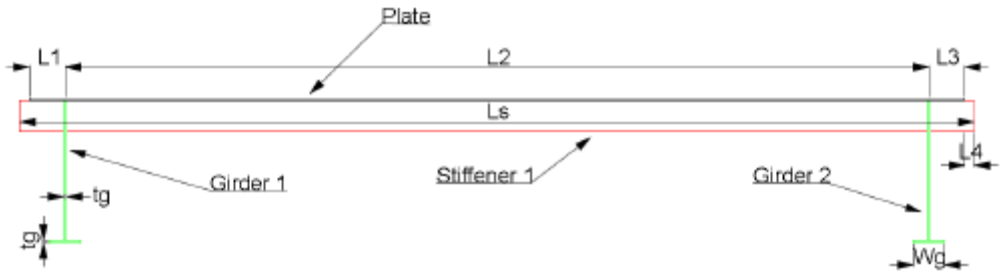

Figure 3.10: Front-view of the model

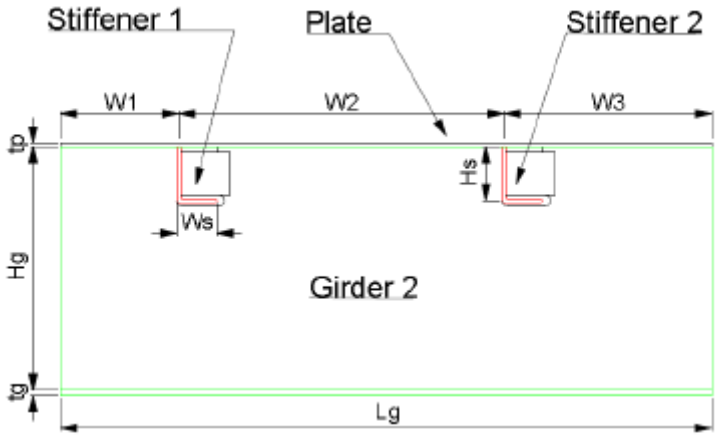

Figure 3.11: Right-view of the model

Table 3.6: Main dimensions of the main girders and stiffeners

Dimension	Value	Unit
L_g	1.20	*m*
H_g	45.00	*cm*
W_g	10.00	*cm*
t_g	10.00	*mm*

Dimension	Value	Unit
L_s	3.10	*m*
H_s	*10.00*	*cm*
W_s	*7.30*	*cm*
t_s	*7.00*	*mm*

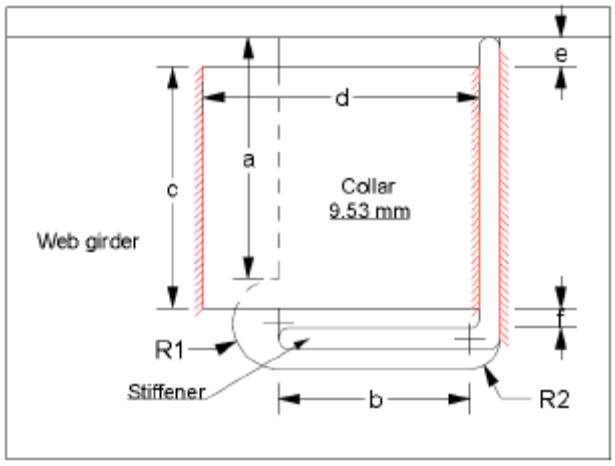

Figure 3.12: Detail of end connection between the stiffeners and girders

Table 3.7: Dimensions of collar plate position in between the stiffeners and girders connection

Dimension	Value	Unit	Dimension	Value	Unit
a	8.00	*cm*	*e*	1.00	*m*
b	6.35	*cm*	*f*	*0.65*	*cm*
c	8.00	*cm*	R_1	*1.50*	*cm*
d	9.15	*cm*	R_2	*1.00*	*cm*

To ensure the free movement of the deck panel in the vertical direction, the deck panel was placed horizontally on 4 stiff steel supports connected via four springs. The springs de-couple the panel from the fixed supports. To keep the panel in the correct vertical position, the upper part of each spring is inserted into a steel cylinder, welded on the girder's flange. The lower part of the spring is inserted into another steel cylinder, which is welded to a square steel plate laid down on the laboratory floor. The two cylinders have outer radius R_{cyl} = 11.00cm and the thickness is t_{cyl} = 10 mm. The detail of the spring supports is presented in the Figure 3.13. Both stiffeners and girders are connected to the plate by intermittent weld. The position and length of each weld is shown in Figure 3.14. the red lines represent the weld beads and the black lines represent the portions of the length of the girders and stiffeners which are not welded to the plate.

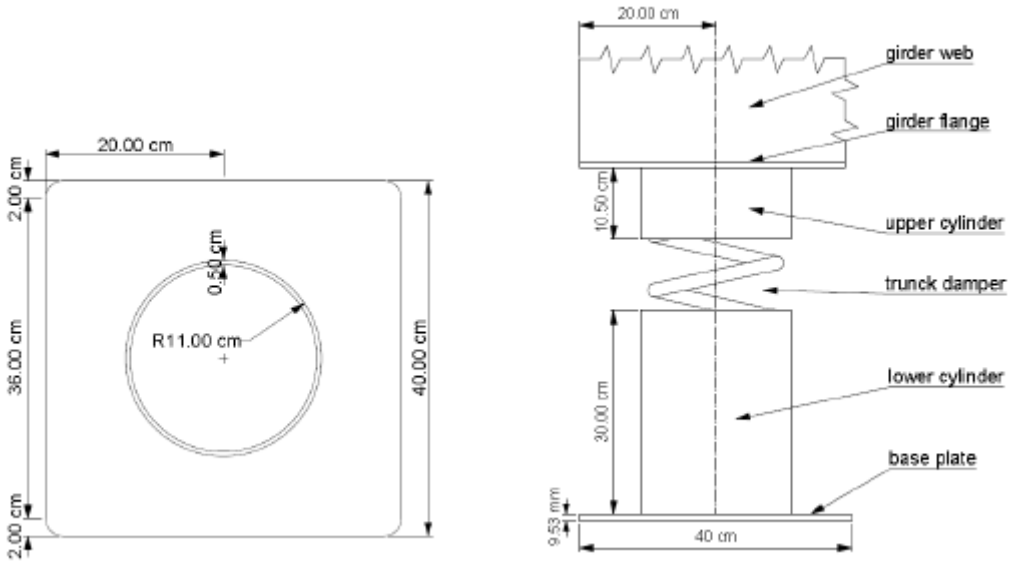

Figure 3.13: Top-view and front-view of the suspension system of the deck panel

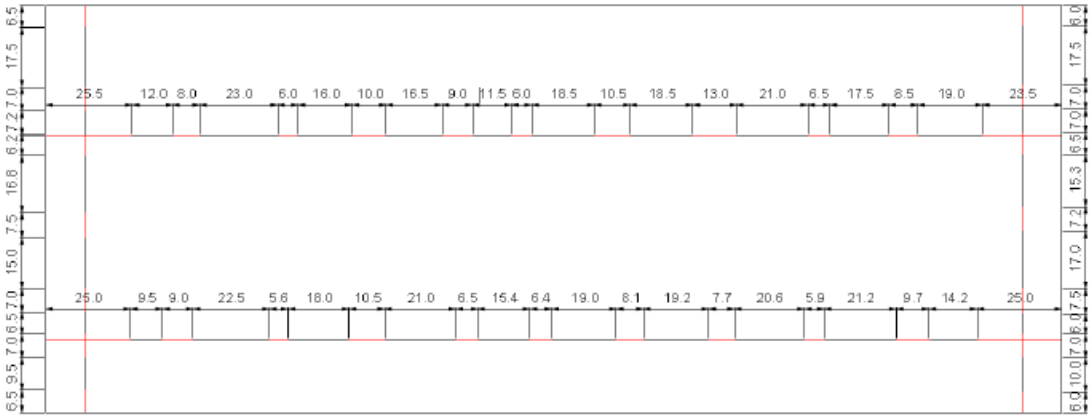

Figure 3.14: Intermittent welding between stiffeners, girders and plate

The total mass of the deck panel is 344.73 kg as it is measured by a laboratory weight scale. The deck panel fabricated in the university workshop is presented in Figure 3.15

Figure 3.15: The ship deck model

3.3.2 Application of the Damping Treatment

VEMs are usually applied to the deck panel and bulkheads. We applied VEM on the top surface of the deck panel in CLD configuration to investigate the effects of this damping treatment in the reduction of structure-borne noise and vibration in ship structure. The brand of the VEM we used is *Marine PU-Red* produced by *Sikafloor®* . This is a typical VEM for marine applications and made of two different components as shown below:

- Compound A: Is a red resin with density $\rho_A = 1300\ kg/m^3$ and viscosity $\mu_A = 20$ Pa.s.
- Compound B: Is the hardener with density $\rho_B = 1200\ kg/m^3$ and viscosity $\mu_B = 120$ Pa.s.

The resin and the hardener are mixed with a mixing weight ratio of 6:1 using a power drill with an appropriate mixing paddle for three minutes at least. The prepared compound is red in color. After mixing the compounds properly, the mixture was

applied on the base structure within 15 minutes. The damping material was applied with a homogeneous thickness of 1mm. Before applying the material, the panel surface was cleaned from dust, grease and other substances which may weaken the adhesion between the viscoelastic material and deck plate.

Table 3.8: Physical properties of compounds A and B of Marine PU-Red

	Density [kg/m^3]	Viscosity [Pa.s]	Color	Mixing ratio by weight
Compound A (Resin)	1.3	20	Red	6
Compound B (Hardener)	1.2	12	Brown	1

The constrained layer configuration of the viscoelastic material applied to the top surface of the deck panel consists 63 steel tails. The dimensions of steel tails are presented in Table 3.9. The positon of the steel tails and the its application measurement are presented in Figure 3.16 and 3.17 respectively. The deck panel after application of damping material is shown in Figure 3.18.

Table 3.9: Dimensions of the steel tails used in constrained layer configuration

Dimension	Value	Unit
L_{tail}	31.00	cm
W_{tail}	15.0	cm
t_{tail}	1.90	Mm
ρ_{tail}	7850.00	Kg/m^3

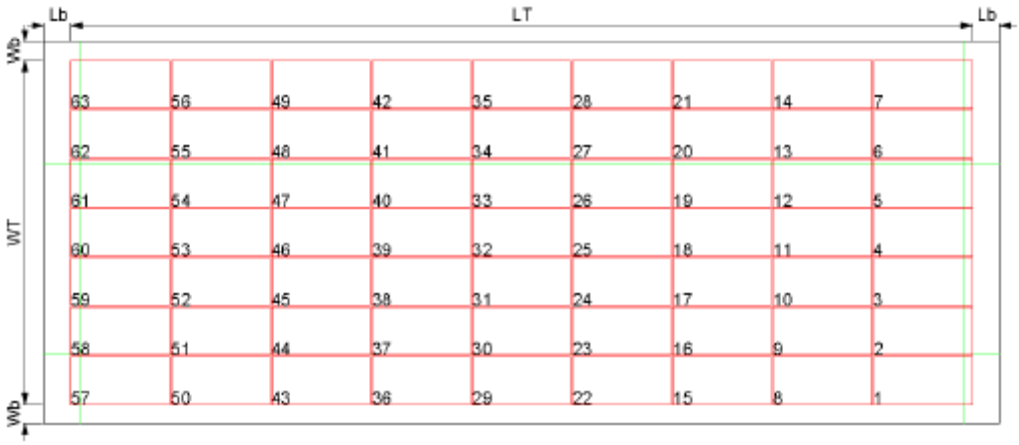

Figure 3.16: Position of the steel tails on the top surface of the deck plate

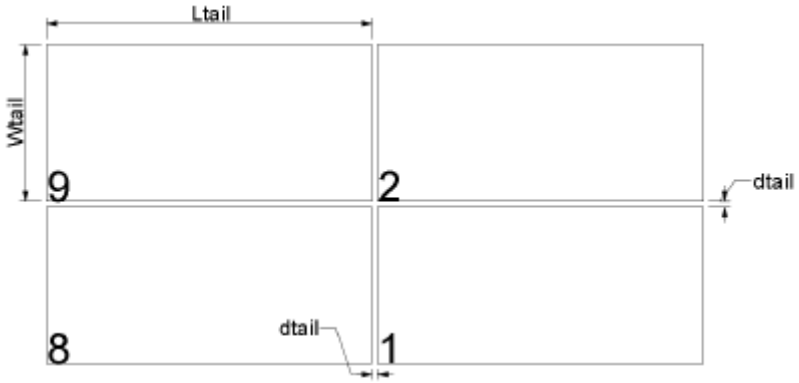

Figure 3.17: Detail of steel tails positioning

Table 3.10: Measurements of the steel tails position

Dimension	Value	Unit
d_{tail}	0.50	*cm*
L_b	8.50	*cm*
W_b	6.00	*cm*
LT	2.83	*m*
WT	1.08	*m*

Figure 3.18: The deck panel with viscoelastic damping treatment

The cross-section of the damping treatment is presented in Figure 3.19

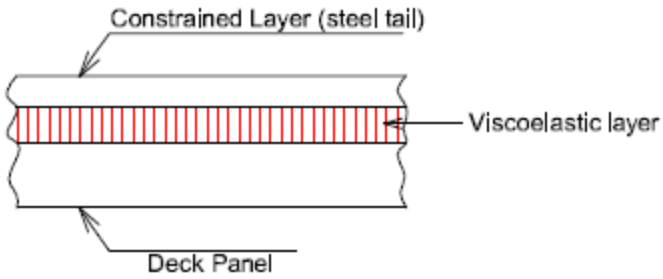

Figure 3.19: Deck panel with constrained layer viscoelastic layer.

3.4 Modal Analysis of the Experimental Mock-up

The concept of modal analysis plays an important role in the design of practical mechanical system. For this reason, it is important to study its effects on mechanical systems for different frequency ranges, i.e. low, medium and high frequency. Modal analysis allows us to evaluate detailed information about the dynamic behavior such as natural frequencies, damping coefficients and modal shapes of any structure. Those

results can be used to design proper anti-noise and anti-vibrational treatment. The configuration for any modal test takes in the form as shown by Lieven et al. (2001):

Input force, *f(t)* ⟶ *Structure* ⟶ Response, *x(t)*

The response to a given input force is normally derived from the equation of motion as stated below:

$$[M]\{\ddot{x}\} + [C]\{\dot{x}\} + [K]\{x\} = \{F(t)\} \quad (3.24)$$

Where M = mass matrix, C = damping matrix, K = stiffness matrix, x = displacement matrix and F = force vector. The natural frequencies and mode shapes are obtained by solving the eigenvalue problem (De Silva 2007).

In this thesis the effects of VEM applied to the ships structure were studied by means of numerical and experimental modal analysis in a low frequency range as described below.

3.4.1 Numerical Modal Analysis of the mock-up structures

Numerical modal analysis of the deck model was performed by using FEA software MSC. Nastran and MSC. Patran to understand how the system behaves in the design phase, the dynamic behaviors of the panel and the effects of boundary conditions. The numerical results were validated by performing experiments. The main features of the FEA model that was developed during the analysis are described below:

1. **Groups:** The elements of the deck model were organized into 05 groups.

1.1 Deck: This includes the flat plate of dimensions 3m x 1.2m x 0.008m. The difference between the dimensions of real case and numerical model is negligible.

1.2 Ordinary stiffener web: It is the vertical part of L - girder having width 100 mm and thickness 7 mm. The length of this part is 100 mm more than the length of the deck plate.

1.3 Ordinary stiffener flange: This is the flange (horizontal part) of L - girder having the width 70 mm, thickness 7 mm and the length is same as the length of the web as described above.

1.4 Main girder web: This is the main transversal part of main T-girder, having the dimensions, length = 1200 mm, width = 450 mm and thickness = 10 mm.

1.5 Main girder flange: This is the horizontal part of the T-girder, having the dimensions, length = 1200 mm, width = 100 mm and thickness = 10 mm.

2. Materials: The whole model is made of steel_ISO_SI, which has the following characteristics:

Young's modulus, $E = 210\ GPa = 2.1\ 10^{11}\ Pa$

Poisson's ratio, $\nu = 0.3$

Density, $\rho = 7800\ kg/m^3$

Thermal coefficient, = $1.2\ 10^{-5}\ 1/C^{\circ}$

3. **Element properties:** The model is defined by fully integrated shell elements. For each group the property of the corresponding shell elements has been defined. All the properties have the same Steel_ISO_SI material while each of them has a thickness compatible with, that stated in defining the groups, namely:
   Deck: 0.008m, Ordinary stiffener web: 0.007 mm, Ordinary stiffener flange: 0.007m, Main girder web: 0.01 m, Main girder flange: 0.001m.
4. **Mesh properties:** The mesh of the model consists of total 1067 nodes and 988 elements. There are 12 elements in width and 52 in length of the deck plate. The remaining elements are distributed along the main and ordinary stiffeners of the model.

3.4.2 Experimental Modal Analysis of the Mock-up

Damping characteristics of the VEM damped structure were calculated by performing experimental modal analysis at a low frequency range [0, 100] Hz. The test was carried out by exciting the model in some points on its deck plate and main girders. Total 217 grid points were marked on the model to survey the responses to the applied force both on the plate and main girders. 189 grid points were marked on the deck plate as shown in Figure 3.20 and remaining 28 points were marked on the two main girders as shown in Figure 3.21 and 3.22. The positions of those grid points are tabulated in Table 3.11. The response signal of each grid point was recorded using a piezoelectric accelerometer.

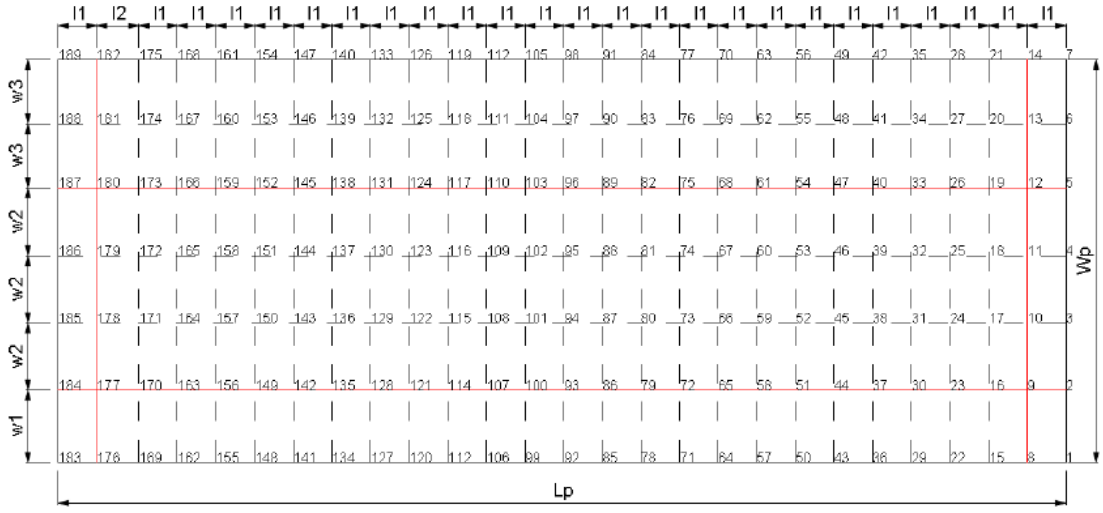

Figure 3.20: Grid marking on deck plate.

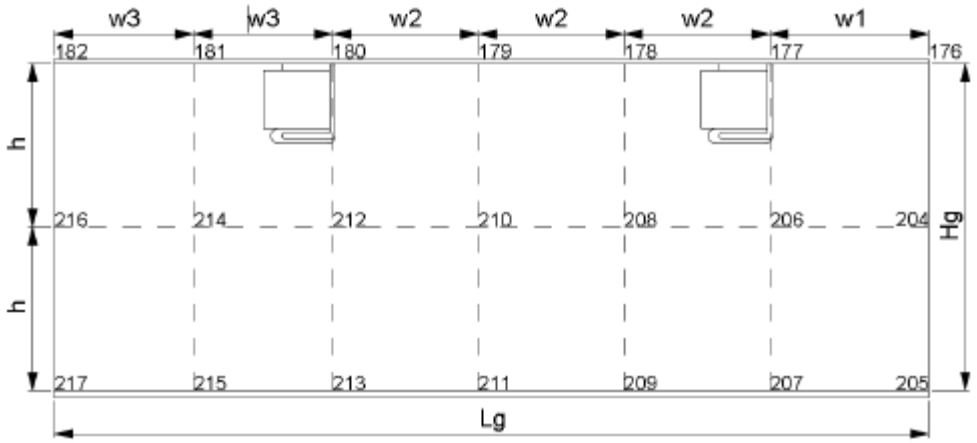

Figure 3.21: Grid point marking on girder 1

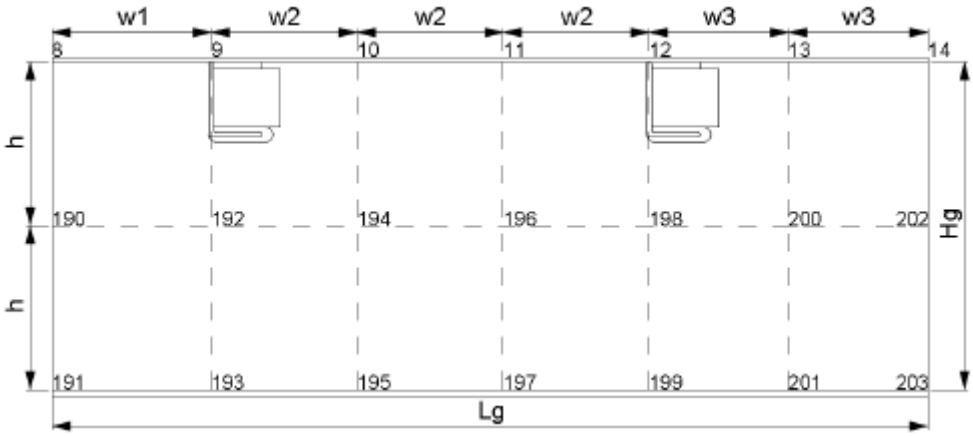

Figure 3.22: Grid point marking on girder 1

Table 3.11: Measurement of grid point on deck plate and main girders

Dimension	Value	Unit
l_1	11.50	*cm*
l_2	12.50	*cm*
w_1	21.80	*cm*
w_2	20.00	*cm*
w_3	19.10	*cm*
h	22.50	*cm*

The accelerometer was placed on 01 fixed point. Impact forces were applied in every point of the grid to acquire the response signal of each point. The impact forces were provided by a hammer instrumented with a load cell on its tip. For each measurement point, time signals of both applied force and response of the panel were recorded simultaneously. The signals of the accelerometer and the hammer load cell were recorded and processed by Fourier Transform in order to calculate Frequency Response Function (FRF). The data acquisition parameters were set in order to cover the frequency range up to 800 Hz. In addition to FRF, the coherence and phase of each

reading were also recorded to check the quality of data acquisition. Each FRF was calculated by averaging 5 time histories. Damping ratio and modal shape were found from the FRF curves. The same measurement technique was utilized to measure the responses before and after application of damping treatment.

3.5 Statistical Energy Analysis:

Statistical energy analysis (SEA) is one of the most reliable test procedures for audio frequency range structural vibration analysis. The excitation of the model is formed by the input power provided by the excitation into the subsystems. The SEA parameters describe the energy balance of subsystems and relate averaged power inputs and averaged energy levels of the subsystem through the following SEA equation.

$$\omega.[\eta^o].\{E\} = \{P\} \text{ and } n_i\eta_{ij} = n_j\eta_{ji} \quad (3.25)$$

where,

n_i = Modal density of subsystem, *i.*

η_i or η_{ii} = Internal loss factor of subsystem *i.*

η_{ij} = Coupling loss factor between subsystem *i* and *j*

E = Energy matrix

P = Power matrix

The modal density is the number of modes per unit frequency. It is the ratio of the number of natural frequencies per unit frequency. The internal loss factor of a subsystem is defined as the ratio of dissipated energy and the global subsystem energy

as it is described in previously. The coupling loss factor describes the energy exchange between subsystems. The coupling loss factor can be identified experimentally. Damping loss factors are fairly well known outside the SEA field. This is however not the case for the coupling loss factor, which are uniquely associated with SEA. Experimental approaches to find out these SEA parameters are described below:

3.5.1 Power Injection Method of SEA:

The power Injection Method (PIM) is based on the measurement of the appropriate power spectral densities of the responses and constitutes the most widely used technique to experimentally identify SEA parameters. This method depends on the measurement of the power input into the subsystems and of the vibrational kinetic energy as an estimate of the total vibrational, reverberant energy of the subsystem. PIM aims at identifying the SEA parameters by means of response measurements as a function of energy and power input measurement. From the mathematical viewpoint, this technique corresponds to the identification of the transformation matrix acting on the energy, *E* vector to produce the power, *P* vector:

$$\{P\} = \omega.[\eta^0].\{E\} \qquad (3.26)$$

The simplest and most obvious way of evaluating the transformation matrix is by evaluating the projection of the set of orthogonal unit vectors of *E* or of the *P* domain. For practical reasons, the images of the set of orthogonal unit vectors of the *P* domain will be determined. In PIM terms, the relevant equation is given by:

$$\{E\} = \frac{1}{\omega}[E^n].\{P\} \qquad (3.27)$$

The transformation matrix $[E^n]/\omega$ of this algebraic equation can be determined by evaluating the images of the basis x-vector:

$$\{P_1\} = \{1\ \ 0\ \ \dots\dots 0\}^T\ ; \{P_2\} = \{0\ \ 1\ \ \dots\dots 0\}^T\ ; etc.$$

The corresponding E-vector constitutes one single column of the transformation matrix $[E^n]/_\omega$. Hence, by applying the orthonormal basis vectors of the P domain, and evaluating the response in the E domain, it is possible to build up the normalized energy matrix.

3.5.2 SEA approach for Two-Subsystem Model:

Let's consider a two-subsystem SEA model as shown in the following Figure 3.23:

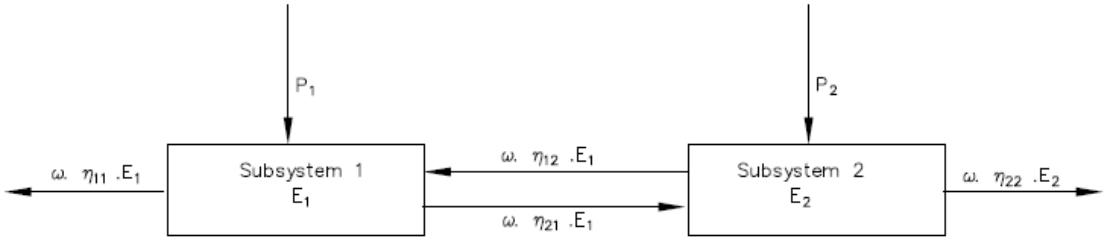

Figure 3.23: Two-subsystem SEA model

The basic SEA equations for a two-subsystem model becomes:

$$\begin{Bmatrix} P_1 \\ P_2 \end{Bmatrix} = \omega \begin{bmatrix} \eta_{11}^o & \eta_{12}^o \\ \eta_{21}^o & \eta_{22}^o \end{bmatrix} \begin{Bmatrix} E_1 \\ E_2 \end{Bmatrix} \tag{3.28}$$

If energy is injected into subsystem 1 by using white noise excitation. Hence, the above equation becomes:

$$\begin{Bmatrix} P_1 \\ 0 \end{Bmatrix} = \omega \begin{bmatrix} \eta_{11}^o & \eta_{12}^o \\ \eta_{21}^o & \eta_{22}^o \end{bmatrix} \begin{Bmatrix} E_{11} \\ E_{21} \end{Bmatrix} \tag{3.29}$$

Where;

E_{ij} = Band and space averaged energy of vibration of subsystem *i* when only subsystem *j* is excited and

P_j = Band averaged power into subsystem *j*.

Equation (3.38) can be normalized with respect to the power input by dividing the energies on the right-hand side of the equation by the power input. A non-dimensional energy level can be obtained by multiplying by the angular frequency. Equation (3.29) becomes:

$$\begin{Bmatrix}1\\0\end{Bmatrix} = \omega \begin{bmatrix}\eta_{11}^{O} & \eta_{12}^{O}\\ \eta_{21}^{O} & \eta_{22}^{O}\end{bmatrix}\begin{Bmatrix}E_{11}^{n}\\E_{21}^{n}\end{Bmatrix} \tag{3.30}$$

Where E_{ij}^{n} represents the normalized, frequency and space averaged energy of vibration of subsystem *i* when only *j* is excited, defined by:

$$E_{ij}^{n} = \frac{\omega . E_{ij}}{P_j} \tag{3.31}$$

Similarly, if energy is injected into subsystem 2 and if the energy of vibration is normalized with respect to the power input, the basic SEA equations become:

$$\begin{Bmatrix}0\\P_2\end{Bmatrix} = \omega \begin{bmatrix}\eta_{11}^{O} & \eta_{12}^{O}\\ \eta_{21}^{O} & \eta_{22}^{O}\end{bmatrix}\begin{Bmatrix}E_{12}\\E_{22}\end{Bmatrix} \text{ or } \begin{Bmatrix}0\\1\end{Bmatrix} = \begin{bmatrix}\eta_{11}^{O} & \eta_{12}^{O}\\ \eta_{21}^{O} & \eta_{22}^{O}\end{bmatrix}\begin{Bmatrix}E_{12}^{n}\\E_{22}^{n}\end{Bmatrix} \tag{3.32}$$

Combining the equations (3.39) and (3.41) we get:

$$\begin{bmatrix}1 & 0\\0 & 1\end{bmatrix} = \begin{bmatrix}\eta_{11}^{0} & \eta_{12}^{0}\\ \eta_{21}^{0} & \eta_{22}^{0}\end{bmatrix}\begin{bmatrix}E_{11}^{n} & E_{12}^{n}\\E_{21}^{n} & E_{22}^{n}\end{bmatrix} \tag{3.33}$$

Hence, the loss factors matrix $[\eta^0]$ can be obtained by inverting the normalized energy matrix $[E^n]$:

$$[\eta^0] = \begin{bmatrix} \eta_{11}^0 & \eta_{12}^0 \\ \eta_{21}^0 & \eta_{22}^0 \end{bmatrix} = \begin{bmatrix} E_{11}^n & E_{12}^n \\ E_{21}^n & E_{22}^n \end{bmatrix}^{-1} \tag{3.34}$$

The SEA coupling loss factors and internal loss factors are recovered by rearranging the terms of the total loss factor matrix $[\eta^0]$:

$$\begin{cases} \eta_{11} = \eta_{11}^0 + \eta_{21}^0 & \eta_{12} = -\eta_{21}^0 \\ \eta_{21} = -\eta_{12}^0 & \eta_{22} = \eta_{22}^0 + \eta_{12}^0 \end{cases} \tag{3.35}$$

The coupling loss factors and the internal loss factors are obtained without a knowledge of the modal densities. In other words, the reciprocity equation has not been used so far.

3.5.3 SEA approach for Multi-Subsystem Model:

In a similar way, the derivation of the PIM equations for a two-subsystem model can be extended to a multi-subsystem model.

- First energy is injected into subsystem 1. After normalization with respect to the injected energy and with respect to the angular frequency, the power input and the energy level of each subsystem are measured, resulting in the following set of SEA equations:

$$\begin{Bmatrix} 1 \\ 0 \\ \cdot \\ \cdot \\ 0 \end{Bmatrix} = [\eta^0]. \begin{Bmatrix} E_{11}^n \\ E_{21}^n \\ \cdot \\ \cdot \\ E_{n1}^n \end{Bmatrix} \tag{3.36}$$

- Next, energy is injected into subsystem 2, the energy levels are measured and normalized:

$$\begin{Bmatrix} 0 \\ 1 \\ \cdot \\ \cdot \\ 0 \end{Bmatrix} = [\eta^0]. \begin{Bmatrix} E_{12}^n \\ E_{22}^n \\ \cdot \\ \cdot \\ E_{n2}^n \end{Bmatrix} \tag{3.37}$$

The total loss factor matrix $[\eta^0]$ is given by the inverse of the measured energy matrix. To obtain the SEA parameter matrix $[\eta]$, the terms of $[\eta^0]$ have to be rearranged. The relationship between η_{ij} and η_{nk}^0 is given by:

$$[\eta^0] = \begin{bmatrix} \sum_{k=1}^n \eta_{1k} & -\eta_{21} & \cdots & -\eta_{n1} \\ -\eta_{12} & \sum_{k=1}^n \eta_{2k} & \cdots & \vdots \\ \vdots & \vdots & \ddots & \vdots \\ -\eta_{1n} & \cdots & \cdots & \sum_{k=1}^n \eta_{nk} \end{bmatrix} \tag{3.38}$$

Therefore, the coupling loss factors and internal loss factors are given by the following formulas:

$$\begin{cases} \eta_{ij} = -\eta_{ji} & i \neq j \\ \eta_{ii} = \sum_{k=i}^n \eta_{ki}^0 \end{cases} \tag{3.39}$$

3.5.4 Estimation of Loss Parameters

The last part of this thesis is the calculation of loss parameters, in the form of Transmission loss, Insertion loss and Insertion loss base structure (Ferrari et al. 2005). Those parameters are important to understand how much vibrational amplitude is reduced over broad frequency range after application of VEM on the radiating surface of the deck plate. The Transmission loss T_L is defined as the difference between the

vibration levels (expressed in decibels) acquired on the radiating surface and on the lower surface of the panel after the application of the damping treatment. The Insertion loss I_L is defined as the difference between the vibration levels (expressed in decibels) acquired on the radiating surface with and without the application of the damping material.

The Insertion loss base structure I_{LB} is defined as the difference between the vibration levels (expressed in decibels) acquired on the lower surface of before and after the viscoelastic material application. This parameter can be defined as the difference of the transmission loss and insertion loss, as presented below:

$$T_{LB} = T_L - I_L$$

Those parameters can be calculated from the formulae described below:

Transmission loss:

$$T_L(f_k) = \frac{1}{M}\frac{1}{N}\sum_{j=1}^{M}\sum_{i=1}^{N}\left(Mobility_{ij,DOWN\ WithVisco}\ (f_k) - Mobility_{ij,UP\ WithVisco}\ (f_k)\right)$$

Insertion loss:

$$I_L(f_k) = \frac{1}{M}\frac{1}{N}\sum_{j=1}^{M}\sum_{i=1}^{N}\left(Mobility_{ij,UP\ NoVisco}\ (f_k) - Mobility_{ij,UP\ WithVisco}\ (f_k)\right)$$

Insertion loss base structure:

$$I_{LB} = \frac{1}{M}\frac{1}{N}\sum_{j=1}^{M}\sum_{i=1}^{N}\left(Mobility_{ij,DOWN\ WithVisco}\ (f_k) Mobility_{ij,DOWN\ NoVisco}\ (f_k)\right)$$

Where:

M = Total number of excitation points.

N = Number of measurement points on the deck plate.

f_k= *k-th* central frequency of each third-octave band

$Mobility_{ij,DOWN\ WithVisco}$ is the mobility expressed in decibel measured in the *i-th* point of the deck when the excitation is applied in the *j-th* point of the main beams on the lower surface after the application of the viscoelastic.

$Mobility_{ij,UP\ WithVisco}$ is the mobility expressed in decibel measured in the *i-th* point of the deck when the excitation is applied in the *j-th* point of the main beams on the radiating surface after the application of the viscoelastic.

$Mobility_{ij,UP\ NoVisco} = Mobility_{ij,DOWN\ NoVisco}$ is the mobility expressed in decibel measured in the *i-th* point of the deck when the excitation is applied in the *j-th* point of the main beams on the radiating surface (equal to what would have been measured on the lower surface) before the application of the viscoelastic.

3.5.5 Experimental Test Set-Up

There are three available measurement strategies for experimental SEA as described by De Langhe (1996). Those measurement techniques are:

- First measurement strategy: Concentration of all instrumentation on one subsystem.
- Second measurement strategy: One response point and one excitation point on each subsystem.

- Third approach: Hybrid form.

In our case, SEA was carried out utilizing the first measurement strategy. This measurement strategy includes basically the acquisition of a sufficient number of FRF's such that all response instruments are concentrated on one subsystem. A short description of this measurement technique is given below for typical SEA with a structure having three subsystems and 4 excitation points on each subsystem, assuming the excitation has been provided using a shaker. The excitation points are indicated by (*) sign as shown in the following figures:

Step 1: Firstly, subsystem 1 is excited at one excitation point and responses are measured at each point indicated on subsystem 1. For each excitation on this subsystem one direct FRF and three indirect FRFs will be found. The same procedure will be repeated for remaining points on subsystem 1. So, total 4x4=16 FRFs will be recorded from subsystem 1 for exciting this subsystem at 4 points as shown in following figure. Thus, the structural energy E_{11} can be calculated.

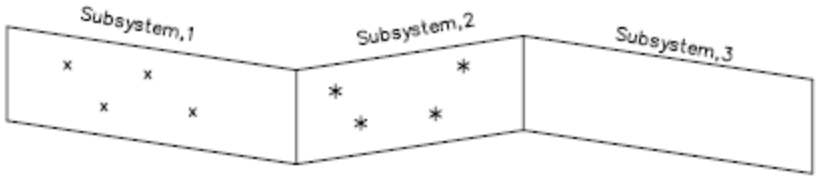

Step 2: Secondly, responses (indirect FRFs) are measured by shifting the accelerometers to subsystem 2 and 3 for exciting at each point on subsystem 1. In this case total 4x4 = 16 FRFs will also be found from subsystem 2 and 3 respectively. The structural energy E_{12} and E_{13} can be calculated from those FRFs. The direct FRFs found from each subsystem can be used to calculate input power.

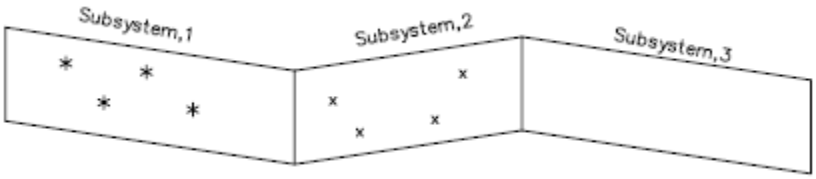

Step 3: The measurement techniques described in step 1 and 2 will be repeated for applying excitation on subsystems 2 and 3. Finally, the structural energy *[E]*, input power *[P]*, internal and coupling loss factor can be calculated utilizing the theoretical formulae described in previous section.

We performed SEA on the same deck panel used for modal analysis. A total of 3 subsystems have been considered in our analysis. The deck plate is defined by subsystem 1 and two main girders have been defined as subsystem 2 and 3 respectively as shown in Figure 3.25. For subsystem 1 and 3 only 4 points of excitation have been considered and total 8 points were considered for subsystem 2. The excitation points in each subsystem are shown in figure 3.26 to 3.28.

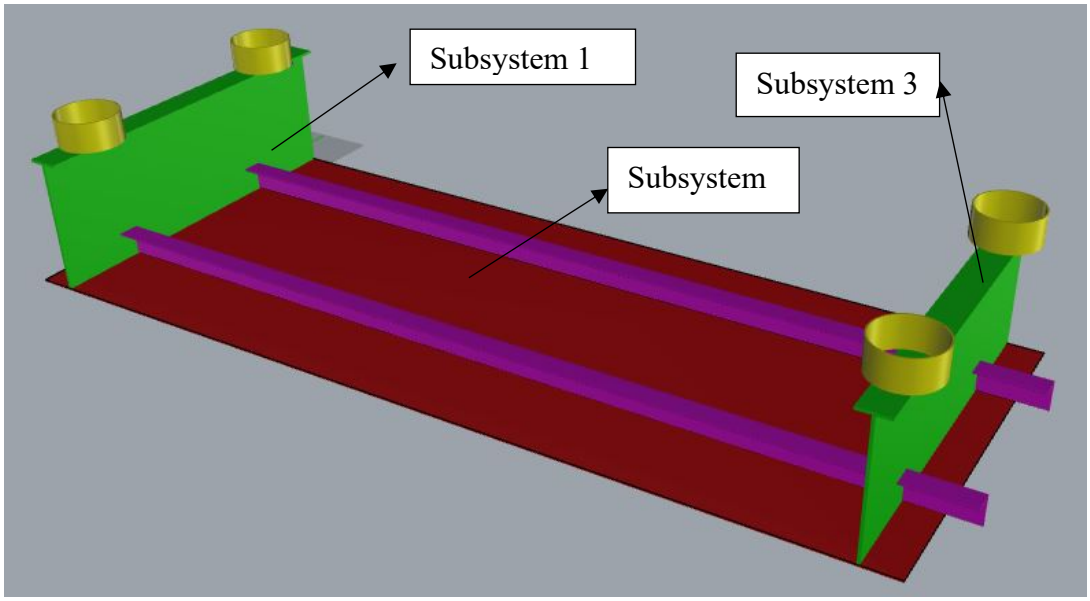

Figure 3.25: Geometry of deck panel and associate subsystems.

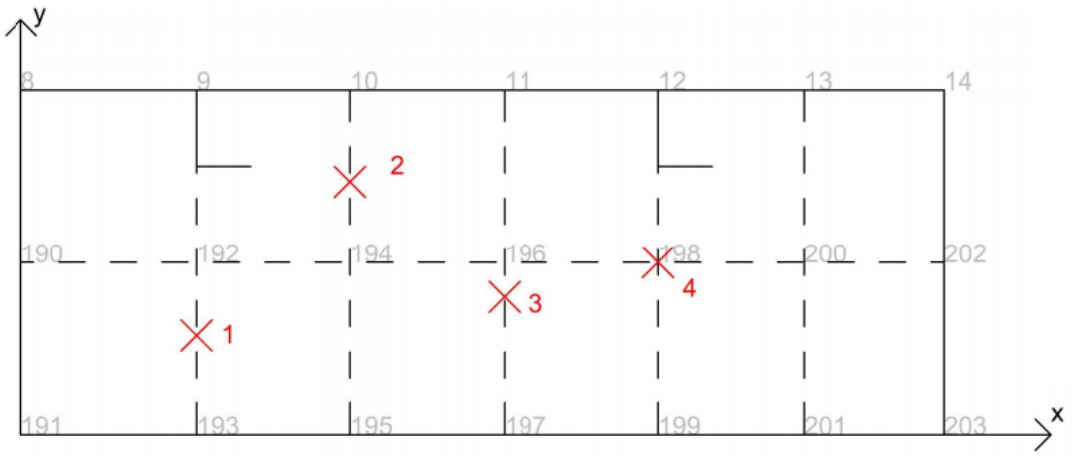

Figure 3.26: Point of excitation at subsystem 01

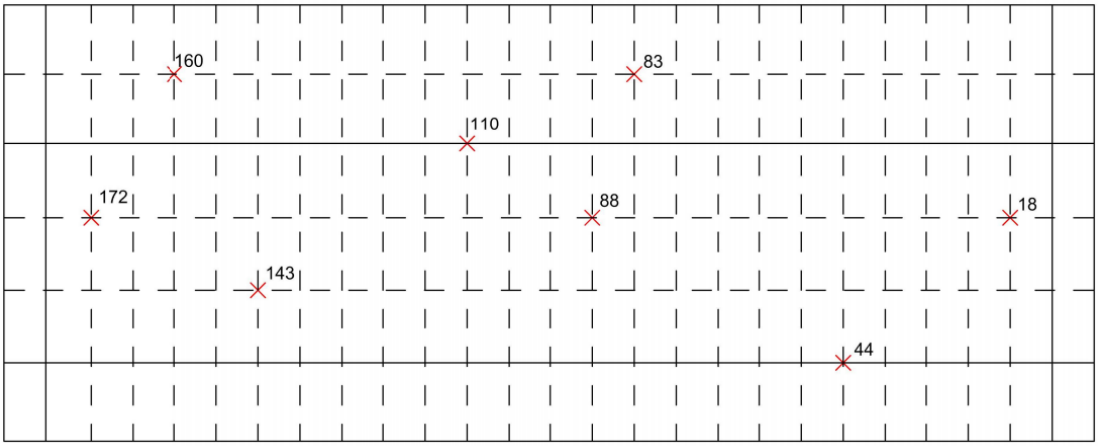

Figure 3.27: Point of excitation at subsystem 02

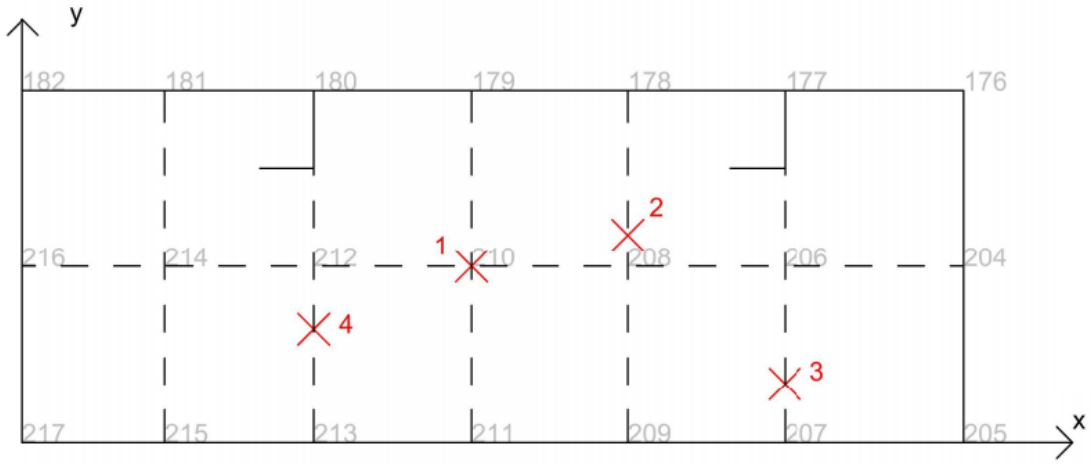

Figure 3.28: Point of excitation at subsystem 03

Figure 3.29: Shaker excitation on subsystem 1.

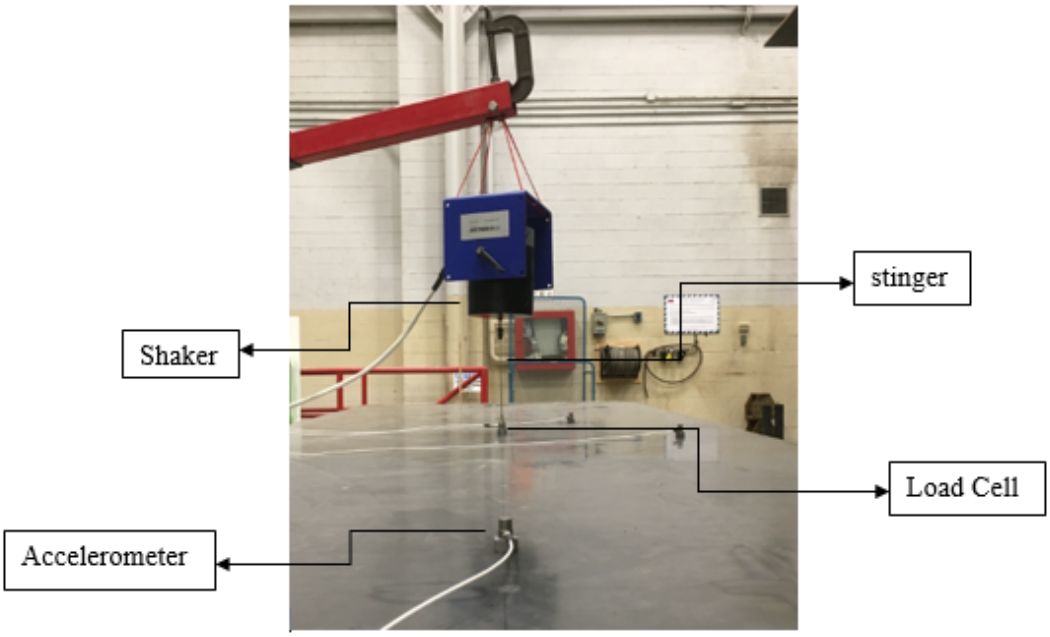

Figure 3.30: Shaker excitation on subsystem 2.

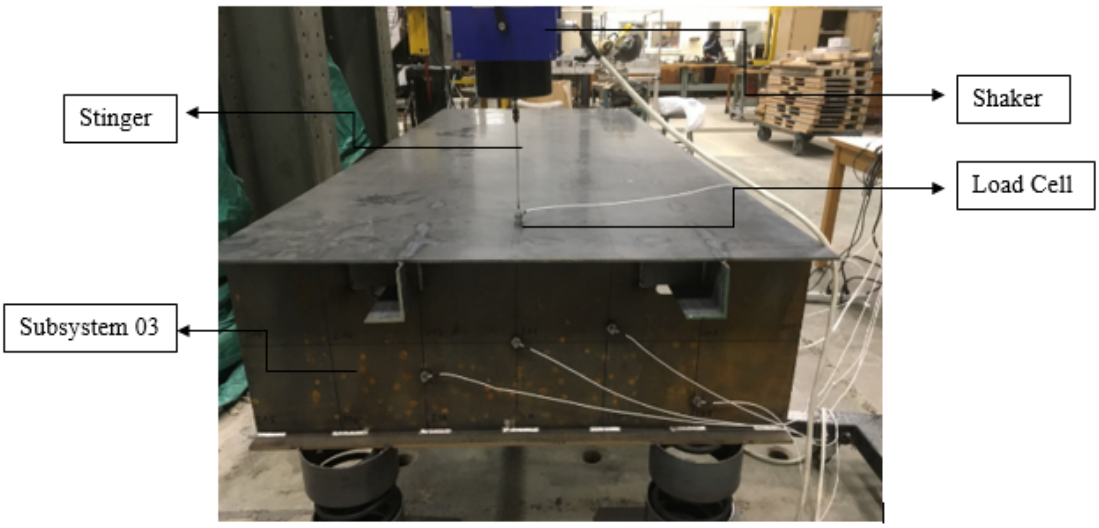

Figure 3.31: Response measuring on subsystem 3

A uniform white noise excitation was provided to the structure by an electro-magnetic shaker utilizing a white noise signal generated in LabVIEW® with an amplitude of 90 mV. The shaker is used to measure the responses at higher frequency range. The white noise excitation was amplified by an amplifier. The excitation force was transmitted to the structure from the shaker via a stringer rod. A piezo-electric load cell was positioned in between the connection of the subsystem and the stringer rod. The applied force signals were recorded through the load cell and the responses of the structure were measured at different points shown in the Figure 3.29 to 3.31 via four piezoelectric accelerometers. Both time-domain and frequency-domain signals were recorded using data acquisition software "LabVIEW Signal Express 2015". The frequency range during the test was set to 0-5000 Hz at frequency resolution 0.250 Hz. The vibration signals were windowed using Hanning window and final signals were saved after completion of averaging 5 (five) time histories. Frequency based signals, frequency

response functions (FRF) were calculated from time signals by means of Fourier Transform (FFT). Coherence and phases were also saved to verify the quality of acquired data. The experimental activities were performed following the first measurement strategy of experimental SEA as described before.

The Transmission and Insertion loss were calculated by measuring the responses at 10 (ten) points on subsystem 2. In this case excitation was provided on subsystem 1 and 3. Responses have been measured on both upper and corresponding points on bottom surfaces at each point for each excitation.

Chapter 4: Results

The outcomes of the research activity are presented in this Chapter. This Chapter is divided into three Sections to present the results of the experimental test performed with VEM damped beams, numerical and experimental modal analysis and SEA respectively.

4.1 Results of Impact Test to Characterize VEM According to ASTM and Effects of Boundary Conditions

FRFs, defined as the ratio between the measured acceleration and the input force (i.e. accelerance), of VEM damped beams are calculated in free-free and cantilever boundary conditions and have been compared with the FRFs of a bare beam in order to highlight the effects of the thickness in the characterization of VEM. Comparison among the FRFs found for all FLD and CLD beams in cantilever and free-free boundary conditions is shown in Figures 4.1 to 4.3. These plots present the effects of thickness in the characterization of VEM in cantilever and free-free boundary conditions.

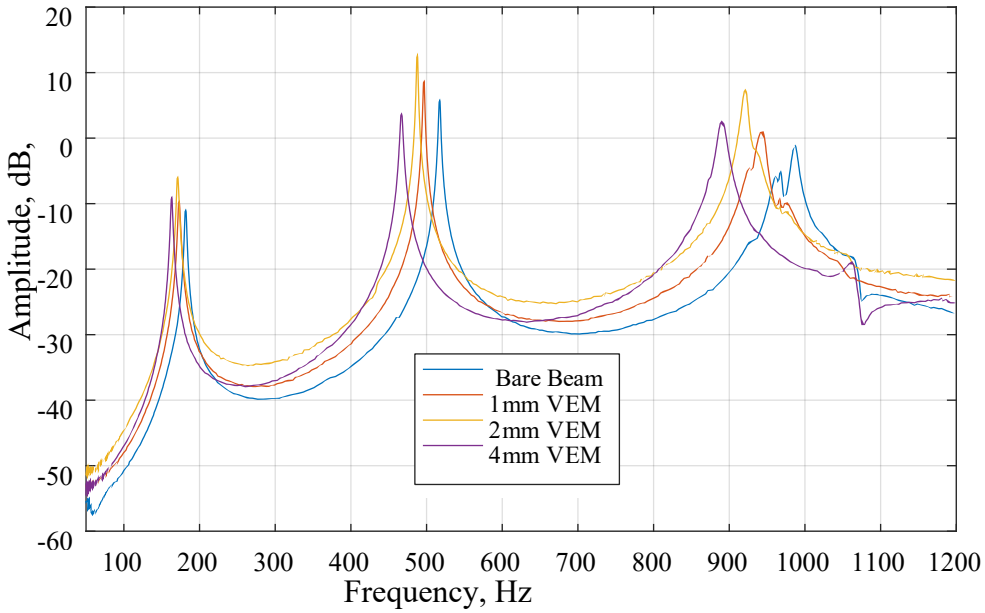

Figure 4.1: All FRFs in cantilever boundary condition for FLD beams.

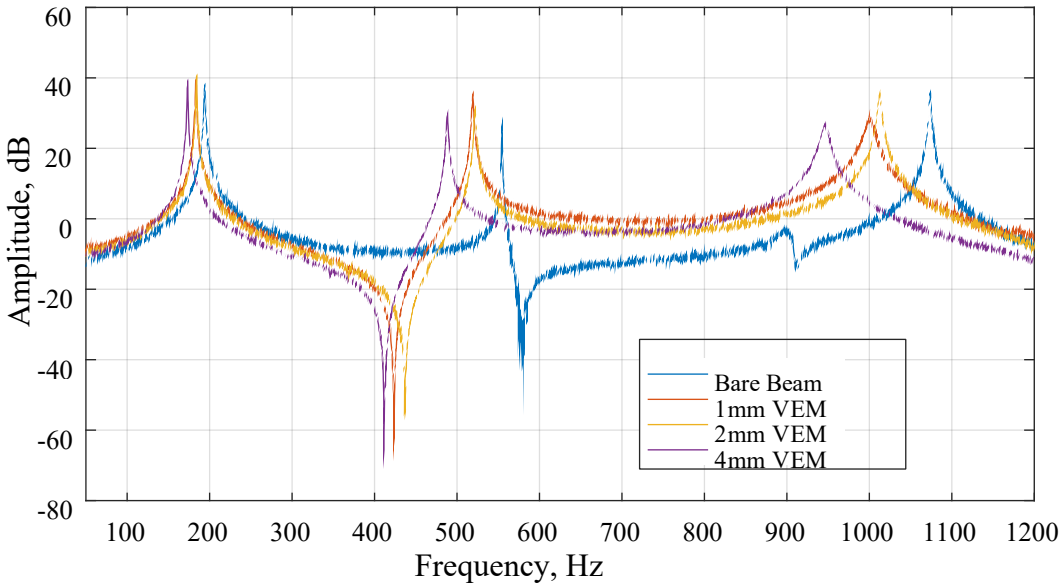

Figure 4.2: All FRF in free-free boundary condition for FLD beams.

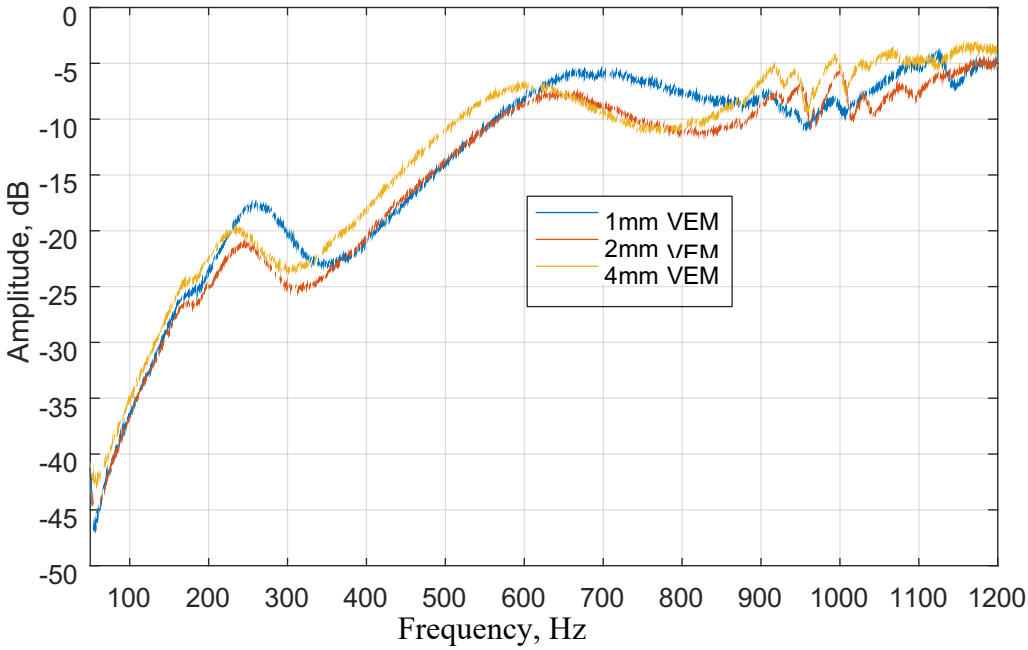

Figure 4.3: All FRF at cantilever boundary conditions for CLD beams.

To understand the effects of boundary conditions in characterization of VEM, the FRFs of each beam calculated in cantilever and free-free boundary conditions are also compared. In Figure 4.4 the accelerance measured for beam-02 in both boundary conditions is presented.

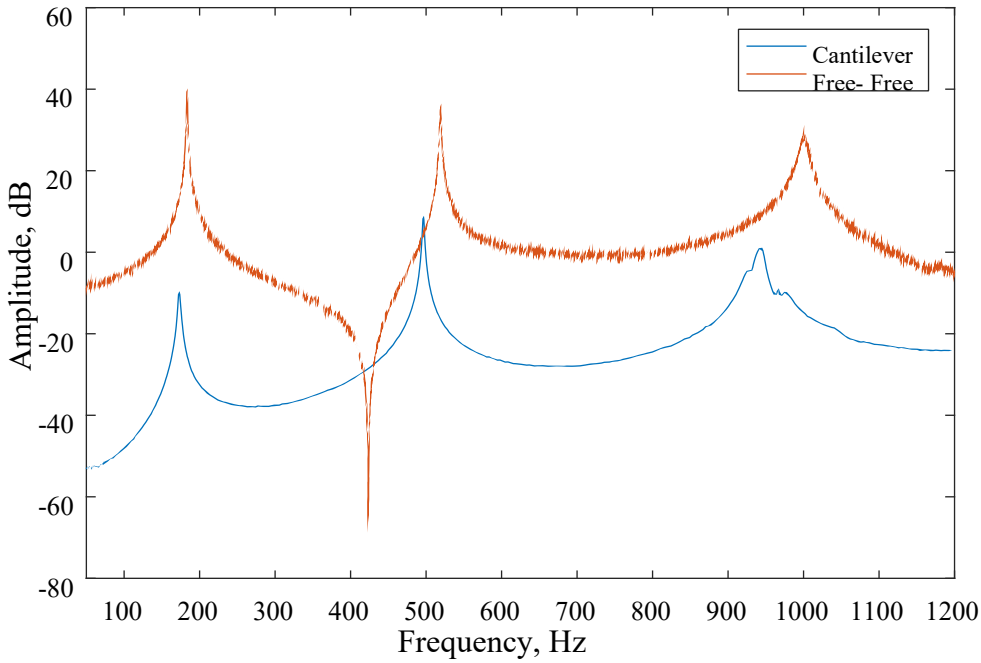

Figure 4.4: FRF of beam-2 at free-free and cantilever boundary conditions.

Loss factors estimated for each FLD beam in cantilever and free-free boundary conditions are plotted as function of frequency in Figure 4.5 and 4.6 respectively.

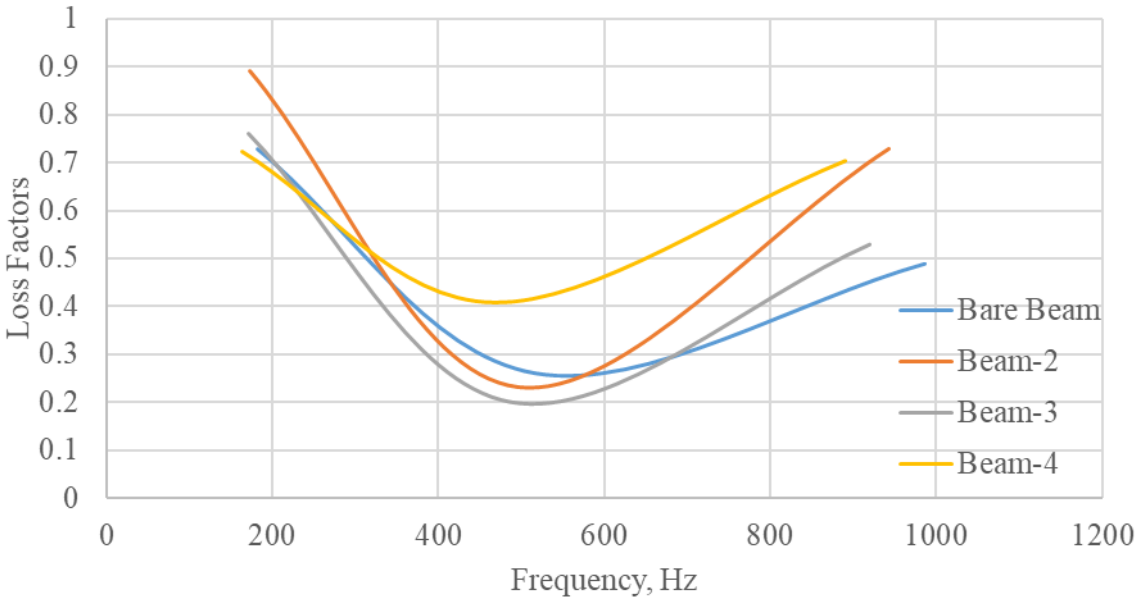

Figure 4.5: Comparison of loss factors at cantilever boundary condition for FLD.

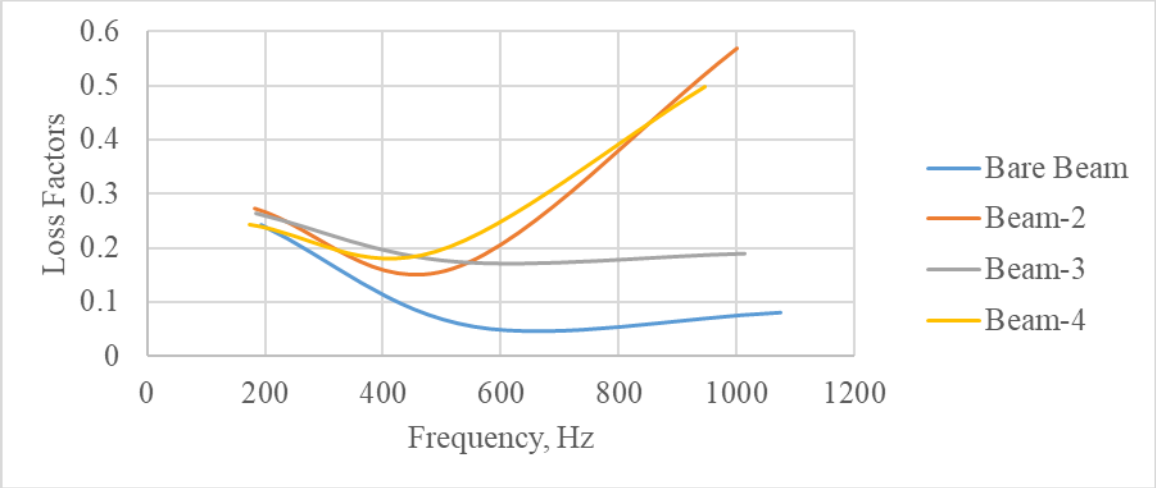

Figure 4.6: Loss factors at free-free boundary condition for FLD.

We cannot present the loss factors of CLD in both boundary conditions because in CLD treatment all the vibrational modes are over damped and the half power band width method to calculate the damping loss factors cannot be applied. Subsidiary results of impact test are presented in appendix–A.

4.2 Modal Analysis of the experimental mock-up

4.2.1 Numerical Modal Analysis of the mock-up structure

Natural frequencies and modal shapes are calculated using Finite Element numerical modal analysis. The modal frequencies are computed numerically in the frequency range [0, 100] Hz before and after the application of the damping treatment. Those values are presented in Table 4.1.

Table 4.1: Numerical natural frequency

Mode No.	Natural frequencies Without damping, f [Hz]
1	0.00
2	0.00
3	0.00
4	3.10
5	4.06
6	5.61
7	8.52
8	22.94
9	29.31
10	32.19
11	35.49
`12	39.89
13	41.17
14	43.10
15	47.77
16	51.50
17	60.84
18	63.36
19	67.65
20	75.78
21	81.28
22	90.45
23	92.16

Mode No	Natural frequencies With damping, f [Hz]
1	0.00
2	0.00
3	0.00
4	2.91
5	3.88
6	5.27
7	8.12
8	21.00
9	29.01
10	29.88
11	33.98
`12	37.34
13	39.51
14	42.82
15	43.38
16	48.66
17	54.52
18	57.02
19	62.80
20	67.80
21	72.80
22	81.43
23	82.72
24	91.92
25	92.74
26	96.72
27	98.03

Numerical modal shapes are presented in Figures 4.17 to 4.22 where they are compared with the experimental mode shapes.

4.2.2 Experimental Modal Analysis of the mock-up structure

FRFs are measured experimentally before and after the application of damping treatment and the results are presented in Figures 4.7 and 4.8 respectively.

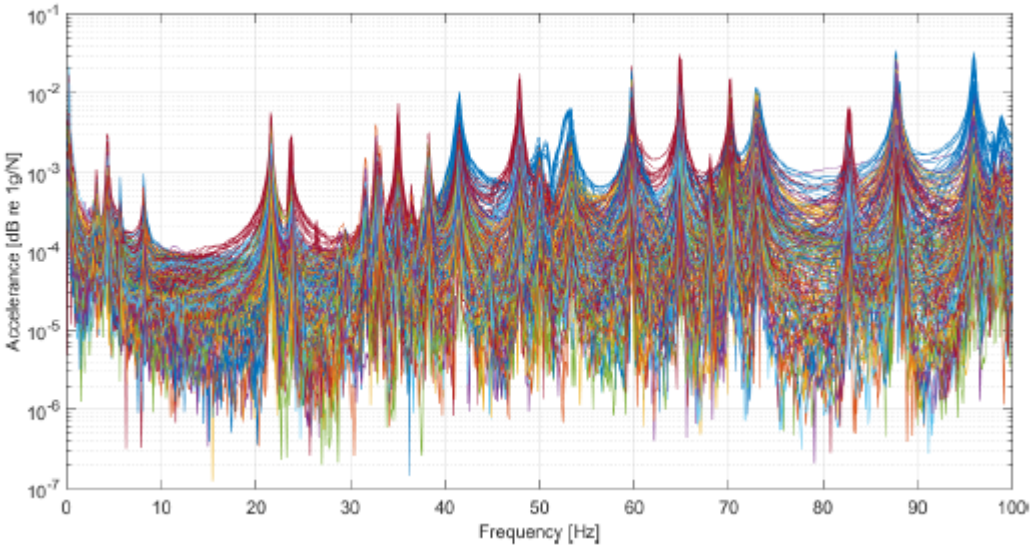

Figure 4.7: Experimental accelerances in frequency range [0, 100] Hz without VEM.

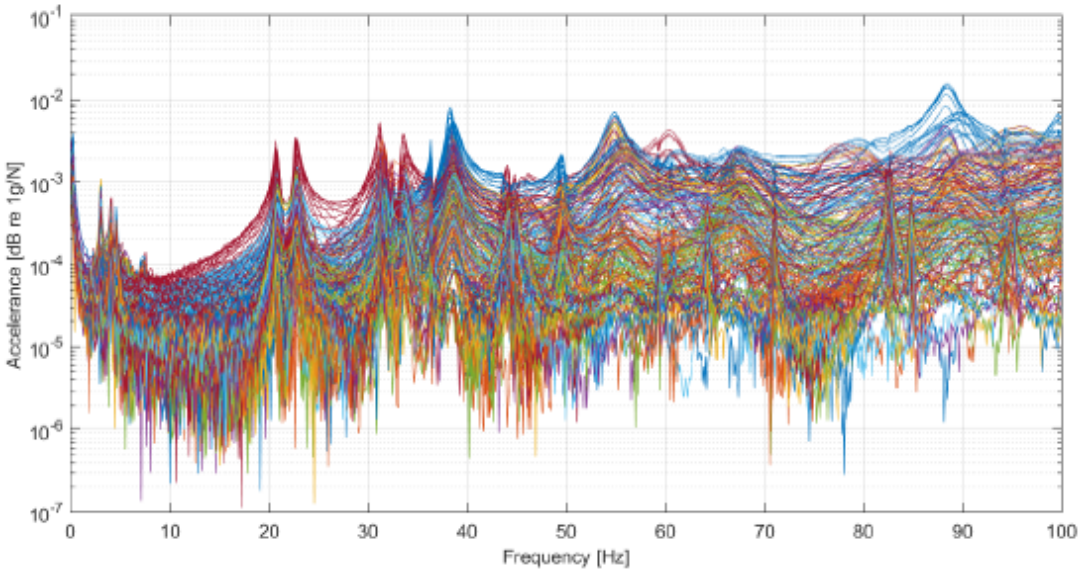

Figure 4.8: Experimental accelerances in frequency range [0, 100] Hz with VEM.

Those FRFs are expressed in terms of accelerance (dB) within the frequency range [0, 100] Hz and processed using the Matlab toolbox Abravibe to estimate experimental natural frequencies and damping ratios. These are calculated from the stability diagram generated from a total number of 217 FRFs. For example, the stability diagram within the frequency range [80, 90] Hz is presented in Figure 4.9 where the modal order, that indicates the mode numbers is presented in frequency domain. The green marks indicate the stable poles and the red circles indicate the unstable poles. The blue curve presents the mode indicator function, defined as real valued frequency dependent function that exhibits minima or maxima at the modal frequencies of the system. Experimental natural frequencies and damping ratios found from the stability diagram in the cases with and without VEM are presented in Table 4.2 and plotted in Figure 4.10.

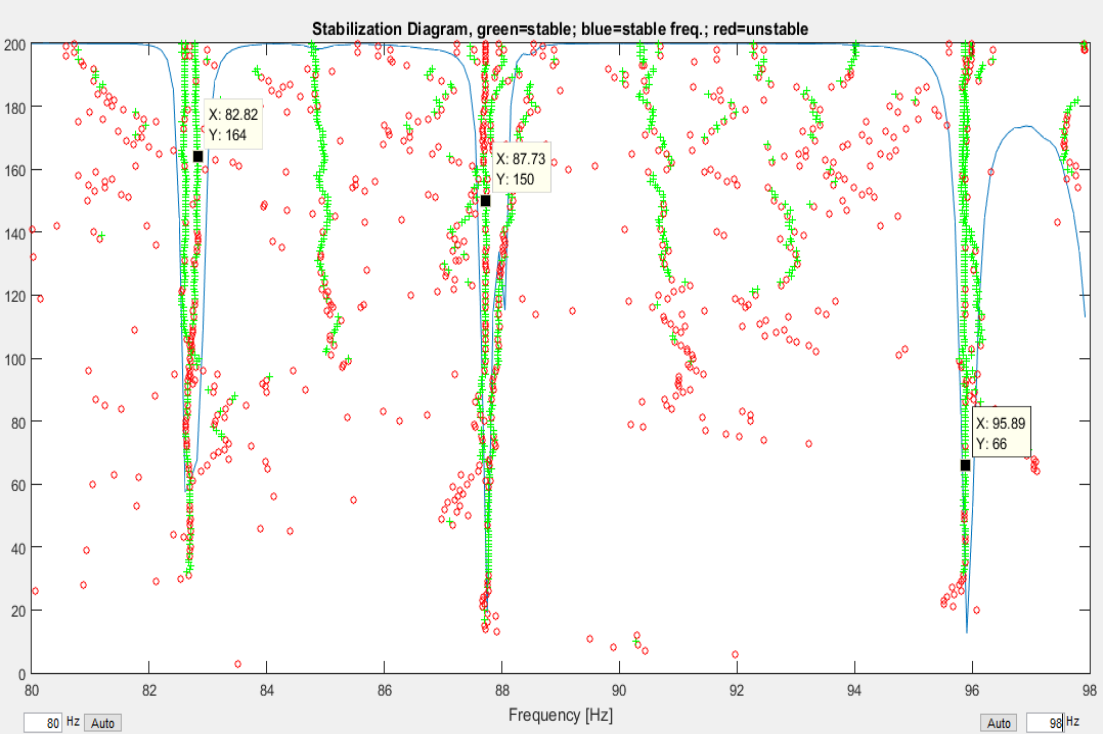

Figure 4.9: Stability diagram for frequency range 80 to 90 Hz.

Table 4.2: Natural frequency and damping ratio before and after application of VEM.

Before Application of VEM			After Application of VEM		
Mode No.	Experimental Natural frequency [Hz]	Damping ratio [%]	Mode No.	Experimental Natural frequency [Hz]	Damping ratio [%]
1	3.09	0.0442	1	3.00	0.0256
2	4.27	0.0119	2	4.04	0.0316
3	5.64	0.0110	3	4.54	0.0279
4	8.12	0.00786	4	20.73	0.00785
5	21.57	0.00272	5	22.69	0.00884
6	23.68	0.00341	6	31.23	0.00701
7	32.62	0.00366	7	33.55	0.00950
8	35.05	0.00179	8	38.28	0.00752
9	38.27	0.00246	9	43.84	0.0104
10	41.49	0.00306	10	49.49	0.00572
11	47.81	0.00167	11	54.80	0.0141
12	49.73	0.00371	12	60.54	0.0215
13	53.28	0.00366	13	66.47	0.0122
14	59.74	0.00106	14	77.29	0.0235
15	64.90	0.00124	15	88.48	0.0117
16	70.18	0.00118			
17	73.09	0.00277			
18	82.76	0.00159			
19	87.73	0.00091			
20	95.88	0.00134			

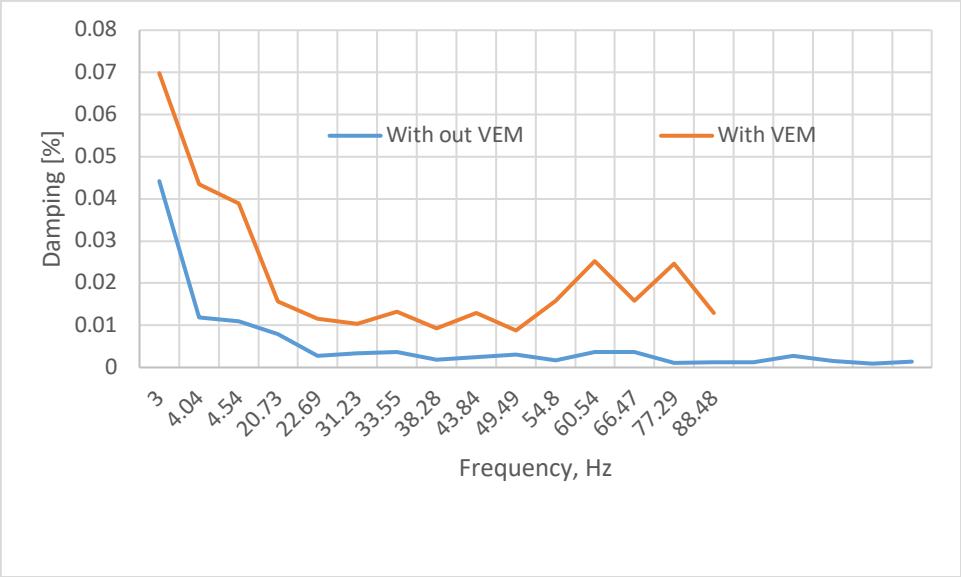

Figure 4.10: Comparison of damping before and after application of VEM on deck panel.

4.2.3 Comparison Between Experimental and Numerical Results

The comparison between experimental and numerical modal parameters are done on the basis of modal assurance criterion (MAC) values. MAC is a common tool to compare among different mode shapes of a structure. It represents the similarity between two mode shapes and its value varies from 0 to 1. Higher MAC values present better correlation between two modes of vibration than those having lower MAC values. The value of the MAC factor can be calculated from experimental eigenvector (X) and numerical eigenvector (A) from the equation:

$$MAC(X,A) = \frac{\left|\sum_{j=1}^{n}(\psi_X)_j(\psi_A)_j^*\right|^2}{\left(\sum_{j=1}^{n}(\psi_X)_j(\psi_X)_j^*\right)\left(\sum_{j=1}^{n}(\psi_A)_j(\psi_A)_j^*\right)} \cdot 100 \qquad (5.1)$$

The auto-MAC matrixes calculated before and after application of VEM are shown in Figure 4.11 and 4.12 respectively.

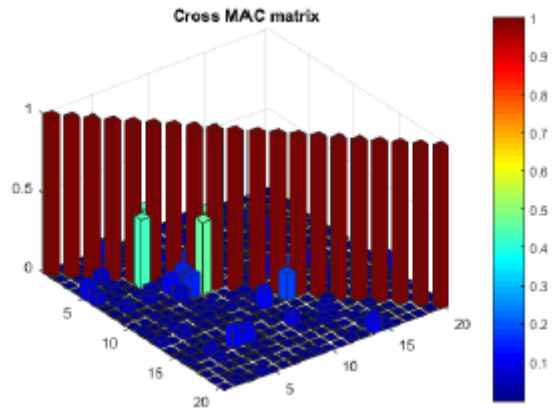

Figure 4.11: Auto-MAC matrix before application of VEM

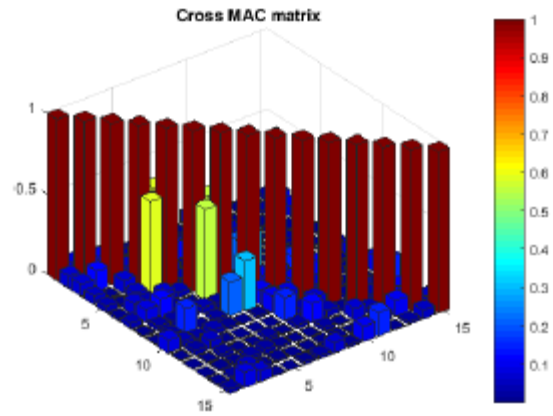

Figure 4.12: Auto-MAC matrix after application of VEM

The MAC values between the numerical modes and experimental modes are shown graphically in Figure 4.13 and 4.14. Blue color indicates lower MAC values and weak correlation between experimental and numerical modes. The other colors indicate higher MAC values and good correlation between experimental and numerical modes.

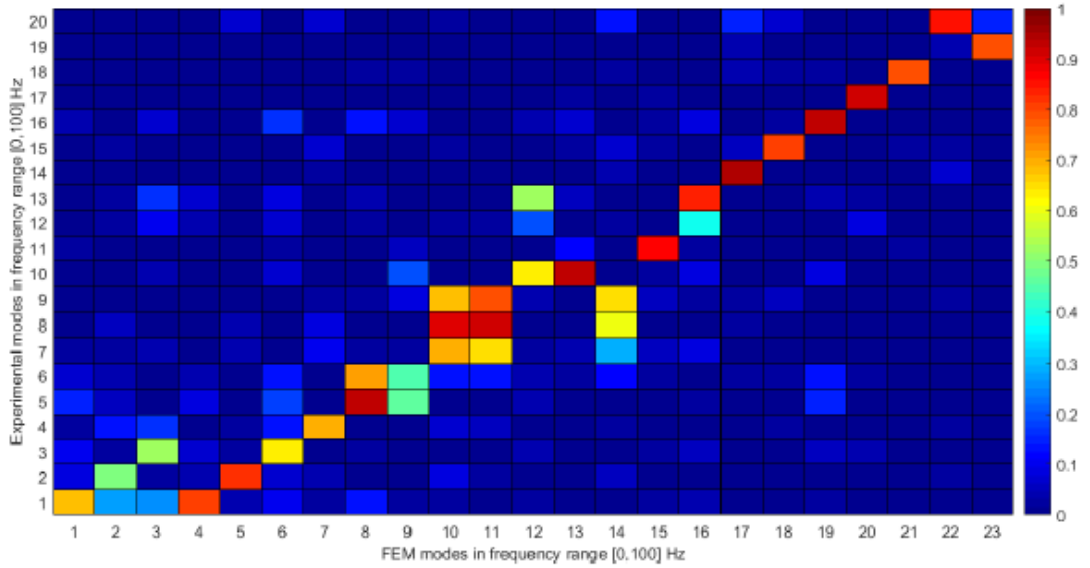

Figure 4.13: MAC matrix between experimental and numerical modes without damping

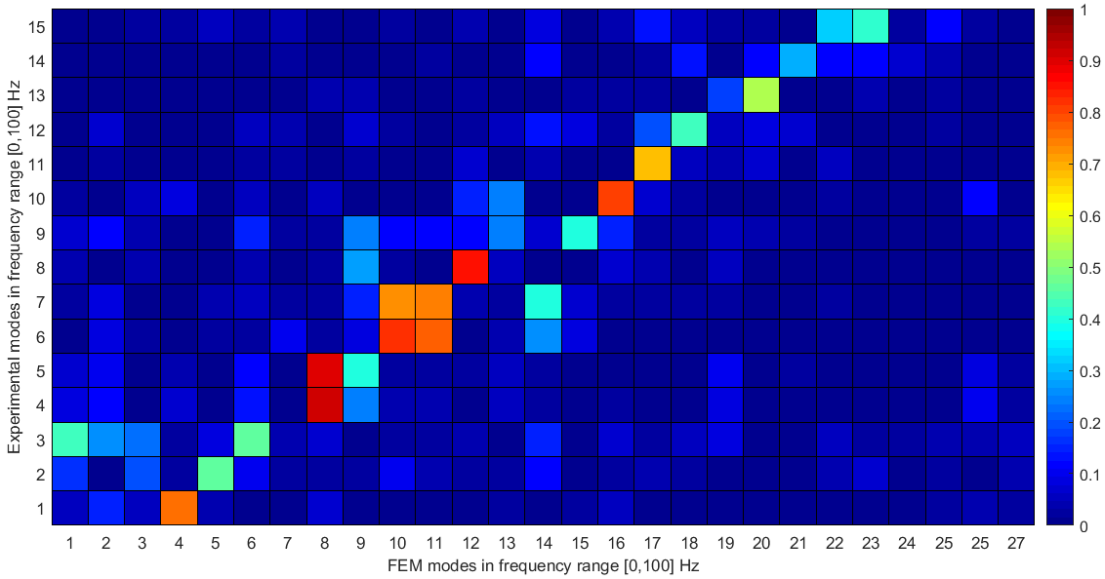

Figure 4.14: MAC matrix between experimental and numerical modes with damping

The absolute and relative difference between the experimental and numerical natural frequencies calculated before and after application of damping treatment for each pair of modes are presented in Table 4.3 and 4.4.

Table 4.3: Comparison of experimental and numerical natural frequency without VEM

Pair of modes ($\Phi_{exp,}$ Φ_{num})	f_{exp} [Hz]	$f_{num.}$ [Hz]	Δf_{abs} [Hz]	Δf_{rel} [%]	MAC
1-4	3.09	3.10	-0.01	-0.31	0.80
2-5	4.27	4.06	0.21	4.81	0.82
3-6	5.64	5.61	0.02	0.42	0.63
4-7	8.12	8.52	-0.40	-4.97	0.69
5-8	21.57	22.94	-1.38	-6.39	0.94
6-9	23.68	29.31	-5.63	-23.78	0.45
7-10	32.62	32.19	0.43	1.33	0.69
8-11	35.05	35.49	-0.43	-1.24	0.92
9-14	38.27	43.10	-4.82	-12.60	0.65
10-13	41.49	41.17	0.32	0.77	0.92
11-15	47.81	47.77	0.04	0.09	0.87
12-12	49.73	39.86	9.87	19.85	0.20
13-16	53.28	51.50	1.79	3.35	0.84
14-17	59.74	60.84	-1.09	-1.83	0.95
15-18	64.90	63.36	1.54	2.37	0.81
16-19	70.18	67.65	2.53	3.61	0.93
17-20	73.09	75.78	-2.69	-3.68	0.92
18-21	82.76	81.28	1.48	1.79	0.78
19-23	87.73	92.16	-4.43	-5.04	0.79
20-22	95.88	90.45	5.43	5.67	0.86

Table 4.4: Comparison of experimental and numerical natural frequency with VEM

Pair of modes ($\Phi_{exp,}$ Φ_{num})	f_{exp} [Hz]	$f_{num.}$ [Hz]	Δf_{abs} [Hz]	Δf_{rel} [%]	MAC
1-4	3.00	2.91	0.09	3.29	0.76
2-5	4.04	3.88	0.16	3.95	0.47
3-6	4.54	5.27	-0.73	-16.13	0.46
4-8	20.73	21.00	-0.27	-1.32	0.91
5-9	22.69	29.01	-6.31	-27.81	0.39
6-10	32.23	33.98	1.35	4.32	0.82
7-11	33.55	37.34	-0.43	-1.27	0.74
8-12	38.28	43.38	0.94	2.45	0.86
9-15	43.84	48.66	0.46	1.05	0.40
10-16	49.49	54.52	0.83	1.68	0.80
11-17	54.80	57.02	0.28	0.52	0.67
12-18	60.54	57.02	3.52	5.82	0.43
13-20	66.47	67.80	-1.33	-2.00	0.53

Figure 4.15 to 4.20 present the mode shape of mode pairs 1-4, 2-5, 3-6, 4-7, 5-8 and 10-13. The mode shape of the remaining pairs are described in Appendix-B.

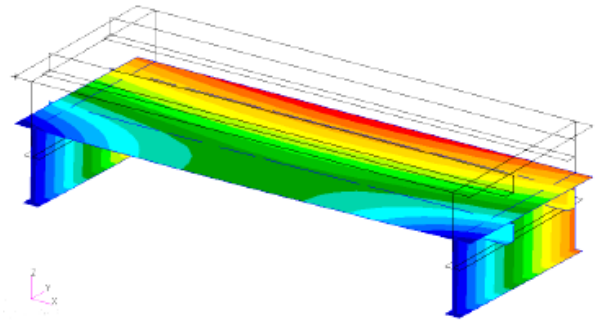

Numerical Mode No. 04,
f=3.10 Hz

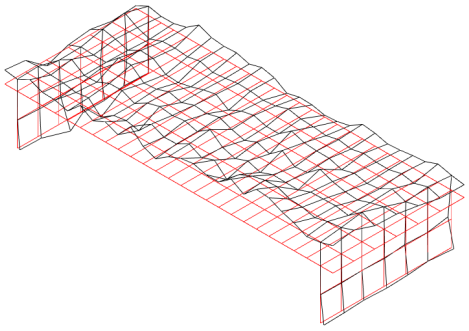

Experimental Mode No.01
f=3.09 Hz

Figure 4.15: Symmetric experimental and numerical mode shape for pair 1-4

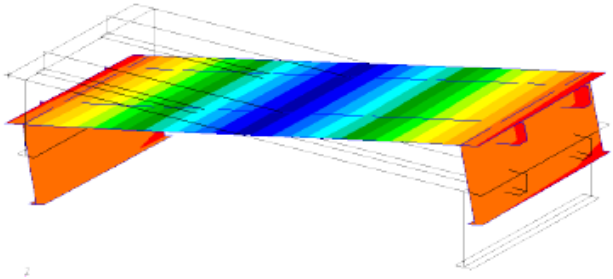

Numerical Mode No. 05
f=4.06 Hz

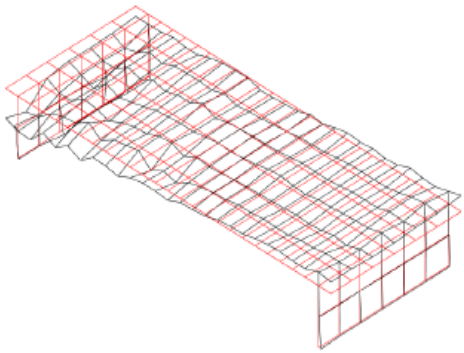

Experimental Mode No.02
f=4.27Hz

Figure 4.16: Symmetric experimental and numerical mode shape for pair 2-5

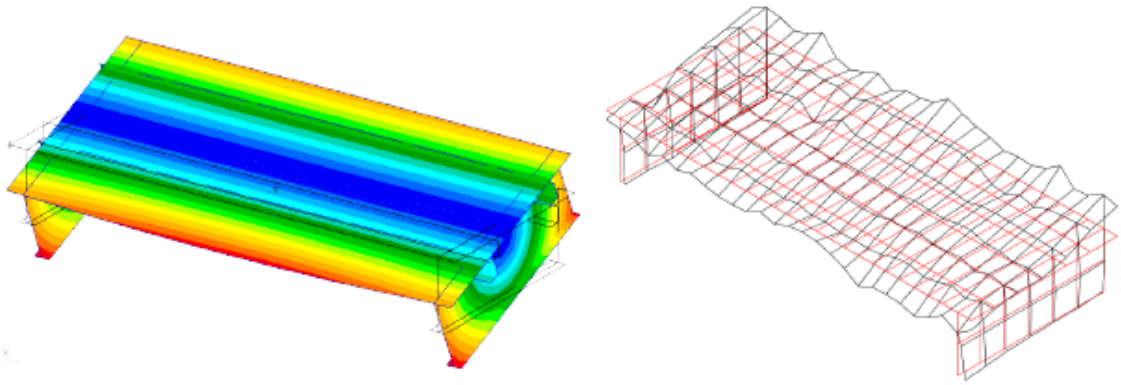

Numerical Mode No. 06
f=5.61 Hz

Experimental Mode No.03
f=5.64 Hz

Figure 4.17: Symmetric experimental and numerical mode shape for pair 3-6

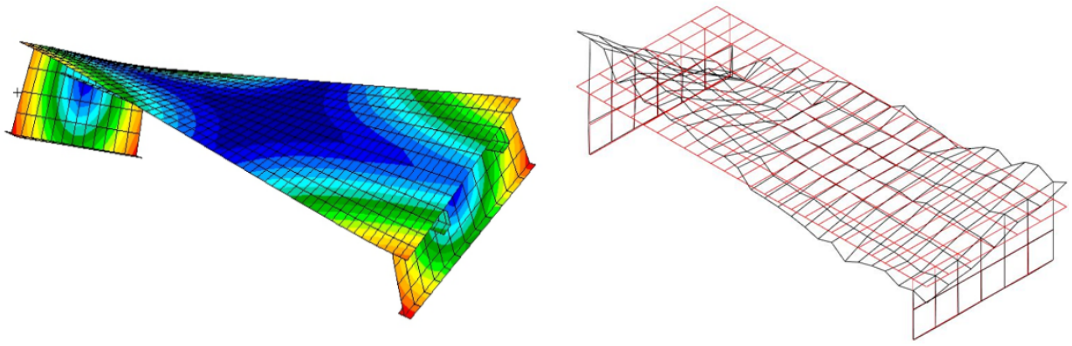

Numerical Mode No. 07
f=8.52 Hz

Experimental Mode No.04
f=8.12 Hz

Figure 4.18: Symmetric experimental and numerical mode shape for pair 4-7

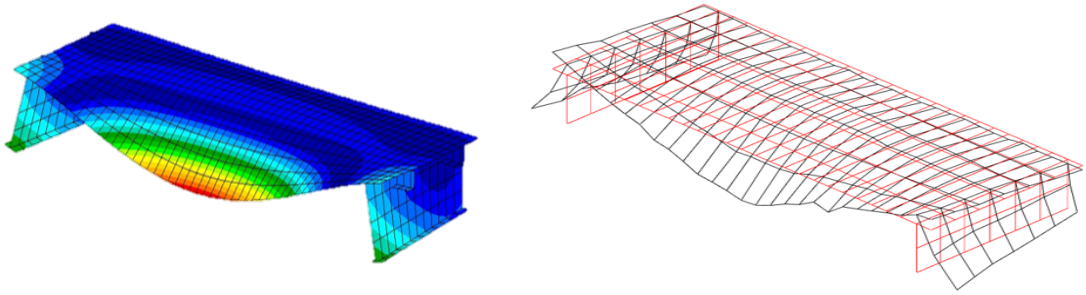

Numerical Mode No. 08
f=22.94 Hz

Experimental Mode No.05
f=21.57 Hz

Figure 4.19: Symmetric experimental and numerical mode shape for pair 5-8

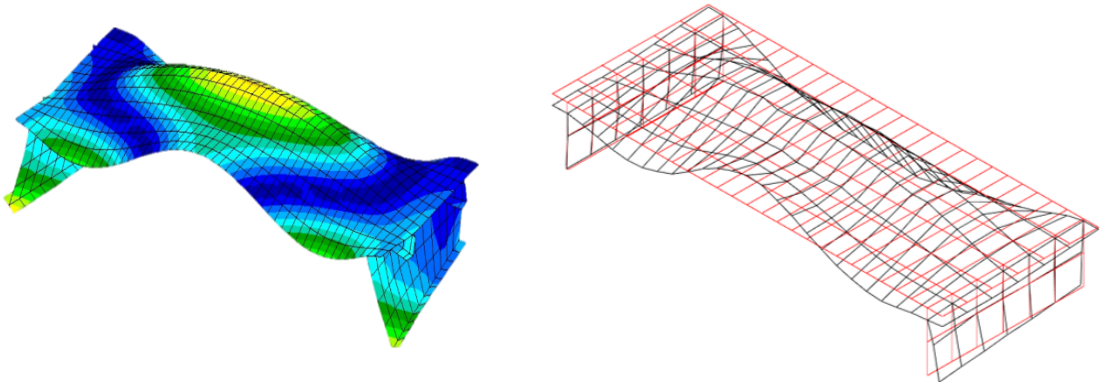

Numerical Mode No. 13
f=41.17 Hz

Experimental Mode No.10
f=41.49 Hz

Figure 4.20: Symmetric experimental and numerical mode shape for pair 10-13

4.3 Results of Experimental Statistical Energy Analysis

In this Section, the loss factor and loss parameters estimated by SEA at audio frequency range are presented. These parameters are calculated in one third octave bands. The loss factors calculated for each subsystem before application of VEM on the deck structure are tabulated in Table 4.5 and presented graphically in Figures 4.25 to 4.27.

Table 4.5: Loss factor before damping treatment.

Frequency [Hz]	η_{11}	η_{22}	η_{33}
200	3.43E-02	1.16E-03	0.00
250	0.00	8.91E-04	4.71E-03
315	0.00	6.09E-04	1.33E-03
400	1.15E-04	3.11E-04	4.12E-03
500	2.64E-03	2.36E-04	5.07E-03
630	3.32E-03	3.29E-04	3.91E-03
800	3.91E-03	6.06E-04	4.14E-03
1000	1.55E-03	4.58E-04	2.99E-03
1250	1.49E-03	5.76E-04	5.08E-03
1600	0.00	9.88E-05	2.83E-04
2000	0.00	1.13E-06	1.14E-04
2500	2.46E-04	0.00	8.01E-04
3150	2.46E-04	0.00	3.01E-04
4000	8.70E-05	0.00	1.05E-03

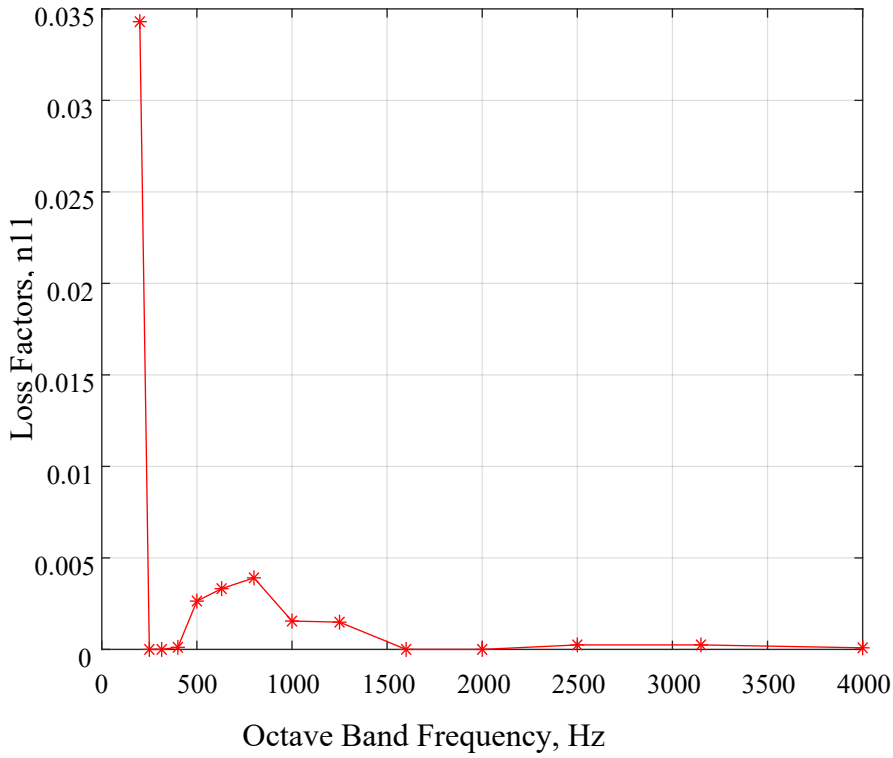

Figure 4.21: Loss factor η_{11} for subsystem 01 calculated before application of VEM

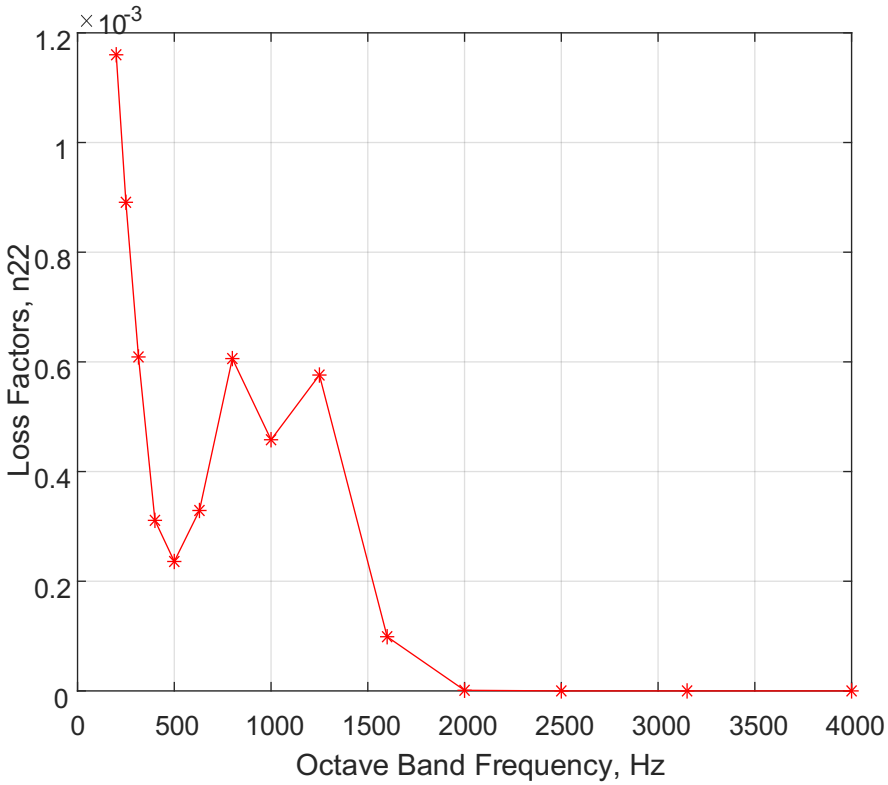

Figure 4.22: Loss factor η_{22} for subsystem 02 calculated before application of VEM

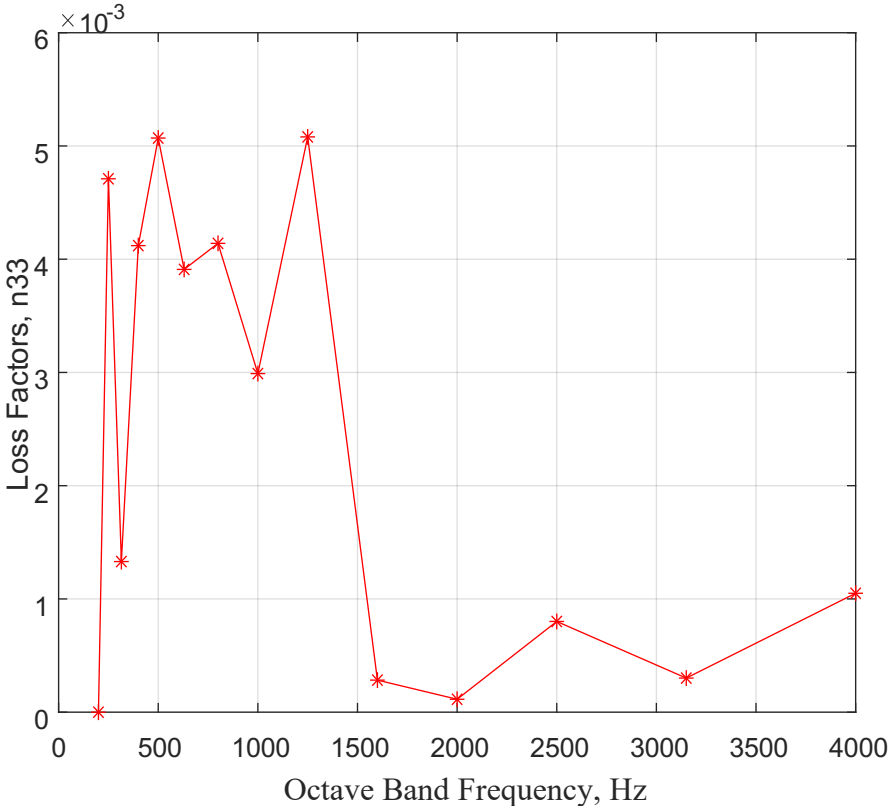

Figure 4.23: Loss factor η_{33} for subsystem 03 calculated before application of VEM

The loss factors calculated for each subsystem after application of VEM on the deck structure are tabulated in Table 4.6 and presented graphically in Figures 4.28 to 4.30.

Table 4.6: Loss factor after damping treatment.

Frequency [Hz]	η_{11}	η_{22}	η_{33}
200	1.36E-02	3.09E-02	2.08E-02
250	3.47E-02	2.47E-02	2.36E-02
315	3.70E-02	1.82E-02	2.39E-02
400	1.92E-02	1.97E-02	1.78E-02
500	1.07E-02	1.90E-02	1.93E-02
630	1.07E-02	1.51E-02	1.22E-02
800	1.48E-02	1.32E-02	1.75E-02
1000	5.40E-03	1.13E-02	6.48E-03
1250	1.03E-02	8.54E-03	1.13E-02
1600	5.89E-03	6.29E-03	6.20E-03
2000	5.35E-03	2.49E-03	9.16E-03
2500	3.68E-03	3.29E-03	6.80E-03
3150	3.25E-03	2.68E-03	4.21E-03
4000	3.87E-03	2.00E-03	4.89E-03

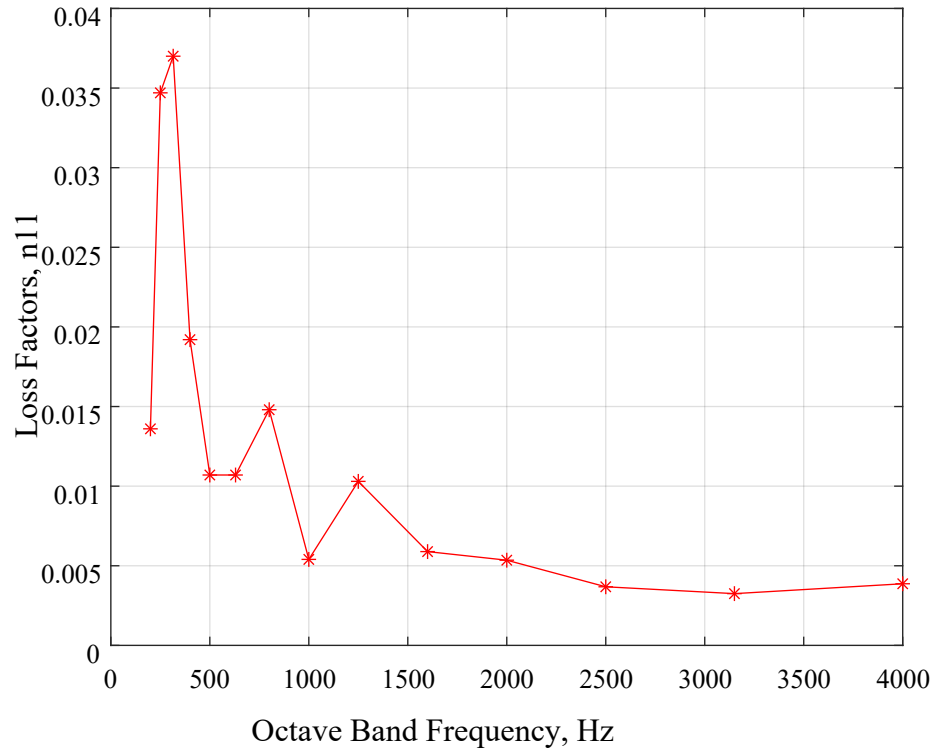

Figure 4.24: Loss factor η_{11} for subsystem 01 calculated after application of VEM

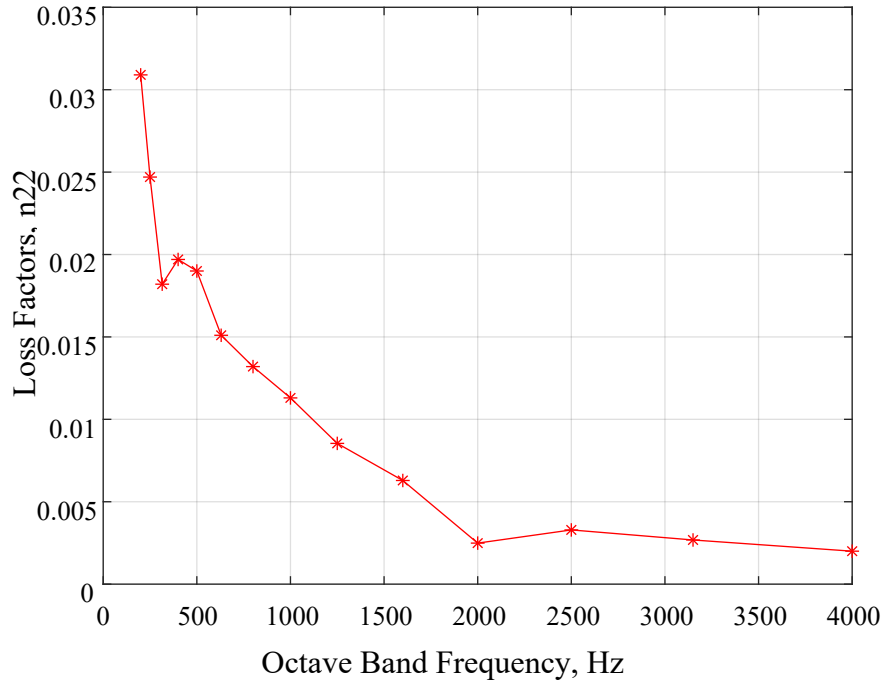

Figure 4.25: Loss factor η_{22} for subsystem 02 calculated after application of VEM

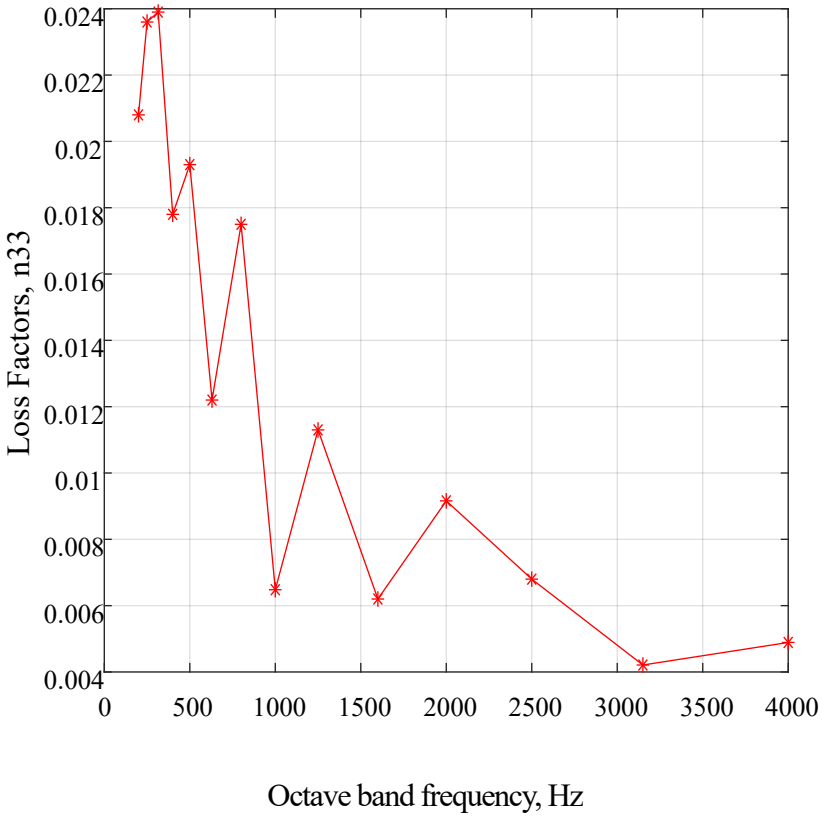

Figure 4.26: Loss factor η_{33} for subsystem 03 calculated after application of VEM

Values of Transmission loss, Insertion loss and Insertion loss base structure are presented in Table 4.7 and plotted in Figures 4.27 to 4.29 respectively.

Table 4.7: Loss parameters in one third octave band.

Frequency [Hz]	Transmission loss [dB re 10^(-9) m/s]	Insertion loss [dB re 10^(-9) m/s]	Insertion loss base structure [dB re 10^(-9) m/s]
16	0.081	8.643	8.563
20	-0.266	0.862	1.127
25	-0.067	-5.349	-5.282
31.5	-0.110	1.982	2.091
40	0.159	-7.939	-8.098
50	0.288	-3.088	-3.376
63	-2.334	-14.554	-12.220
80	-0.263	-21.567	-21.304

100	-0.373	-18.207	-17.834
125	-0.180	-14.784	-14.604
160	-0.422	-12.245	-11.823
200	-0.079	-15.398	-15.319
250	-0.680	-21.974	-21.295
315	0.119	-21.850	-21.969
400	0.089	-20.801	-20.891
500	0.272	-22.980	-23.252
630	-0.256	-23.868	-23.612
800	-0.233	-22.074	-21.842
1000	-0.500	-20.792	-20.292
1250	-0.682	-21.087	-20.405
1600	-0.660	-24.854	-24.194
2000	-0.687	-27.497	-26.810
2500	-3.209	-31.913	-28.704
3150	-2.965	-31.380	-28.416
4000	-3.833	-27.086	-23.253

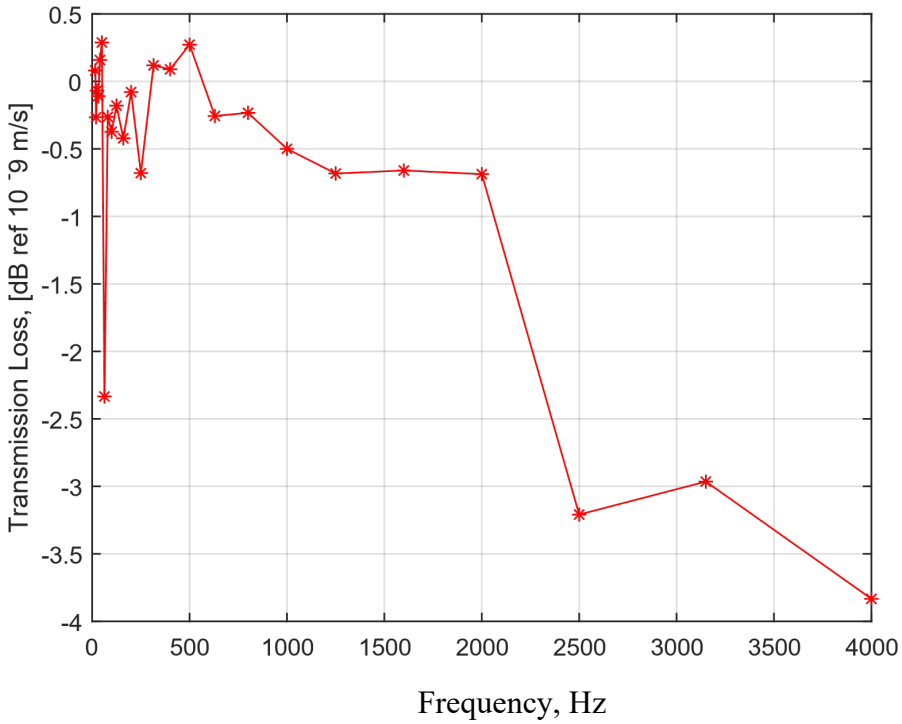

Figure 4.27: Transmission Loss

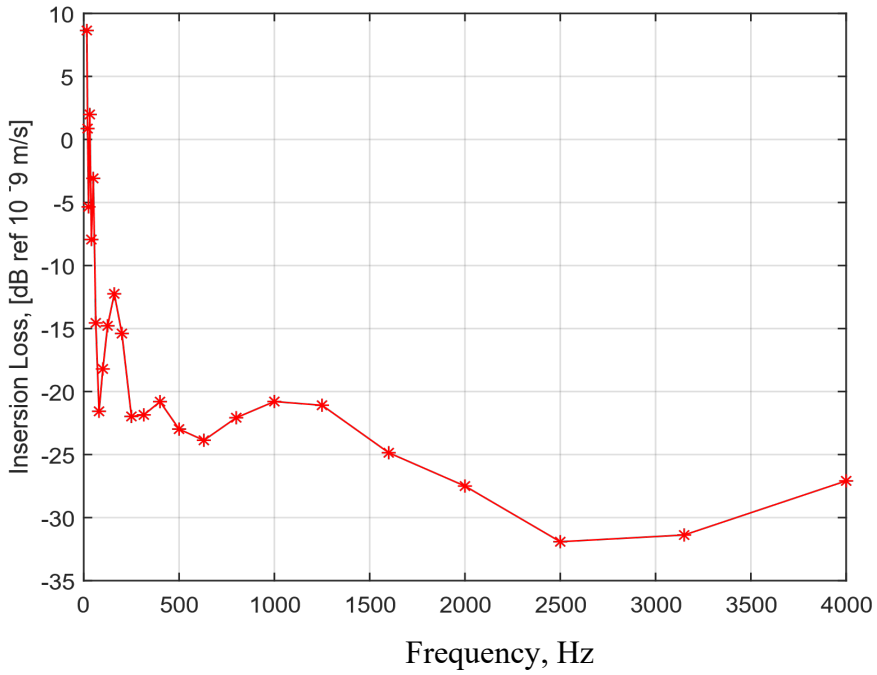

Figure 4.28: Insertion loss.

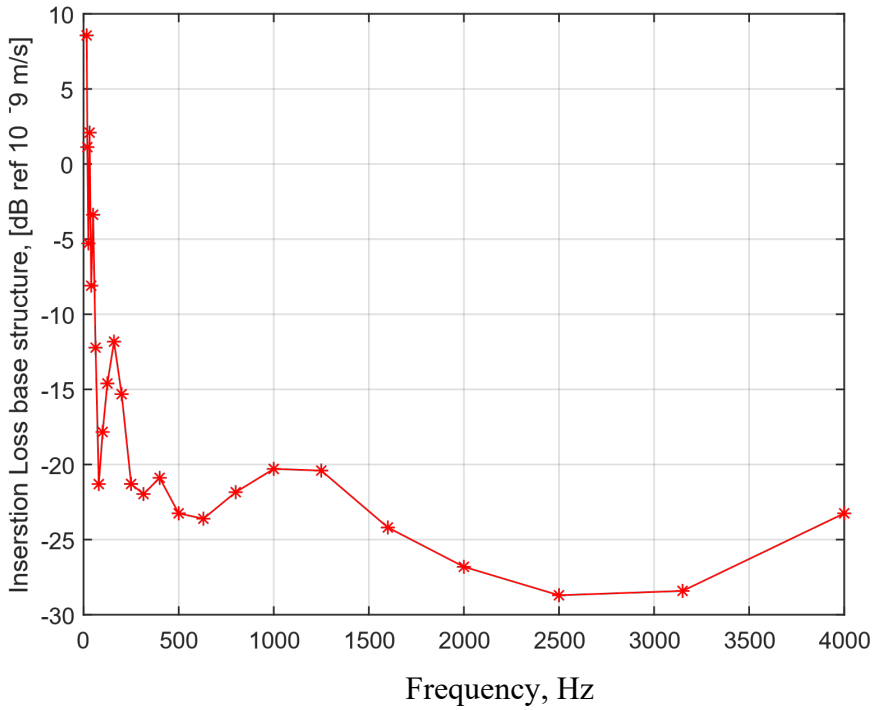

Figure 4.29: Insertion loss base structure.

Chapter 5: Discussion

From the impact test results, it is found that the CLD configuration is more effective to reduce the amplitude of the structure-borne noise and vibration as it damps all the vibrational modes of the bare beam and the overall damping appears to be higher than the free-layer damping configuration. This is seen the Figure 4.3, which shows that the damping of all vibrational modes is higher than the damping presented in Figure 4.1 and 4.2. The natural frequencies of damped beams are reduced down. The reduction level varies 4 to 10% in free-free boundary condition and 5 to 11% in cantilever boundary condition for different sets of damped beams.

With regards to effect of the boundary conditions on the assessment of the damping ratios of the VEM, Figures 4.1 and 4.2 show that the variation of the natural frequencies of the two beams is within 5.0% to 9.0%. With regard to the damping loss factors measured in two different boundary conditions, we can see from Figures 4.5 and 4.6 that there is a significant difference (12.5% to 83.64%) among the values calculated and measured. This variation is due to the uncertainty associated with the difficulty to reproduce experimentally perfect boundary conditions. In particular, the cantilever beam was obtained clamping an extremity of the tested beam by means of a flange bolted to a rigid structure (Figure 3.5). Nevertheless, bolts are not rigid connections in the audio frequency range, and this can create the shift of the natural frequencies in the audio frequency range (Figure 4.1 and 4.2). From Figure 4.5 and 4.6 it is found that the changing pattern of damping loss factor values calculated in free-free and cantilever boundary conditions are same. For this reason, it can be concluded that we need further investigation to proof that the experimental results are in agreement with the theoretical

considerations presented in Section 3.1, but the trend of the results seems to confirm the assumptions.

In the second part of this research activity, the effects of VEM to mitigate structure-borne noise and vibration when the VEM is directly applied to the ship's structures were investigated. Modal analysis was carried out to obtain natural frequencies, damping ratios and mode shapes before and after application of damping treatment to the deck panel. During the analysis FRFs measured both on the deck plate and the two transversal beams were taken into consideration. FRFs were measured in both cases, before and after application of damping layer on the deck panel. From Figure 4.8 it is observed that VEM damping treatment damps the vibrational modes of the model, as after the application of VEM their shapes become less sharp. The values of natural frequencies and damping ratios, estimated from the stabilization diagram before and after application of viscoelastic materials, are tabulated in Table 4.2. From those values it is shown that the damping increases and natural frequency reduces to lower values due to the application of the damping materials on deck panel. Particularly, this is shown for frequencies higher than 50 Hz, where the accelerances are lower and peaks are damped. This is also proved by Figure 4.10. To correlate the experimental and numerical mode shape, and validate the numerical model, the MAC matrixes between the numerical modes and the experimental modes before and after application of damping treatment are calculated and shown graphically in Figure 4.13 and 4.14 respectively. It is worth pointing out, that the numerical model of the deck panel with the damping treatment also takes into account the added mass of the non-structural material, which inertia cannot be neglected. The color of each element of the MAC

matrix represents the correspondent value of the MAC parameter. The blue color indicates low MAC values and weak correlation whereas the other colors indicate higher MAC and a stronger similarity between the experimental and numerical modes. 20 pairs of experimental and numerical modes were identified before application of damping treatment and 13 pairs of experimental and numerical modes are found after application of damping treatment on the basis of MAC values. The Comparison between the experimental and numerical frequencies and corresponding MAC values of each pair before and after application of damping treatment are tabulated in Table 4.3 and 4.4 respectively. The comparison between the experimental and numerical mode shapes are presented in Figure 4.15 to 4.20. The MAC parameter is generally higher than 0.6 denoting a good correlation between the corresponding mode shapes. Only in two cases the MAC is under this threshold, that is for the pair 6-9 and 12-12. In these two cases the identification is performed by observing the similarities of deformation shape between the experimental and numerical modes. From Table 4.4 it is found that after application of damping treatment, the MAC parameters become lower than the previous case particularly at frequencies higher than 60 Hz. This is due to the damping effect of the VEM that decreases the coherence in the acquired FRFs. Nonetheless, the MAC values are still considered acceptable and the numerical model can be considered validated.

The main objectives of the statistical energy analysis carried out in this research activity is to identify the SEA parameters. The calculation of the loss factor matrix for each third-octave band was done excluding the points 44, 110 and 160 as those points are outside the central part of the deck plate formed by two ordinary stiffeners and two T-

girders. Loss factors estimated before and after application of viscoelastic by utilizing the experimental approach are presented in the Table 4.5 and 4.6 and plotted in Figure 4.21 to 4.26. From these Figures, it is observed that the damping loss factors are also increased after application of VEM to the deck panel in the audio frequency range. The loss factor values estimated experimentally can be used in SEA simulations to understand and optimize the effect of VEM to ship structures. Estimation of the Transmission loss parameters was carried out and presented in the Table 4.7. Those values are plotted in third octave bands in Figure 4.27 to 4.29. From the loss parameter results it can be concluded that the VEM damping treatment reduces the amplitude of vibration of the radiant surface by dissipating the vibrational energy. The Transmission Loss is very low whereas the insertion loss and the insertion loss base structure achieve higher values in the frequency range of interest. This was an expected value, as VEMs are used to increase damping of ship structures, phenomenon better shown by Insertion Loss and Insertion Loss Base Structures, while the Transmission Loss is usually a more significant quantity to assess insulation characteristics of materials.

Chapter 6: Conclusions and Future Work

This research activity has been performed with an aim to develop a set of design guidelines for the optimal application of VEM at the preliminary design stage of ships structure. Analyzing the results of the research, this study can be concluded as follow:

- ❖ Damping properties of VEM depends upon the following factors:
  - Thickness
  - Types of material
  - Configuration (FLD/CLD)
- ❖ CLD is more effective than FLD in reduction of structure-borne noise and vibration as the CLD system is overdamped
- ❖ Cantilever and Free-Free boundary conditions are equivalent in characterization of VEM
- ❖ VEM is an effective damping treatment to control structure-borne noise and vibration of ships structure

  VEM treatment can reduce vibrational amplitude of radiating surface of ships deck panel both in lower and audio frequency range.

This thesis presents an application of experimental SEA to calculate damping parameters of VEM damped structure in audio frequency range. In future this work can be extended by performing numerical SEA analysis with a full-scale ship model to understand the vibrational behaviors of the whole ship structure in higher frequency range.

Bibliography:

A.S.T.M Standard, E756-05 (Reapproved 2010). Standard test method for measuring vibration-damping properties of materials. West Conshohocken, United States.

Avcar M. Free vibration analysis of beams considering different geometric characteristics and boundary conditions. system. 2014;4(2):2. Avitabile, P., 2017. Modal Testing: A Practitioner's Guide, 1 edition. Hoboken, NJ: Wiley.

Biot M, Moro L. Experimental study of a resilient mounting for marine diesel engines. In Proceedings of the IMDC 2012 Conference, Glasgow, UK 2012.

Biot M, Moro L, Vassallo PN. Prediction of the structure-borne noise due to marine diesel engines on board cruise ships. InProceedings of the 21st International Congress on Sound and Vibration 2014. ICSV21.

Brandt A. Abravibe – A Matlab toolbox for noise and vibration analysis and teaching. Department of Technology and Innovation University of Southern Denmark abra@ iti. sdu. dk May 13, 2018.

Burella G, Moro L, Colbourne B. Noise sources and hazardous noise levels on fishing vessels: The case of Newfoundland and Labrador's fleet. Ocean Engineering. 2019 Feb 1;173:116-30.

Costa PA, Calçada R, Cardoso AS. Ballast mats for the reduction of railway traffic vibrations. Numerical study. Soil Dynamics and Earthquake Engineering. 2012 Nov 1;42:137-50.

Crocker MJ, editor. Handbook of noise and vibration control. John Wiley & Sons; 2007 Oct 5.

De Silva CW. Vibration damping, control, and design. CRC Press; 2007 Apr 5.

De Silva CW. Vibration: fundamentals and practice. CRC press; 2006 Sep 14.

De Langhe, K., 1996. High frequency vibrations: contributions to experimental and computational SEA parameter identification techniques. Doctoral dissertation of Katholieke Universiteit Leuven, Celestijnenlaan 300B-B 3001 Heverlee(Leuven), Belgium.

De Fenza A. Experimental and numerical estimation of damping in composite plates with embedded viscoelastic treatments (Doctoral dissertation, PhD Thesis, Department of Aerospace Engineering, University of Naples–Federico II, Italy).

Daley S, Johnson FA, Pearson JB, Dixon R. Active vibration control for marine applications. Control Engineering Practice. 2004 Apr 1;12(4):465-74.

Fedeli, N. Experimental characterization and numerical simulations of visco-elastic materials for marine application. Master dissertation of Universita Degli Studi Di Trieste, Italy.

Fan R, Meng G, Yang J, He C. Experimental study of the effect of viscoelastic damping materials on noise and vibration reduction within railway vehicles. Journal of Sound and Vibration. 2009 Jan 9;319(1-2):58-76.

Fragasso J, Moro L, Vassallo PM, Biot M, Badino A. Experimental characterization of viscoelastic materials for marine applications. In Progress in the Analysis and Design of Marine Structures 2017 Apr 28 (pp. 87-96). CRC Press.

Fragasso J, Moro L, Lye LM, Quinton BW. Characterization of resilient mounts for marine diesel engines: Prediction of static response via nonlinear analysis and response surface methodology. Ocean Engineering. 2019 Jan 1;171: 14-24.

Ferrari, A., Rizzuto, E., March 2007. Measuring of damping properties of viscoelastic materials for marine applications. In advancement in Marine Structures – Proceedings of the 1st International Conference on Marine Structure (MARSTRUCT – 2007), Glasgow, UK, 12-14.

Ferrari, A. and Rizzuto, E., September 2005. Modal Behavior of a full-scale deck panel with anti-noise treatments. Maritime Transportation and Exploration of Ocean and Coastal Resources: Proceeding of the 11th International Congress of the International Maritime Association of the Mediterranean, Lisbon, Portugal, 26-30.

Flint J. A review of theories on constrained layer damping and some verification measurements on shim material. SAE Technical Paper; 2003 Oct 19.

Hujare PP, Sahasrabudhe AD. Effect of Thickness of Damping Material on Vibration Control of Structural Vibration in Constrained Layer Damping Treatment. InApplied Mechanics and Materials 2014 (Vol. 592, pp. 2031-2035). Trans Tech Publications.

Irvine, T., 2011. Bending frequencies of beams, rods and pipes. Vibration data, Revision P.

Jones DI. Handbook of viscoelastic vibration damping. John Wiley & Sons; 2001 Aug 15.

Kandasamy R, Cui F, Townsend N, Foo CC, Guo J, Shenoi A, Xiong Y. A review of vibration control methods for marine offshore structures. Ocean Engineering. 2016 Nov 15;127:279-97.

Kalivoda M, Danneskiold-Samsøe U, Krüger F, Barsikow B. EURailNoise: a study of European priorities and strategies for railway noise abatement. Journal of Sound and Vibration. 2003 Oct 23;267(3):387-96.

Lieven N. A. J., Ewins D. J., McConnell, K. G., Jan. 2001. Modal testing. Philos. Trans. R. Soc. Lond. Ser. Math. Phys. Eng. Sci., vol. 359, no. 1778, pp. 11–28.

Lieven, N. A. J., Ewins, D. J., Lieven, N.A.J., Ewins, D. J., Jan. 2001. The context of experimental modal analysis. Philos. Trans. R. Soc. Lond. Ser. Math. Phys. Eng. Sci., vol. 359, no. 1778, pp. 5–10.

Monk-Steel AD, Thompson DJ, De Beer FG, Janssens MH. An investigation into the influence of longitudinal creepage on railway squeal noise due to lateral creepage. Journal of Sound and Vibration. 2006 Jun 13;293(3-5):766-76.

Martinez-Agirre M, Elejabarrieta MJ. Dynamic characterization of high damping viscoelastic materials from vibration test data. Journal of sound and vibration. 2011 Aug 1;330(16):3930-43.

Moro.L, Brocco. E, Badino. A, Vassallo. P.N.M, Clericuzio. A, Biot. M., September, 2016. Design procedure for the development of new floating floors to improve comfort on ships. Proceedings of PRADS 2016, 4-8. Copenghagen, Denmark.

Moro L, Brocco E, Vassallo PM, Biot M, Le Sourne H. Numerical simulation of the dynamic behaviour of resilient mounts for marine diesel engines. In5th International Conference on Marine Structures (MARSTRUCT 2015) 2015 Mar 2 (pp. 149-157). CRC Press, Taylor and Francis Group.

McConnell, K. G.,2001. Modal Testing. Philos. Trans. Math. Phys. Eng. Sci., vol. 359, no. 1778, pp. 11–28.

Nakra BC. Vibration control in machines and structures using viscoelastic damping. Journal of sound and vibration. 1998 Apr 2;211(3):449-66.

Swinbanks MA. The active control of noise and vibration and some applications in industry. Proceedings of the Institution of Mechanical Engineers, Part A: Power and Process Engineering. 1984 Nov;198(4):281-8.

Schulte-Werning B, Beier M, Degen KG, Stiebel D. Research on noise and vibration reduction at DB to improve the environmental friendliness of railway traffic. Journal of sound and vibration. 2006 Jun 13;293(3-5):1058-69.

Schomer PD, Neathammer RD. The role of helicopter noise-induced vibration and rattle in human response. The Journal of the Acoustical Society of America. 1987 Apr;81(4):966-76.

Syed RU, Sabir MI, Wei J, Shi DY. Effect of viscoelastic material thickness of damping treatment behavior on gearbox. Research Journal of Applied Sciences, Engineering and Technology. 2012 Sep 1;4(17):3130-6.

Sheng X, Jones CJ, Thompson DJ. Prediction of ground vibration from trains using the wavenumber finite and boundary element methods. Journal of Sound and Vibration. 2006 Jun 13;293(3-5):575-86.

Thompson DJ, Jones CJ, Waters TP, Farrington D. A tuned damping device for reducing noise from railway track. Applied acoustics. 2007 Jan 1;68(1):43-57.

The International Labour Organization and the safety and Health of Fishers, A report of ILO to improve occupational safety and health based on papers presented at IFISH-3, India, 2006.

Vergassola G, Boote D, Tonelli A. On the damping loss factor of viscoelastic materials for naval applications. Ships and Offshore Structures. 2018 Jul 4;13(5):466-75.

Wills AG, Bates D, Fleming AJ, Ninness B, Moheimani SR. Model predictive control applied to constraint handling in active noise and vibration control. IEEE Transactions on Control Systems Technology. 2008 Jan;16(1):3-12.

Zytoon MA. Occupational injuries and health problems in the Egyptian Mediterranean fisheries. Safety science. 2012 Jan 1;50(1):113-22.

Appendices

Appendix-A: Subsidiary Results of Impact Test

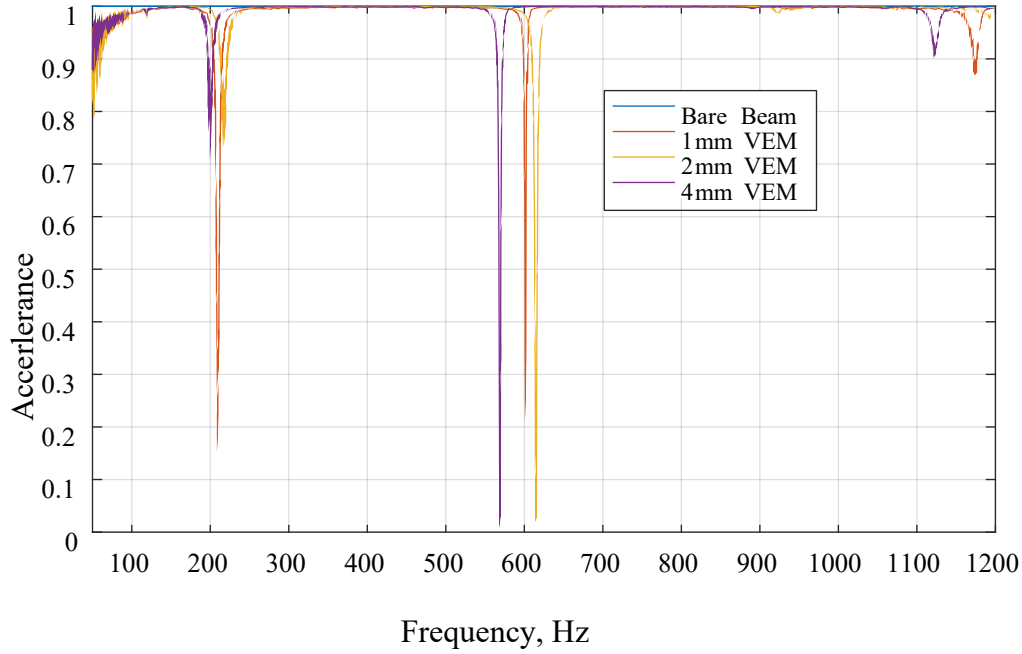

Figure A.1: Coherence for beam 1to 4 at cantilever boundary conditions.

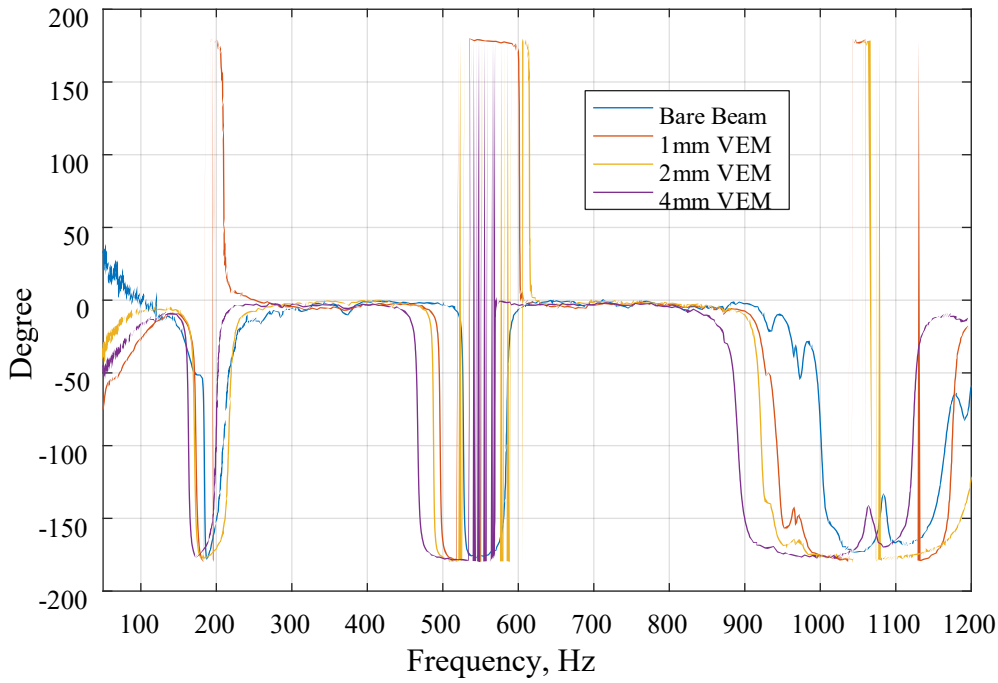

Figure A.2: Phase for beams 1 to 4 at cantilever boundary condition.

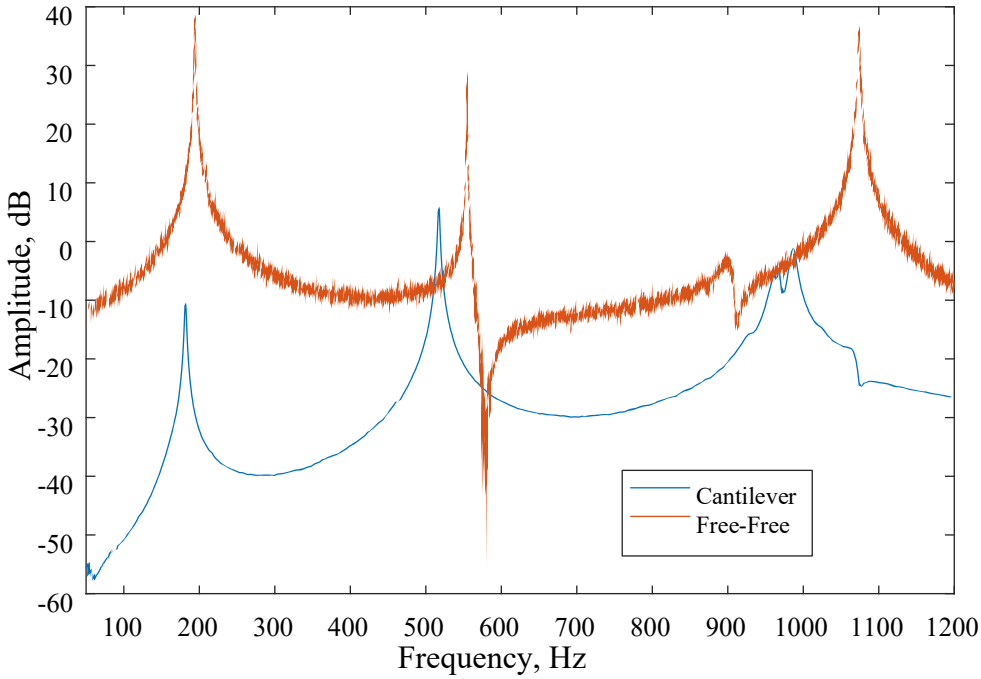

Figure A.3: FRF of bare beam at free-free and cantilever boundary conditions.

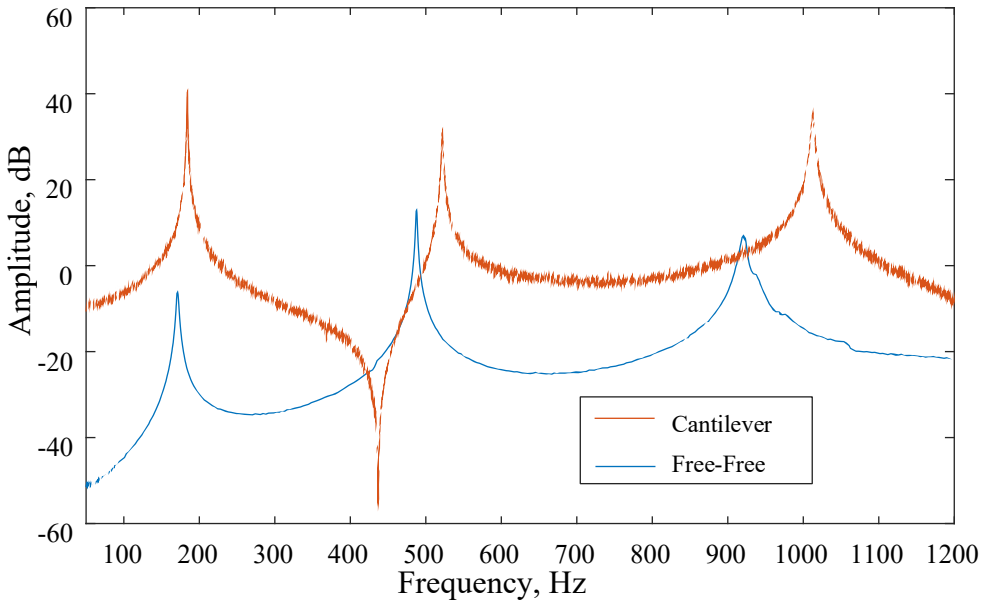

Figure A.4: FRF of beam-3 at free-free and cantilever boundary conditions.

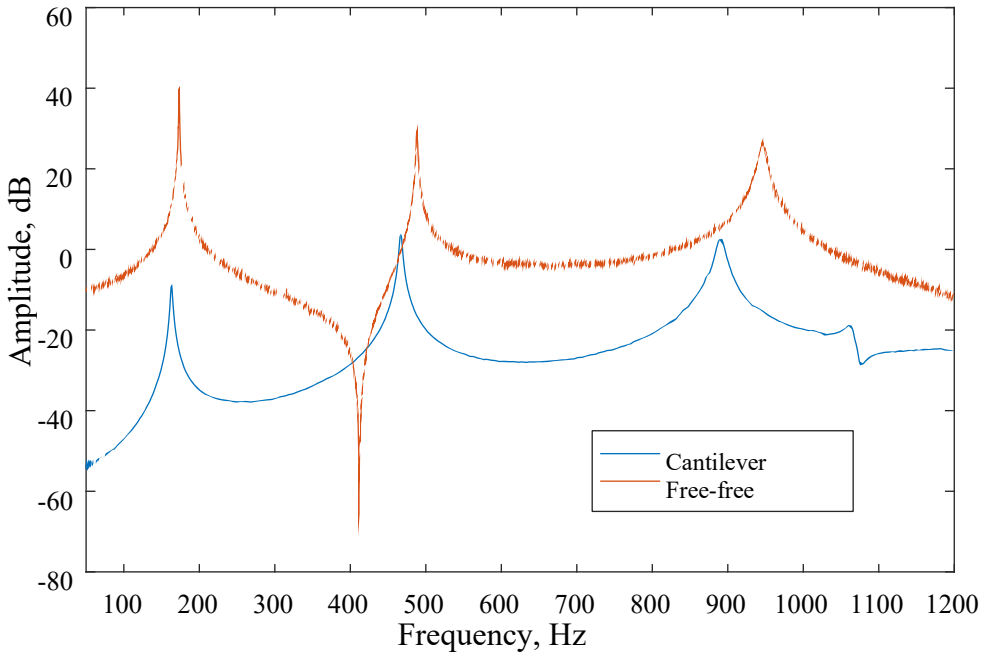

Figure A.5: FRF of beam-4 at free-free and cantilever boundary conditions.

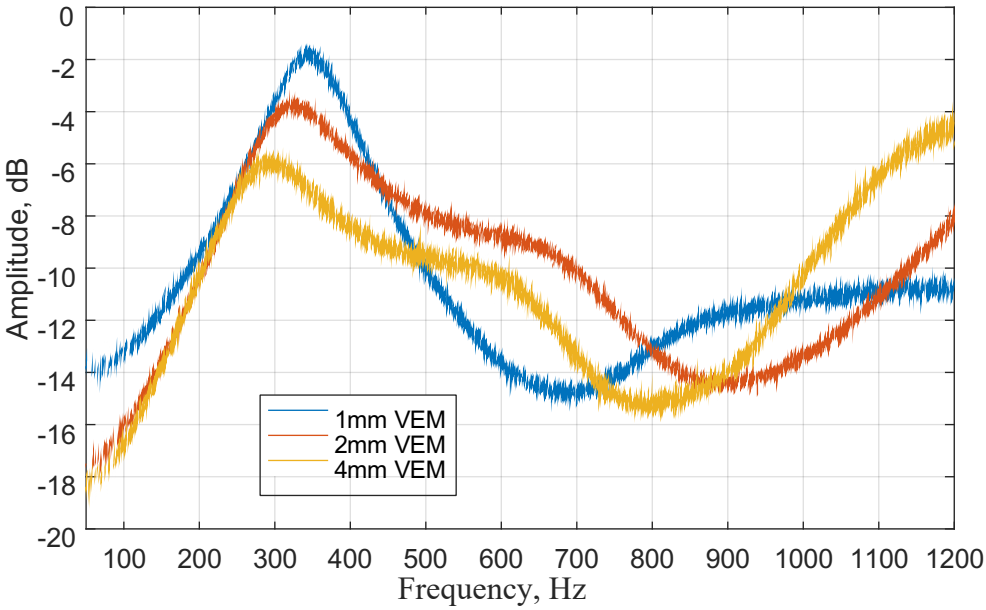

Figure A.6: All FRF at free-free boundary conditions at CLD

Appendix-B: Subsidiary Results of Modal Analysis

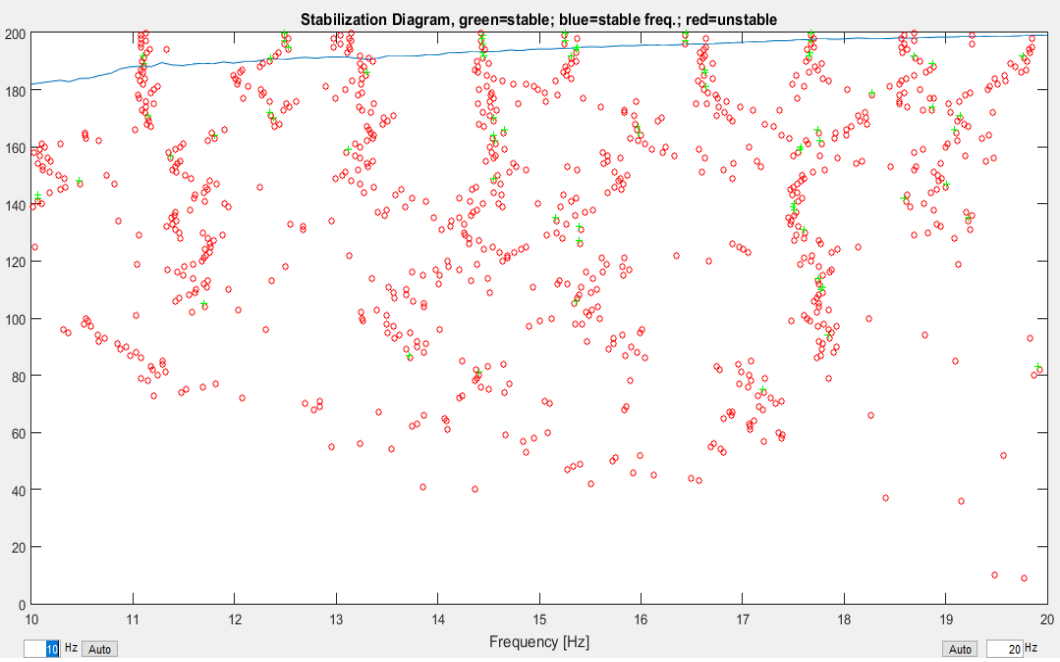

Figure B.1: Stability diagram 10-20 Hz

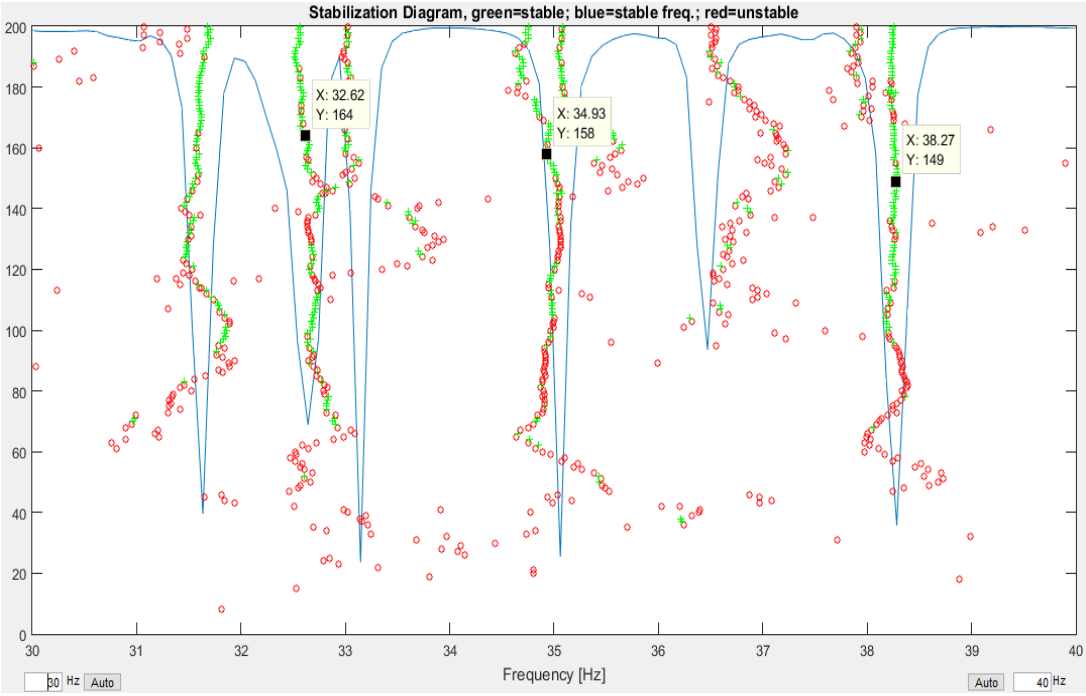

Figure B.2: Stability diagram 30-40 Hz

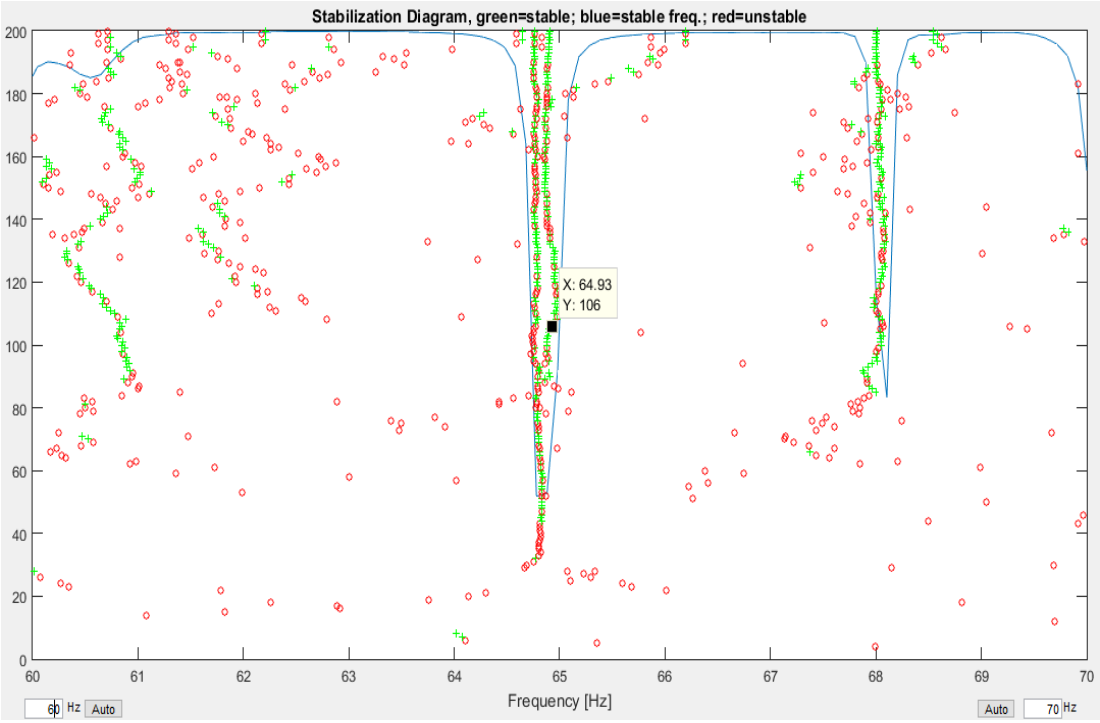

Figure B.3: Stability diagram 60-70 Hz

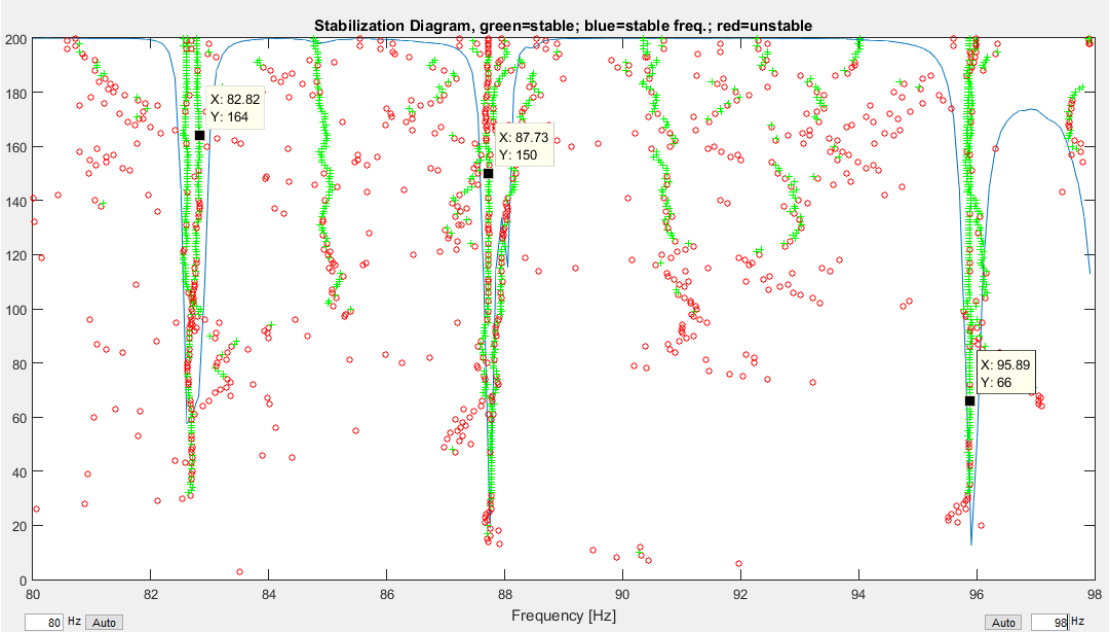

Figure B.4: Stability diagram 80-90 Hz

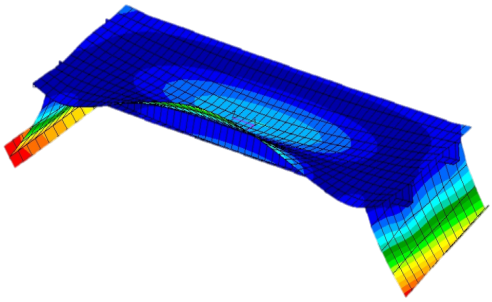

Numerical Mode No. 09

$f = 32.43$ Hz

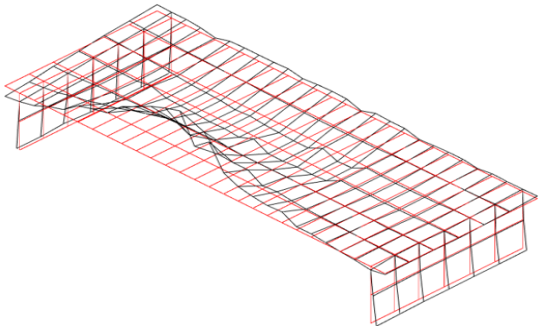

Experimental Mode No.06

$f = 23.64$ Hz

Figure B.5: Symmetric experimental and numerical mode shape for pair 6-9

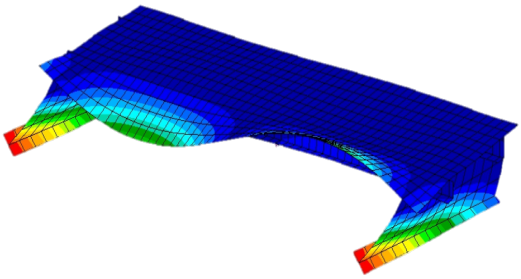

Numerical Mode No. 10

$f = 35.62$ Hz

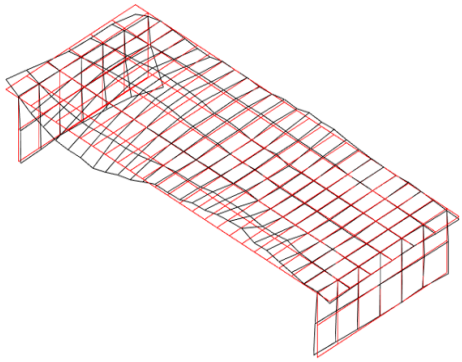

Experimental Mode No.07

$f = 32.62$ Hz

Figure B.6: Symmetric experimental and numerical mode shape for pair 7-10

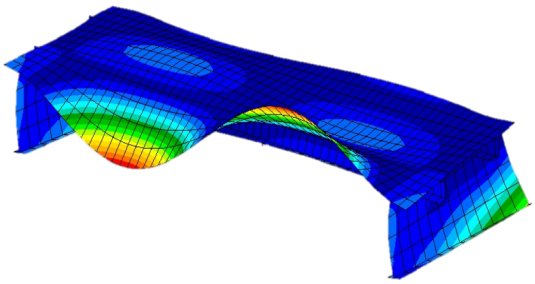

Numerical Mode No. 11

$f = 41.56$ Hz

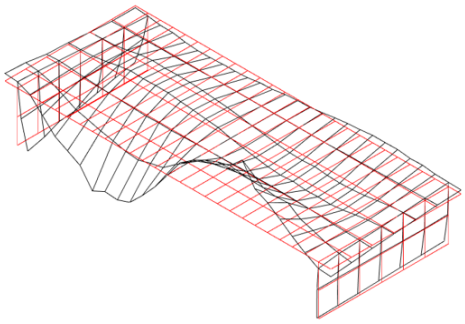

Experimental Mode No.08

$f = 34.93$ Hz

Figure B.7: Symmetric experimental and numerical mode shape for pair 8-11

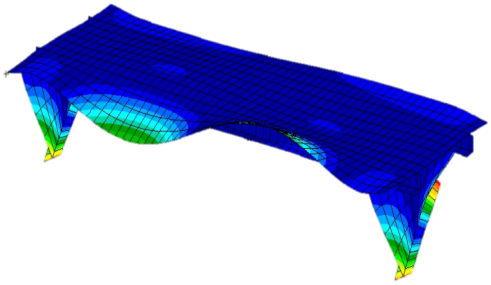

Numerical Mode No. 14

$f = 46.69$ Hz

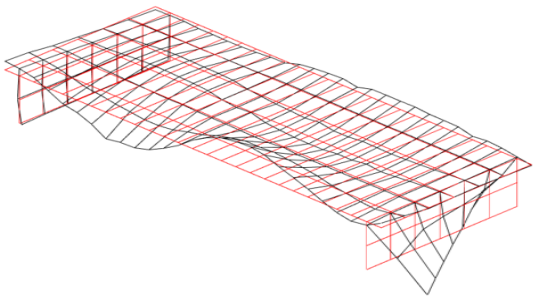

Experimental Mode No.09

$f = 38.27$ Hz

Figure B.8: Symmetric experimental and numerical mode shape for pair 9-14

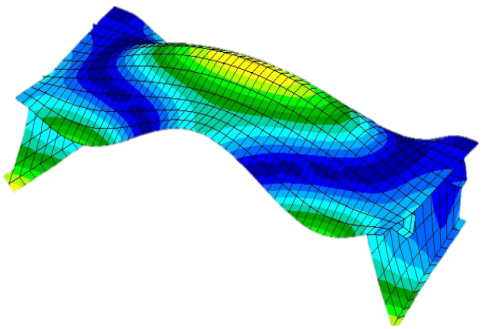

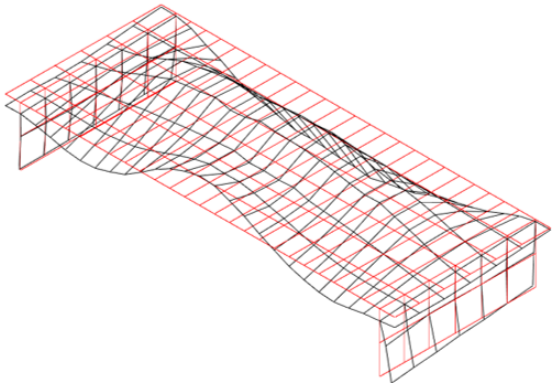

Numerical Mode No. 13

$f = 46.22$ Hz

Experimental Mode No.10

$f = 41.49$ Hz

Figure B.9: Symmetric experimental and numerical mode shape for pair 10-13

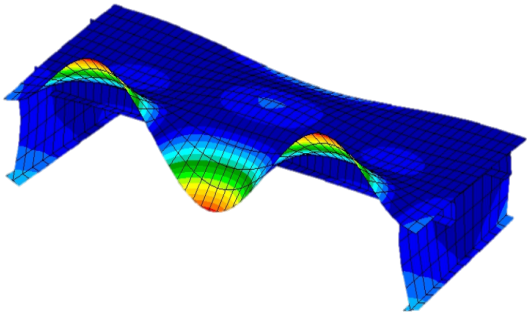

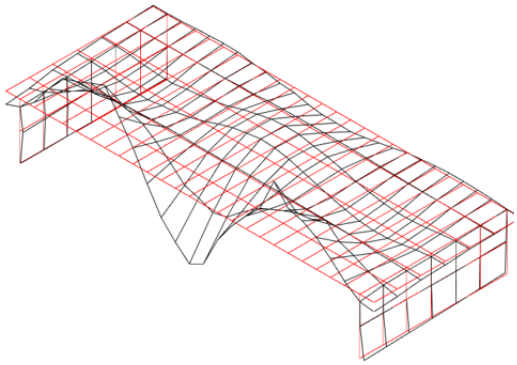

Numerical Mode No. 16

$f = 60.35$ Hz

Experimental Mode No.11

$f = 47.98$ Hz

Figure B.10: Symmetric experimental and numerical mode shape for pair 11-16

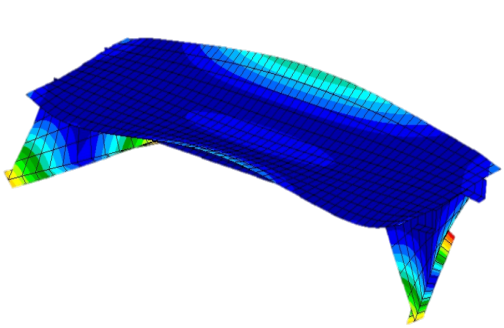

Numerical Mode No. 12

$f = 42.89$ Hz

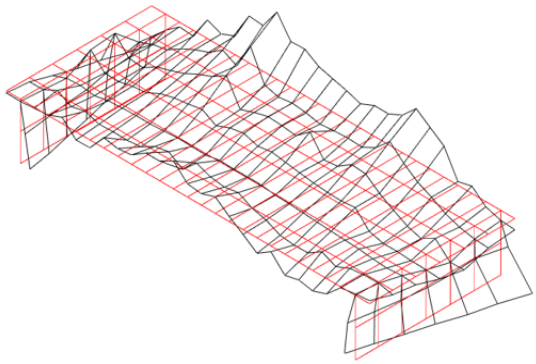

Experimental Mode No.12

$f = 50.03$ Hz

Figure B.11: Symmetric experimental and numerical mode shape for pair 4-7

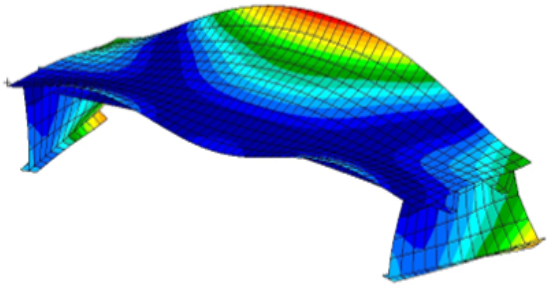

Numerical Mode No. 15

$f = 54.69$ Hz

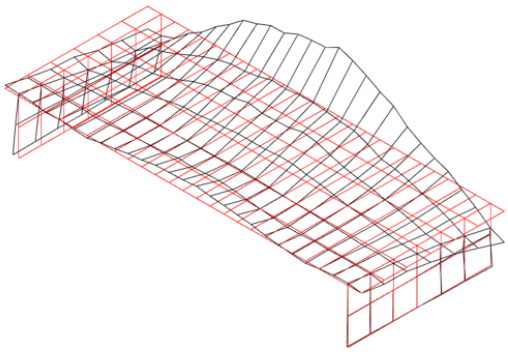

Experimental Mode No.13

$f = 53.31$ Hz

Figure B.12: Symmetric experimental and numerical mode shape for pair 13-15

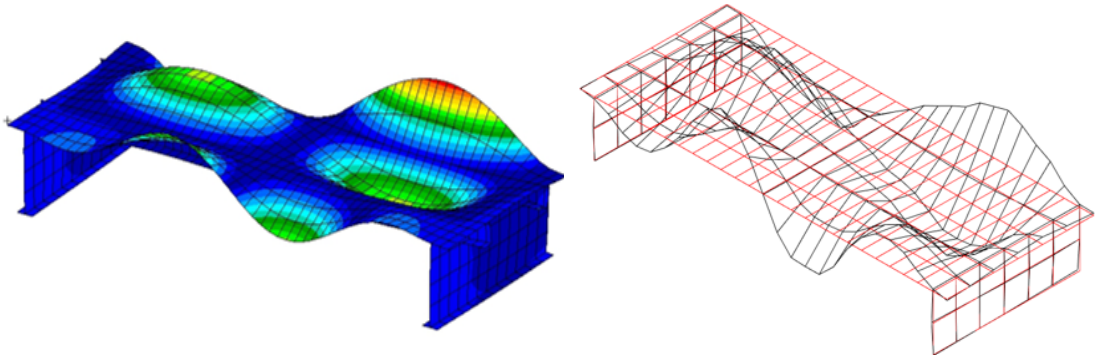

Numerical Mode No. 17 Experimental Mode No.14

$f = 74.71$ Hz $f = 59.72$ Hz

Figure B.13: Symmetric experimental and numerical mode shape for pair 14-17

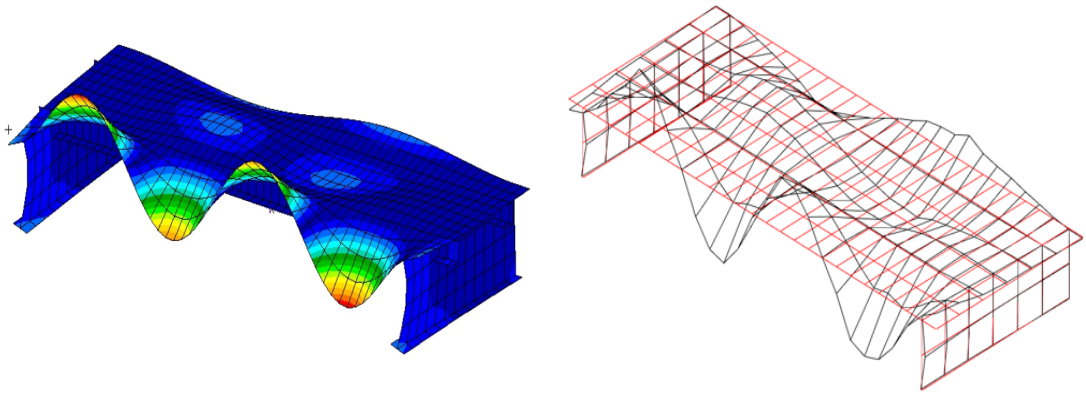

Numerical Mode No. 18 Experimental Mode No.15

$f = 80.40$ Hz $f = 64.93$ Hz

Figure B.14: Symmetric experimental and numerical mode shape for pair 15-18

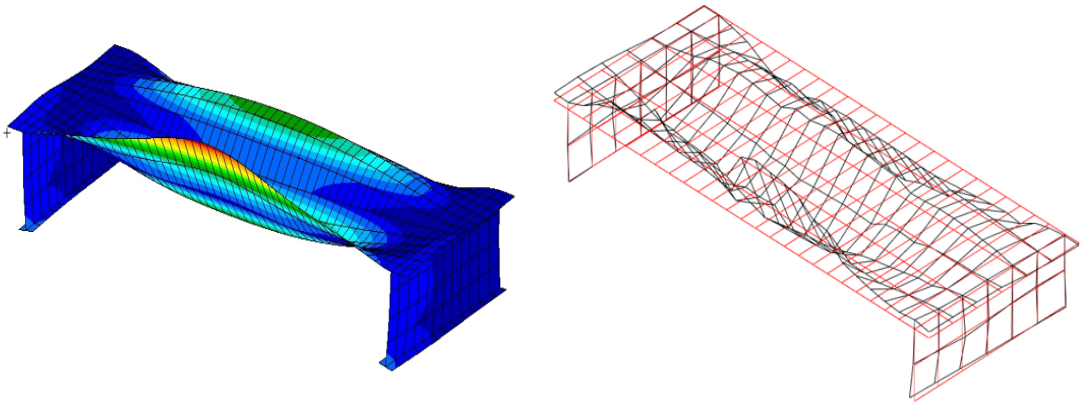

Numerical Mode No. 19

$f = 81.24$ Hz

Experimental Mode No.16

$f = 70.17$ Hz

Figure B.15: Symmetric experimental and numerical mode shape for pair 16-19

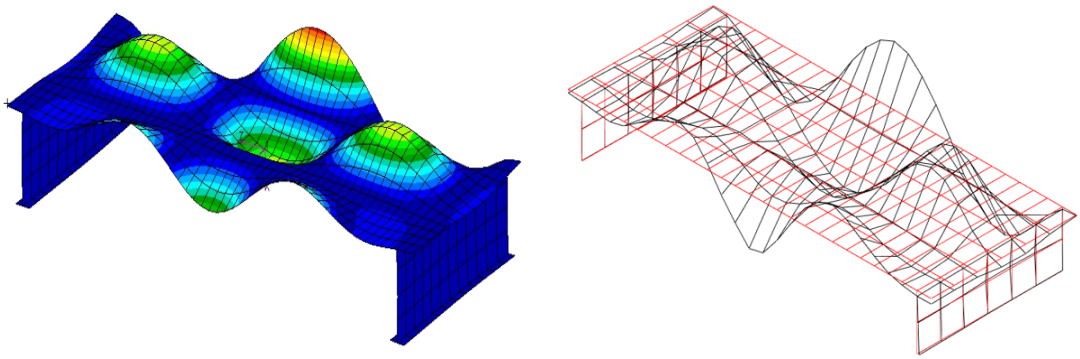

Numerical Mode No. 20

$f = 98.70$ Hz

Experimental Mode No.17

$f = 73.10$ Hz

Figure B.16: Symmetric experimental and numerical mode shape for pair 17-20

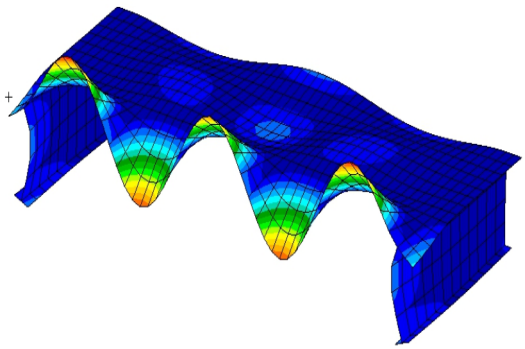

Numerical Mode No. 21

$f = 103.74$ Hz

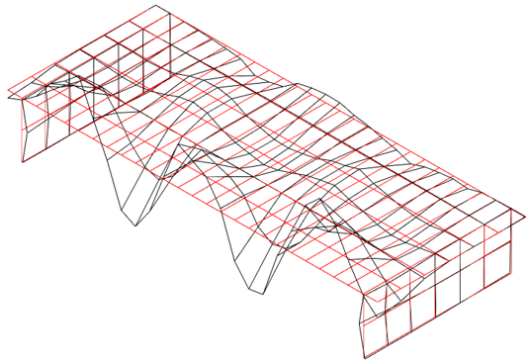

Experimental Mode No.18

$f = 82.82$ Hz

Figure B.17: Symmetric experimental and numerical mode shape for pair 18-21

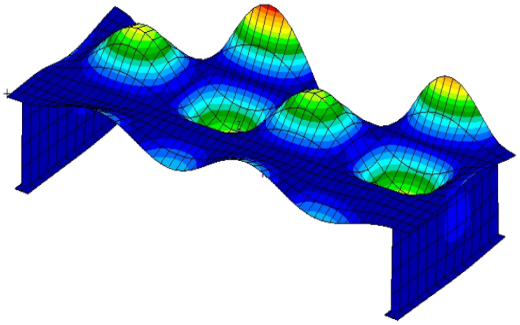

Numerical Mode No. 23

$f = 121.32$ Hz

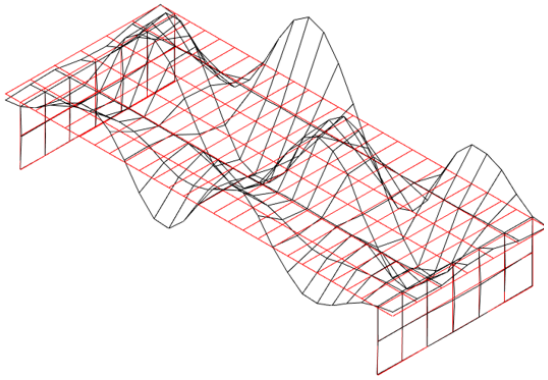

Experimental Mode No.19

$f = 87.73$ Hz

Figure B.18: Symmetric experimental and numerical mode shape for pair 19-23

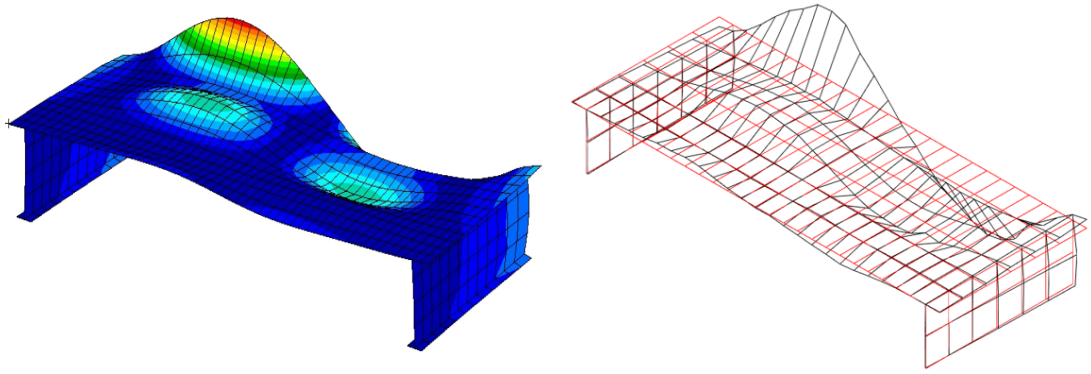

Numerical Mode No. 22

f = *111.14* Hz

Experimental Mode No.20

f = *95.89* Hz

Figure B.19: Symmetric experimental and numerical mode shape for pair 19-23

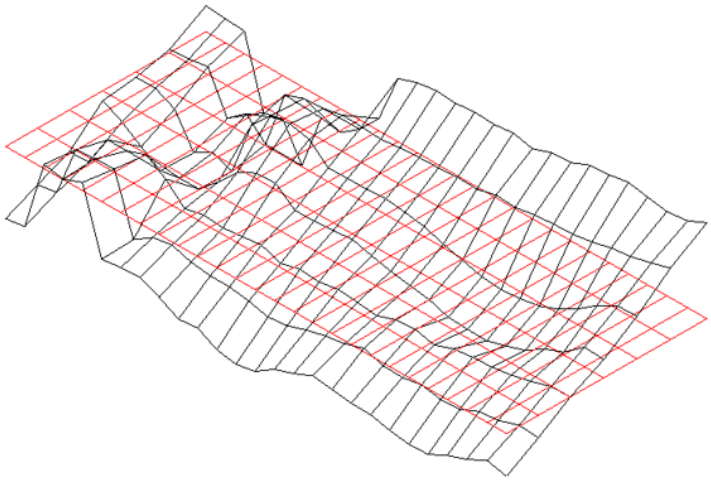

Figure B.20: Mode shape of the deck plate after damping treatment (*f* = 4.551 Hz)

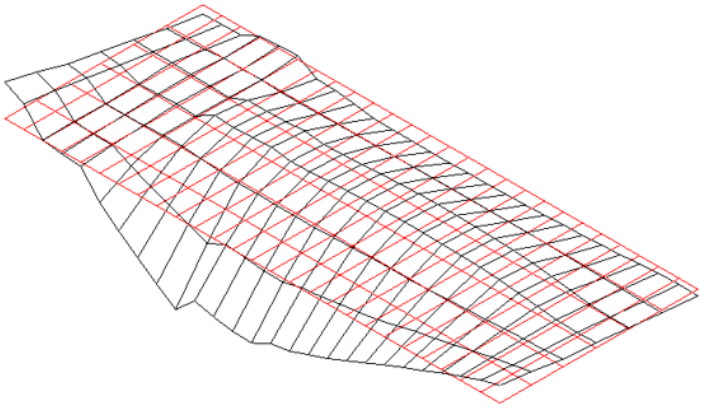

Figure B.21: Mode shape of the deck plate after damping treatment (f = 20.67 Hz)

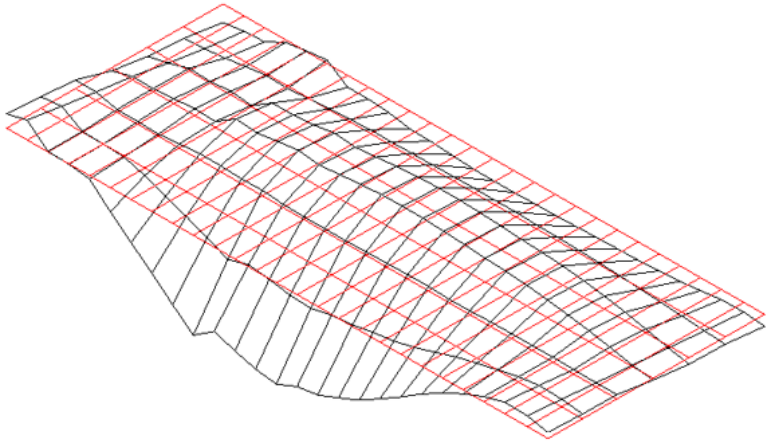

Figure B.22: Mode shape of the deck plate after damping treatment (f = 22.67 Hz)

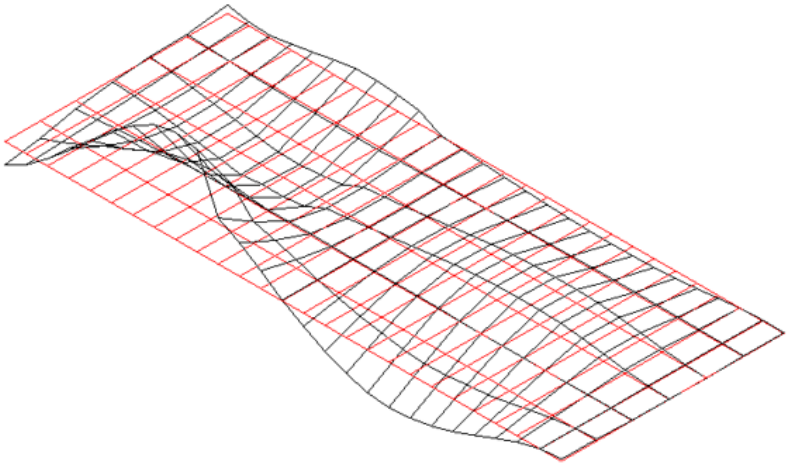

Figure B.23: Mode shape of the deck plate after damping treatment (f = 31.16 Hz)

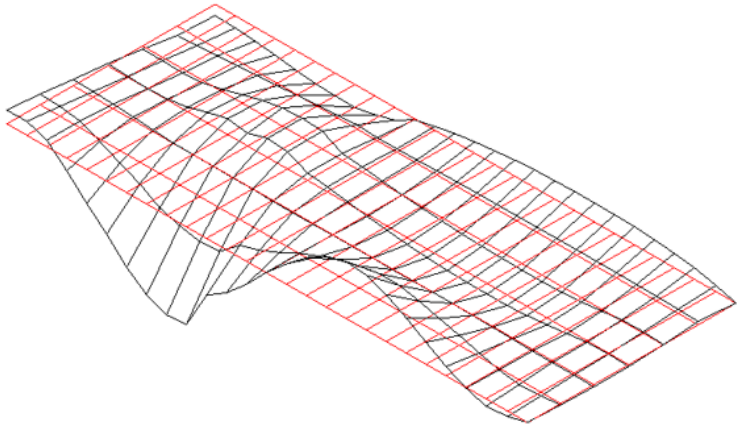

Figure B.24: Mode shape of the deck plate after damping treatment (f = 33.43 Hz)

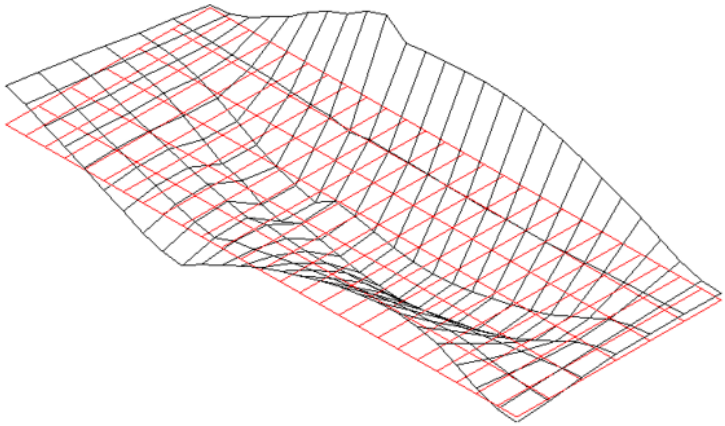

Figure B.25: Mode shape of the deck plate after damping treatment (f = 36.38 Hz)

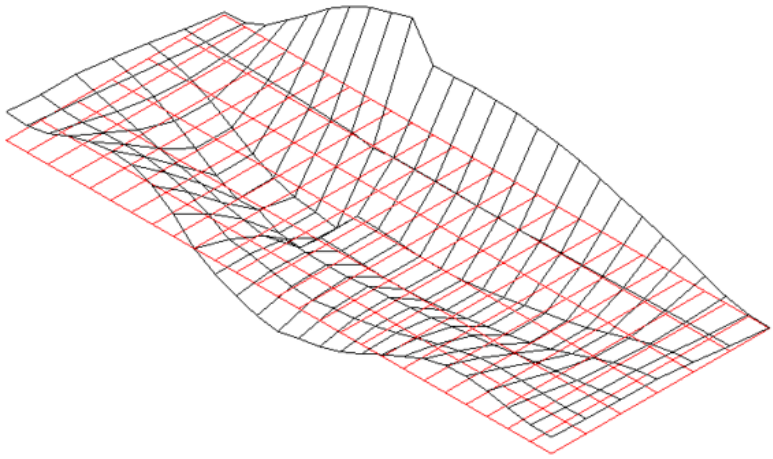

Figure B.26: Mode shape of the deck plate after damping treatment (f = 38.25 Hz)

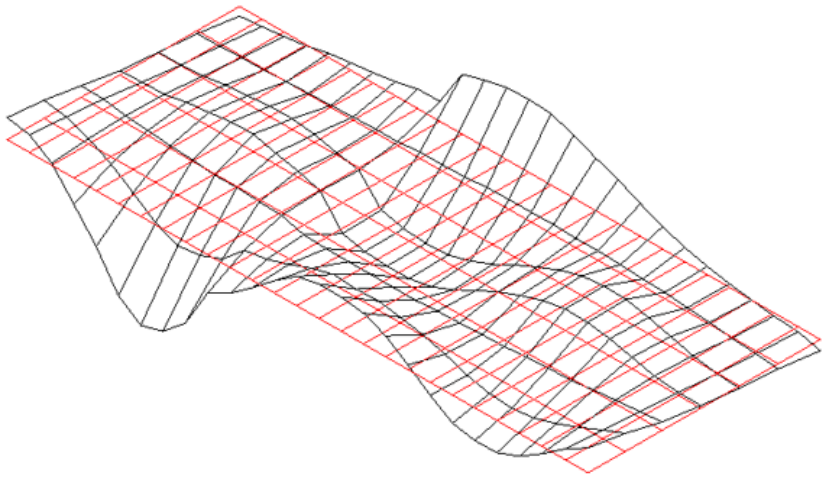

Figure B.27: Mode shape of the deck plate after damping treatment (f = 43.87 Hz)

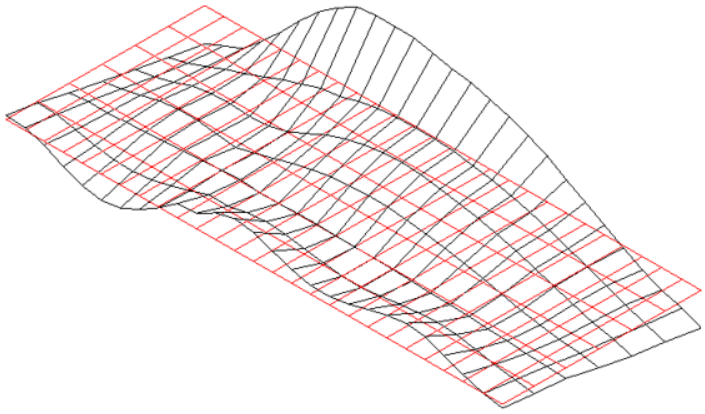

Figure B.28: Mode shape of the deck plate after damping treatment (f = 49.69 Hz)

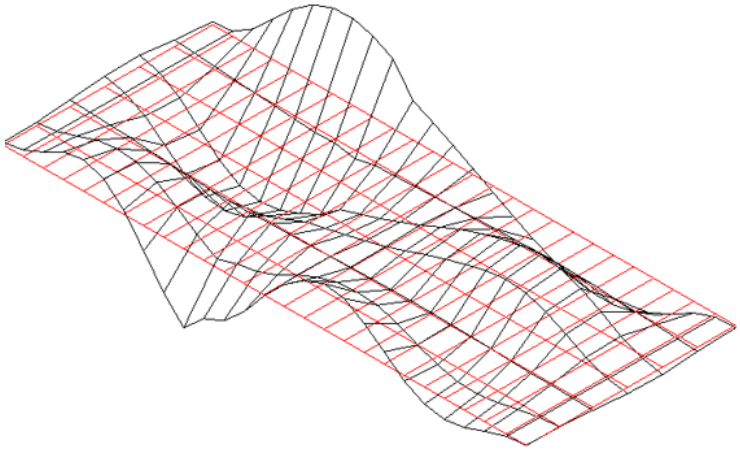

Figure B.29: Mode shape of the deck plate after damping treatment (f = 54.77 Hz)

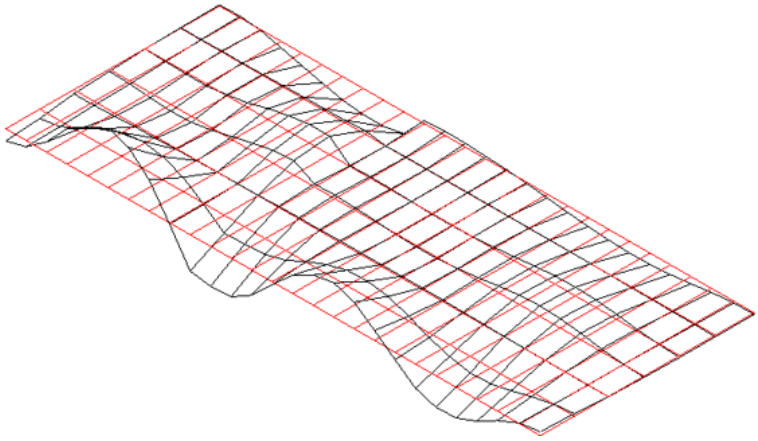

Figure B.30: Mode shape of the deck plate after damping treatment (f = 60.67 Hz)

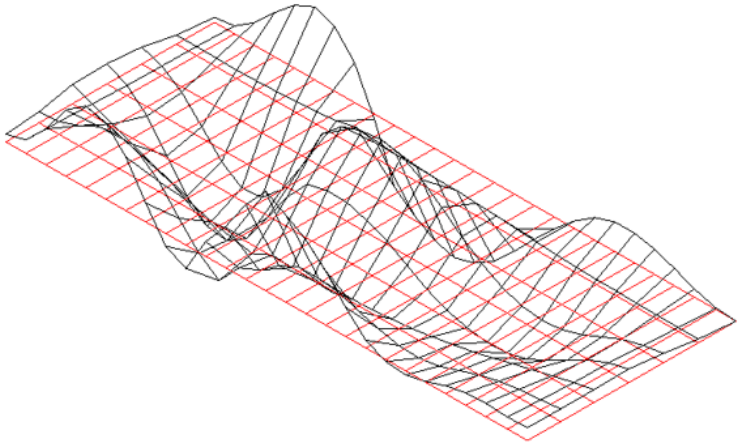

Figure B.31: Mode shape of the deck plate after damping treatment (f = 66.85 Hz)

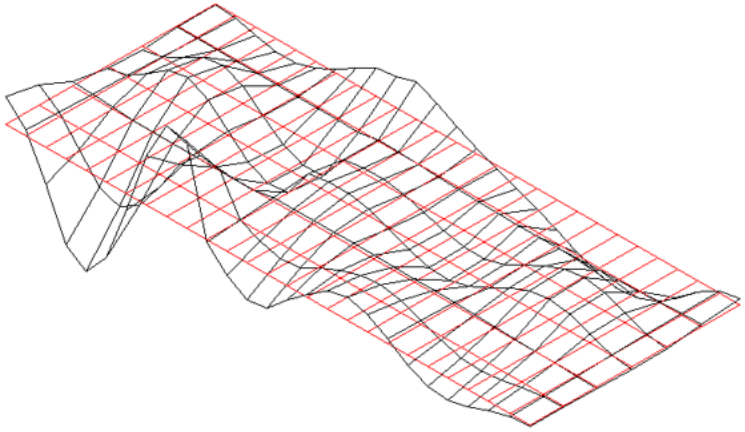

Figure B.32: Mode shape of the deck plate after damping treatment (f = 77.32 Hz)

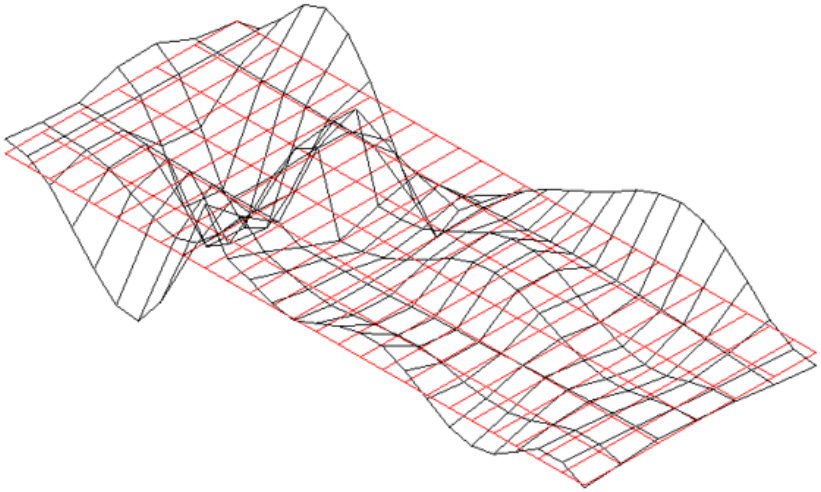

Figure B.33: Mode shape of the deck plate after damping treatment (f = 82.57 Hz)

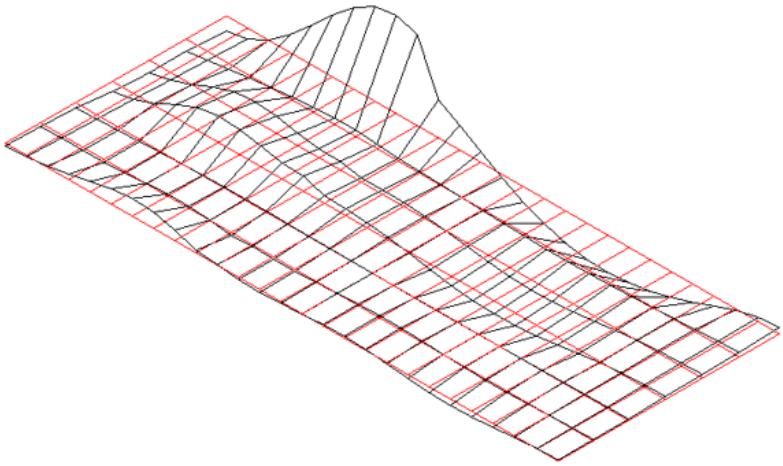

Figure B.34: Mode shape of the deck plate after damping treatment (f= 88.40 Hz)

Appendix-C: Supplementary Results of SEA

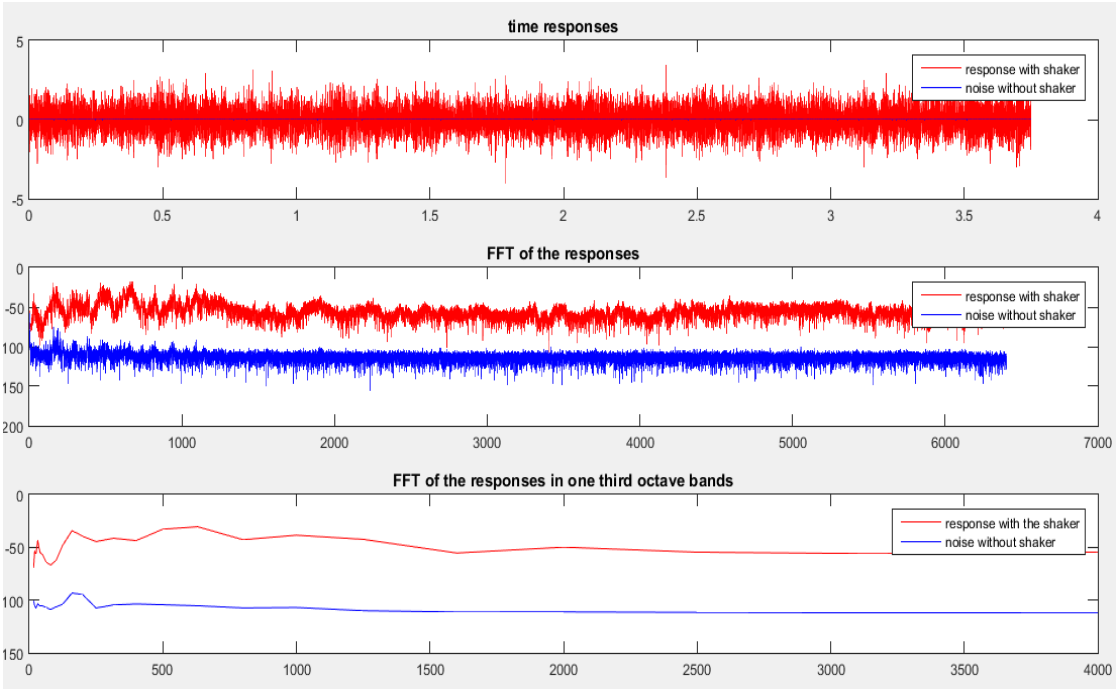

Figure C.1: Shaker excitation test.

Band No.	Lower Frequency	Central Frequency	Upper Frequency
	$[Hz]$	$[Hz]$	$[Hz]$
1	14.1	16	17.8
2	17.8	20	22.4
3	22.4	25	28.2
4	28.2	31.5	35.5
5	35.5	40	44.7
6	44.7	50	56.2
7	56.2	63	70.8
8	70.8	80	89.1
9	89.1	100	112

10	112	125	141
11	141	160	178
12	178	200	224
13	224	250	282
14	282	315	355
15	355	400	447
16	447	500	562
17	562	630	708
18	708	800	891
19	891	1000	1122
20	1122	1250	1413
21	1413	1600	1778
22	1778	2000	2239
23	2239	2500	2818
24	2818	3150	3548
25	3548	4000	4467

Figure C.2: One third octave band frequency range.